

**Experimental Studies of Surface and Gas-
Phase Processes Relevant to the
Interstellar Medium and Planetary
Atmospheres**

Elsbeth Rebecca Latimer

Thesis submitted for the degree of Doctor of Philosophy

University College London

2010



*I, Elspeth Rebecca Latimer confirm that the work presented in this thesis is my own.
Where information has been derived from other sources, I confirm that this has been
indicated in the thesis.*

Abstract

The interstellar medium (ISM) is the region of space between stars, where star and planet formation occurs. Molecular hydrogen is vitally important to the chemistry that happens in the ISM, as it initiates most of the reactions. The molecules that result from these reactions act as a coolant for the huge molecular clouds that collapse to form stars. The abundance of molecular hydrogen in the ISM is too high to form through gas phase processes alone. The accepted formation mechanism for H_2 is *via* heterogeneous catalysis on the surface of interstellar dust grains. These dust grains make up approximately 1% mass of the ISM and are carbonaceous or silicate in composition.

The experiment presented in this thesis has been designed to probe ro-vibrational energy of nascent HD formed on an interstellar dust grain analogue. The experiment involves the use of two atom sources, to produce H and D atoms, ultrahigh vacuum chambers and cryogenic cooling to obtain conditions relevant to the ISM. The laser technique of resonance enhanced multiphoton ionisation (REMPI) is employed to state selectively ionise the HD, in order to investigate the internal energy of the newly formed HD when it desorbs from the highly orientated pyrolytic graphite surface. The results are presented here and are compared to other theoretical and experimental studies; the astrophysical implications are discussed.

Also included in this thesis is a study of the electron impact ionisation of OCS using pulsed time-of-flight in conjunction with a 2-D coincidence technique. The experimental set-up allows fragment ions to be formed by dissociative single, double and triple ionisation to be detected and quantified. The relative partial ionisation cross sections (PICS) and precursor specific relative PICS are derived as well as information on OCS^{2+} . OCS is found in the atmospheres of Jupiter and Venus, where it may exist in a doubly charged state, OCS has been observed in the interstellar medium.

Acknowledgements

Completing this PhD and thesis has been a long process and something I would not have achieved without the help of the following people:

Steve Price, for his inspirational guidance over the past three years and his never ending belief in me and the experiment. Wendy Brown, for being an excellent second supervisor and providing me with good advice.

John Edridge, for the endless cups of tea and pints of cider, without which I would be heavily under caffeinated and probably have a stronger liver! For listening to me whinge about broken lasers or HD signals when there shouldn't be HD signals and for the endless argument about who had the better vacuum or the bigger laser.

All the other members of the Price group who have all, at some point, helped me with the experiment and been excellent fun to work with.

My parents, for their complete faith in me from the very beginning and always being there to provide words of wisdom and occasionally some extra funding.

My friends, Issie and Jess, who know that I work with dust and possibly think that I might be an astronaut but who continually support me with a lot of hugs, tea, wine and most vitally laughs.

Finally, Tom, there are no words; just that it would have been a long three years without him. Thank you.

Table of Contents

| | |
|---|-----------|
| Abstract | 2 |
| Acknowledgements | 3 |
| Table of Contents | 4 |
| List of Figures | 8 |
| List of Tables | 14 |
| | |
| Chapter 1. Introduction | 16 |
| 1.1 Hydrogen in the Early Universe | 16 |
| 1.2 Hydrogen in the Interstellar Medium | 17 |
| 1.3 Chemistry in the ISM | 20 |
| 1.4 Hydrogen Formation in the ISM | 23 |
| 1.5 Interstellar Dust Grains | 24 |
| 1.6 Molecule Formation Mechanisms | 28 |
| 1.7 Previous Work | 30 |
| 1.7.1 Theoretical Studies | 30 |
| 1.7.2 Experimental Studies | 35 |
| 1.8 The UCL Cosmic Dust Experiment | 43 |
| 1.9 Interstellar Ices and OCS in the ISM | 44 |
| 1.10 Molecular Dications in the ISM and Planetary Atmospheres | 45 |
| 1.11 Ionisation Cross-Sections | 46 |
| 1.12 Multiply Charged States of Small Molecules | 48 |
| 1.13 Summary | 51 |
| 1.14 References | 52 |
| | |
| Chapter 2. Experimental | 56 |
| 2.1 Vacuum Set-up | 57 |
| 2.2 H-atom and D-atom Generation | 58 |
| 2.3 Atom Beam Transport | 60 |
| 2.4 Target Mount and Coldhead | 62 |

Table of Contents

| | | |
|-------------------|---|-----------|
| 2.5 | Time of Flight Mass Spectrometry | 65 |
| 2.6 | Focussing Conditions for the TOFMS | 67 |
| 2.7 | The Laser System and REMPI Technique | 69 |
| 2.7.1 | Laser System | 69 |
| 2.7.2 | Nd:YAG Laser | 69 |
| 2.7.3 | Tuneable Dye Laser | 71 |
| 2.7.4 | Frequency Doubling and Frequency Mixing | 74 |
| 2.7.5 | Frequency Doubling | 74 |
| 2.7.6 | Frequency Mixing | 77 |
| 2.7.7 | Frequency Doubling and Mixing Optics | 78 |
| 2.8 | Resonance Enhanced Multiphoton Ionisation (REMPI) | 81 |
| 2.9 | Commissioning of the Position Sensitive Detector | 85 |
| 2.10 | Summary | 88 |
| 2.11 | References | 89 |
| Chapter 3. | Results of the Formation of HD on a Graphite Surface | 90 |
| 3.1 | Experimental Methods | 90 |
| 3.1.1 | Calibration of Laser Power | 92 |
| 3.1.2 | Determination of Rotational Temperature | 94 |
| 3.2 | HD Formation on HOPG | 95 |
| 3.2.1 | HD formed in $v'' = 3$ and 4 | 95 |
| 3.2.2 | HD formed in $v'' = 5, 6$ and 7 | 101 |
| 3.3 | Energy Partitioning | 108 |
| 3.3.1 | Translational Energy | 108 |
| 3.3.2 | Internal Energy and Energy flow into the Graphite | 111 |
| 3.4 | Discussion | 113 |
| 3.5 | Astronomical Implications | 116 |
| 3.6 | Summary | 119 |
| 3.7 | References | 121 |

Table of Contents

| | |
|--|------------|
| Chapter 4. Commissioning of Cold Atom Jets and Consequent Experimental Shortcomings | 123 |
| 4.1 Cooling of Atom Beams | 123 |
| 4.2 Results | 126 |
| 4.3 Problem Solving | 128 |
| 4.4 Conclusion | 134 |
| 4.5 References | 135 |
| | |
| Chapter 5. Studies of the Dissociation and Energetics of OCS | 136 |
| 5.1 Introduction | 136 |
| 5.2 Experimental | 137 |
| 5.2.1 Ion Discrimination Effects | 139 |
| 5.2.2 Energetic Ion Collection | 140 |
| 5.3 Data Analysis | 141 |
| 5.3.1 Singles Spectra | 141 |
| 5.3.2 Pairs Spectra | 142 |
| 5.3.3 Triples Spectra | 145 |
| 5.3.4 Relative Partial Ionisation Cross Sections | 147 |
| 5.4 Results | 149 |
| 5.4.1 Relative Partial Ionisation Cross Sections for OCS | 149 |
| 5.4.1.1 Relative PICS (σ_r) Values | 150 |
| 5.4.1.2 Precursor-Specific Relative PICS | 152 |
| 5.4.2 Discussion | 155 |
| 5.4.3 The Energetics of OCS Dissociation | 156 |
| 5.5 Summary | 160 |
| 5.6 References | 161 |
| | |
| Chapter 6. Further Work | 162 |
| 6.1 Water in the ISM | 162 |
| 6.1.1 Preliminary Experiments | 163 |
| 6.1.2 Safety | 163 |

Table of Contents

| | | |
|--|---|------------|
| 6.2 | Other Interstellar Grain Analogue Surfaces | 164 |
| 6.3 | Summary | 164 |
| 6.4 | References | 165 |
| | | |
| Appendix A. Calculation of Ion Flight Times in a Two Field Time-of-Flight Mass Spectrometer | | 166 |
| | | |
| Appendix B. Error analysis on the Rotational Populations | | 172 |
| | | |
| Appendix C. Derivation of Relative PICS and Relative Precursor Specific PICS equations | | 177 |

List of Figures

Chapter 1.

Figure 1.5.1 Barnard 68. The dust grains present in this dense interstellar cloud result in the extinction of the background starlight. Image taken from astronomyonline.org/Stars/Introduction.asp **25**

Figure 1.5.2 Stellar extinction curve, taken from reference³³. The dotted line indicates the proposed contribution of graphite to the curve. **26**

Figure 1.5.3 Reflection nebula NGC 1999, image captured by the Hubble Space Telescope. Image from www.telegraph.co.uk/science/picture-galleries **27**

Figure 1.5.4 Schematic of a typical interstellar dust grain. **28**

Figure 1.7.1 Figure taken from the work of Sidis *et al*⁴³ on the Langmir-Hinshelwood formation mechanism. Figure depicts the ro-vibrational distribution for H₂ formed on a felexible grapheme surface at 200 K. (a) nascent H₂ molecules from formation *via* LH mechanism. (b) reflected molecules after one collision with the surface. **34**

Figure 1.7.2 Figure taken from the work of Hornekaer *et al*.¹⁹ Figure shows STM images of a graphite surface after increasing doses of D atoms, (a) one bright spot on the graphite surface, (b) after dosing D atoms for 1 min, (c) after dosing D atoms for 6 mins and (d) after dosing D atoms onto the graphite for 24 mins. **40**

Figure 1.12.1 Schematic representation of the potential energy curves for a dication AB²⁺, taken from reference⁹² **48**

Figure 1.12.2 Schematic potential energy curves describing the avoided crossing of two potentials, one corresponding to monocation-monocation potential and the other to dication-neutral potential, forming a thermodynamically unstable, but long-lived

Table of Contents

metastable dication. The vibrational level for a metastable state are indicated, the lifetimes of these states are influenced by curve-crossings to dissociative potentials.⁹³ 49

Chapter 2.

Figure 2.1.1 Schematic diagram of vacuum chamber set-up (not to scale). 57

Figure 2.2.1. One half of a microwave radiator showing two sets of slots. 58

Figure 2.2.2 Schematic diagram of a H or D-atom source. 59

Figure 2.2.3 Basic circuit diagram of the safety trips for the H and D atom sources. 60

Figure 2.3.1 Schematic diagram to show how the H and D-atoms are piped through the PTFE tubes and blocks. The pumping holes allow some of the gas to escape into the source chamber so that the pressure in the target chamber stays low, but the dissociation cells can still be kept at an optimum pressure for H and D dissociation. 61

Figure 2.3.2 Schematic diagram to show how the H and D-atom transport tubes are mounted on the repeller plate of the time-of-flight mass spectrometer. 62

Figure 2.4.1 Schematic diagram of target mount set-up. 63

Figure 2.4.2 Diagram showing the metal clamp and tensioning wire system that holds the HOPG surface in place. One clamp is used on either side of the target for security. 64

Figure 2.5.1 Schematic diagram of physical arrangement of the TOFMS. 66

Figure 2.5.2 Block diagram to show the timing electronics for the TOFMS. 67

Figure 2.7.1 Energy level diagram for the transitions in the Nd:YAG laser, $\tilde{\nu}$ refers to the wavenumber of that particular level. 70

Table of Contents

| | |
|---|-----------|
| Figure 2.7.2 Schematic of the energy levels and laser transitions in a dye laser. | 72 |
| Figure 2.7.3 Schematic diagram of the optical layout of the dye laser. | 74 |
| Figure 2.7.4 Wave ellipsoid for incident and second harmonic rays. The circle and ellipse indicate how the phases of the electric fields of the O-ray and E-ray alter as they go through the crystal. ^{13,14} | 76 |
| Figure 2.7.5 Schematic diagram showing the set-up of the doubling optics. | 78 |
| Figure 2.7.6 Schematic diagram showing the set-up of the tripling optics. | 79 |
| Figure 2.7.7 Schematic of Brewster's Angle window. | 81 |
| Figure 2.8.1. Schematic diagram of the (1+1) and (2+1) REMPI processes. | 82 |
| Figure 2.8.2 (2+1) REMPI scheme taken from reference ¹⁵ | 83 |
| Figure 2.9.1. Schematic of redesign for the source and acceleration regions of the time-of-flight to reduce the effect of charging on the ceramic legs. | 88 |
| Chapter 3. | |
| Figure 3.1.1 On resonance mass spectrum for $\nu'' = 4, J'' = 1$, showing the peaks for H^+ , H_2^+ , HD^+ and D_2^+ . | 91 |
| Figure 3.1.2. Plot of $\ln(\text{ion signal})$ vs $\ln(\text{laser power})$ to determine the laser power dependence factor for HD formed in $\nu'' = 5$. The solid line is a weighted least squares fit, the gradient of which gives the values of n described in the text. | 93 |
| Figure 3.2.1 REMPI spectrum for the transition $X^1\Sigma_g^+ (\nu'' = 4, J'' = 1) \rightarrow E, F X^1\Sigma_g^+ (\nu' = 1, J' = J'')$ from HD formed on a HOPG surface held at 15 K. | 96 |

Table of Contents

Figure 3.2.2 Boltzmann plot for HD formed in $v'' = 4$ on a HOPG surface held at 15 K. The solid line is a weighed least squares fit to the data, the gradient of which yields the rotational temperature. **98**

Figure 3.2.3 Ro-vibrational distribution for HD formed on a cold graphite surface in the $v'' = 3$ and 4 vibrational states. **98**

Figure 3.2.4 Relative ro-vibrational populations for HD formed in $v'' = 1 - 4$ on a HOPG surface at 15 K. **101**

Figure 3.2.5 Derived relative ro-vibrational populations of HD formed on a HOPG surface at 15 K in the vibrational states $v'' = 1 - 7$. These ro-vibrational states are placed on a relative scale applying the methodology described in the text. **105**

Figure 3.2.6 Relative ro-vibrational populations of HD formed on a HOPG surface at 15 K in the vibrational states $v'' = 3 - 7$. The data used to compile this plot was obtained from a series of consecutive scans. **106**

Figure 3.3.1 Schematic of the paths of two ions with opposite initial velocities and their position in the TOFMS. **109**

Chapter 4.

Figure 4.1.1 A cut through of the Al block attached to the radiation shield to cool the H and D atoms. The block has two channels cut into it, similar to the one shown above, one for the H atoms and another for the D atoms. **124**

Figure 4.1.2 Schematic to show how the aluminium cooling block is attached to the radiation shield. **125**

Table of Contents

Figure 4.2.1 Derived relative ro-vibrational populations of HD formed on a HOPG surface at 15 K in the vibrational states $v'' = 1 - 7$. The H and D atoms were cooled to 45 K before reaching the surface. The ro-vibrational states are placed on a relative scale, as describe in Chapter 3. **126**

Figure 4.2.2 REMPI signal for the HD transition $E, F \ ^1\Sigma_g^+ (v' = 0, J' = 1) - X \ ^1\Sigma_g^+ (v'' = 1, J'' = 1)$. HD was formed on a HOPG surface at 298 K. The \blacklozenge symbol indicates when both atom sources were on, the \blacksquare the H source was on but the D source was off and the \blacktriangle the D source was on and the H source was off. **127**

Figure 4.2.3 REMPI signal for the HD transition $E, F \ ^1\Sigma_g^+ (v' = 0, J' = 1) - X \ ^1\Sigma_g^+ (v'' = 3, J'' = 1)$. HD was formed on a HOPG surface at 298 K. The \blacklozenge symbol indicates when both atom sources were on, the \blacksquare the H source was on but the D source was off and the \blacktriangle the D source was on and the H source was off. **128**

Figure 4.3.1 Diagram to show the set-up of the PTFE tubes in and out of the aluminium block placed in the D gas line. **130**

Figure 4.3.2 Mass spectrum showing the high background levels observed. **131**

Figure 4.3.3 Background mass spectra taken with the D_2 gas line cooled in liquid nitrogen, one spectrum taken with the microwave source on and the other with the source off but the gas still flowing. **132**

Figure 4.3.4 Background mass spectra taken with the D_2 gas line cooled and the gas allowed to pass through a zeolite before entering the dissociation cell. One spectrum was taken if the microwave source on and the other taken with the microwaves off but the D_2 still flowing. **133**

Chapter 5.

Figure 5.2.1 Schematic diagram of the experimental set-up. **138**

Table of Contents

| | |
|---|----------------|
| Figure 5.3.1 Singles time-flight-mass spectrum for the fragmentation of OCS by electron impact ionisation. | 141 |
| Figure 5.3.2 Pairs spectrum for the electron impact ionisation of OCS. | 143 |
| Figure 5.3.3 Time difference distribution for $O^+ + C^+$ recorded in the pairs spectrum for OCS. The shaded area indicates the counts missed due to energetic ion pairs, these losses are corrected for using a suitable geometric construction. | 145 |
| Figure 5.4.1 Relative PICS $\sigma_r[X^+]$ for forming ionic fragments following electron ionisation of OCS. | 152 |
| Figure 5.4.2 Relative precursor-specific PICS $\sigma_n[X^+]$ for forming ionic fragments <i>via</i> dissociative single (\blacklozenge), double (\blacksquare) or triple (\blacktriangle) ionisation of OCS. | 153-154 |
| Figure 5.4.3 Contributions to the total ion yield from single, double and triple ionisation, following the electron impact ionisation of OCS. | 154 |
| Figure 5.4.4 Schematic potential energy curve for a molecule AB, showing the relationship between the asymptotic energy of the dissociation limit, the KER and the energy of the dication precursor state that gives rise to the ion pair formation. | 157 |
| Figure 5.4.5 Schematic diagram to show the steps that can be seen in the time difference spectrum if there are two KERs for a given dissociation. | 158 |
| Appendix A | |
| Figure A.1 Schematic diagram of TOFMS showing the dimensions and electric fields needed to calculate an ion's flight time. | 166 |
| Appendix B | |
| Figure B.2 REMPI plot showing the A and B parameters described in the text. | 172 |

List of Tables

Chapter 1.

Table 1. The molecules observed in the ISM to date (adapted from www.ajmarkwick.com/achemnet/stats.php?mode=1&flat=0). **19**

Chapter 2.

Table 1. Shows the details of the dye and YAG laser set-up for the vibrational states of HD probed. **73**

Table 2. Photon wavelengths for the transition $X^1\Sigma_g^+(v'' = 1, J'') \rightarrow E, F^1\Sigma_g^+(v' = 1, J')$ **85**

Chapter 3.

Table 1. Table to show the laser power dependence factors determined for each vibrational state of HD. **93**

Table 2. Table detailing the different Franck Condon factors³ and $|M_{fo}|^2$ for HD in $v'' = 1 - 6$, $v'' = 7$ is not included in this table as Huo and Zare¹⁰ did not calculate values of $|M_{fo}|^2$ for vibrational states higher than $v'' = 6$. **99**

Table 3. Details the spectroscopic constants obtained from Dabrowski and Herzberg,¹² used in the calculation of the wavelengths required for REMPI transitions in $v'' = 5, 6$ and 7 , these values should be compared to the constants obtained from NIST which were $B_e = 24.568 \text{ cm}^{-1}$ and $D_e = 0.0123 \text{ cm}^{-1}$. **102**

Table 4. Shows a complete list of all the ro-vibrational states detected and the relevant average rotational temperatures. **104**

Table of Contents

Table 5. Experimentally estimated relative ro-vibrational populations for HD formed on a cold (15 K) HOPG surface for the vibrational states $\nu'' = 1 - 7$. The populations are derived using the relevant Franck Condon factors and are also displayed in Figure 3.2.5.

107

Table 6. Relative ro-vibrational populations for HD formed on a cold (15 K) HOPG surface for the vibrational states $\nu'' = 3 - 7$. This distribution was derived from a series of consecutive scans and is also shown in Figure 3.2.6.

107

Table 7. Experimentally estimated nascent vibrational distribution for HD formed on a cold HOPG surface.

108

Table 8. Table detailing how the 4.5 eV of binding energy released on the formation of HD is distributed through the various possible internal energy modes and into the HOPG surface. As discussed in the text above the value for the translational energy is an upper limit and hence the value for the energy deposited into the surface is a lower limit.

112

Chapter 5.

Table 1. Optimum experimental parameters.

139

Table 2. Details of the σ_r , σ_1 , σ_2 and σ_3 values calculated by Wang and Vidal using covariance mapping, these values are compared to the numbers calculated in this thesis.

151

Table 3. Details of the kinetic energy releases and peaks widths for the fragment ion pairs formed from the electron ionisation of OCS, calculated by use of a Monte Carlo simulation.

158

Table 4. Details of the excited energy states calculated from the KERs. This data is compared to the values obtained using photon ionisation by the Eland group²⁰ (a) and Cooks *et al*²¹ data from electron impact ionisation (b).

159

Chapter 1

Introduction

Overview

The region of space in between stars and planets is called the Interstellar Medium (ISM) and although much of the matter in the Universe consists in the form of stars and planets the ISM is far from empty and important chemistry occurs in this region. The ISM contains vast clouds of gas and dust called interstellar clouds, which have a mean density of 10^{10} atoms per m^3 .¹ The clouds vary in size and density but are predominantly made up of hydrogen which accounts for approximately 90% of the gas by mass. The clouds fall into three loose classifications, 'dense' ('dark' or 'molecular'), 'diffuse' and 'HII'. In the HII regions hydrogen exists in a mainly ionised form. Dust grains make up about 1% of the mass of the clouds and, as will become apparent, play an important role in the chemistry. The clouds themselves are sites for star formation, the details of which will be discussed in more detail later in this chapter.

Molecular hydrogen has been described as the 'key to interstellar chemistry';² it is the dominant molecule in the ISM and is approximately 10^5 times more abundant than CO, the next most abundant molecule. Hydrogen is also the most abundant element in the Universe; in all its various forms it accounts for 75% by mass of the Universe or 92% by number density.¹ As the lightest of the elements hydrogen was among the first to be formed at the start of the Universe, along with helium and small amounts of lithium. Hydrogen was also essential to the formation of the first stars and larger structures in the early Universe.¹ This chapter will describe the vital role that hydrogen plays in the ISM, including theories on the formation of molecular hydrogen and will explain the relevant background to the Cosmic Dust experiment, upon which the majority of this thesis is based.

1.1 Hydrogen in the Early Universe

After the 'Big Bang' the early Universe began rapidly expanding and cooling. This cooling was sufficient to allow electrons to combine with positive ions to form the neutral

Chapter 1. Introduction

atoms hydrogen and helium.² However, the expansion meant that not all the electrons were able to recombine and hence the Universe was left partially ionised, an important factor for chemistry in space. To form stars, large clouds of gas had to collapse under gravity. With gas temperatures at above 10,000 K cooling mechanisms for the hot plasma were essential as the pressure of the hot gases resisted collapse. Hydrogen atoms were able to radiate away some of this heat through their ionisation.² The clouds could also be cooled through the formation of molecular hydrogen. Molecular hydrogen initially formed *via* electron and proton catalysed reactions, for example:



Or



Collisions with atomic hydrogen resulted in the vibrational levels in the molecules being populated. These vibrationally excited molecules could emit radiation, *via* quadrupole transitions, allowing the gas to cool. Given the high temperatures present in the early Universe the vibrational levels of H₂ were easily populated hence the molecules acted as a very efficient coolant. In gas clouds with temperatures above 100 K H₂ also acted as a coolant through excitation of rotational levels within the molecule, followed by emission. Thus, molecular hydrogen is essential as a coolant. However, this is not hydrogen's only important role in the ISM, it is also largely responsible for the chemistry that occurs.

1.2 Hydrogen in the Interstellar Medium

As discussed above, the clouds in the ISM are loosely divided into three different classes. As the name suggests, diffuse clouds have much lower densities than either dark clouds or HII regions, a typical density being between 10⁷ and 10⁹ molecules m⁻³, with a gas temperature of ~100 K. Diffuse clouds can be easily penetrated by radiation such as

Chapter 1. Introduction

cosmic rays and UV photons and as a result most of the hydrogen is atomic, as H_2 is readily dissociated.^{1,2} Astronomical observations show that despite the ongoing bombardment from radiation there is still some hydrogen that remains in its molecular form; this suggests that there must be a very efficient H_2 formation mechanism. Along with hydrogen, other simple molecular species such as HCN, CN, CH^+ are found in diffuse clouds. Diffuse clouds species that have an ionisation potential less than that of atomic hydrogen, such as carbon and sulphur, can be photoionised, whereas those with an ionisation potential greater than H, such as atomic nitrogen and oxygen, exist in a neutral state.

Dark (dense or molecular) clouds are where most of the molecules in the ISM are formed. High densities of dust grains means that the molecules are shielded from UV and cosmic ray radiation. To date, over 120 molecules have been observed spectroscopically in dense clouds (Table 1.1). Typical densities in these clouds are from 10^9 to 10^{10} molecules m^{-3} . They are much cooler than the diffuse counterparts, with a gas temperature of around 10 K. Most of the hydrogen in dark clouds is in its molecular form.¹

Many molecules observed in the ISM have a rich spectrum in the radio and microwave regions; however, H_2 does not, as it does not have a dipole moment. This means that when molecules such as OH and CO were first detected in the 1960s, using radio astronomy, H_2 was not detected despite its abundance. The majority of molecular hydrogen's lowest energy transitions lie in the infrared (IR) and at these wavelengths the Earth's atmosphere is opaque.² Similarly, many of hydrogen's highest lying transitions are at UV wavelengths, where again atmospheric absorption is a problem. The universal abundance of hydrogen lead astronomers to predict that far more H_2 , greater than any other molecule, would exist in astronomical sources and, even before it was observed, a detailed theory for the formation and destruction of H_2 was developed.³

| 2 Atoms | 3 Atoms | 4 Atoms | 5 Atoms | 6 Atoms | 7 Atoms | > 7 Atoms |
|-----------------|--|--------------------------------|---------------------------------|---------------------------------|-----------------------------------|---------------------------------------|
| AlF | C ₃ | c-C ₃ H | C ₅ | C ₅ H | C ₆ H | CH ₃ C ₃ N |
| AlCl | C ₂ H | l-C ₃ H | C ₄ H | C ₅ O | CH ₂ CHCN | HCOOCH ₃ |
| C ₂ | C ₂ S | C ₃ N | C ₄ Si | C ₂ H ₄ | CH ₃ C ₂ H | CH ₃ COOH |
| CH | HCN | C ₃ O | l-C ₃ H ₂ | CH ₃ CN | HC ₅ N | CH ₃ C ₄ H |
| CN | HCO | C ₃ S | c-C ₃ H ₂ | CH ₃ OH | HCOCH ₃ | CH ₃ CH ₂ CN |
| CO | HCS ⁺ | C ₂ H ₂ | CH ₂ CN | CH ₃ SH | NH ₂ CH ₃ | (CH ₃) ₂ O |
| CO ⁺ | HOC ⁺ | CH ₂ D ⁺ | CH ₄ | HC ₃ NH ⁺ | c-C ₂ H ₄ O | CH ₃ CH ₂ OH |
| CP | H ₂ O | HCCN | HC ₃ N | HC ₂ CHO | CH ₂ CHOH | HC ₇ N |
| CS | H ₂ S | HCNH ⁺ | HC ₂ NC | HCONH ₂ | | C ₈ H |
| CSi | HNC | HNCO | HCOOH | l-H ₂ C ₄ | | CH ₃ C ₅ N |
| HCl | HNO | HNCS | H ₂ CHN | C ₅ N | | (CH ₃) ₂ CO |
| H ₂ | MgCN | HOCO ⁺ | H ₂ C ₂ O | | | NH ₂ CH ₂ COOH |
| KCl | MgNC | H ₂ CO | H ₂ NCN | | | HC ₉ N |
| NH | N ₂ H ⁺ N ₂ O | H ₂ CN | HNC ₃ | | | HC ₁₁ N |
| NO | NaCN | H ₂ CS | SiH ₄ | | | CH ₈ CH ₂ OHCHO |
| NS | OCS | H ₃ O ⁺ | H ₂ COH ⁺ | | | C ₇ H |
| NaCl | SO ₂ | NH ₃ | | | | H ₂ C ₆ |
| OH | c-SiC ₂ | SiC ₃ | | | | |
| PN | CO ₂ | | | | | |
| SO | NH ₂ | | | | | |
| SO ⁺ | H ₃ ⁺ | | | | | |
| SiN | AlCN | | | | | |
| SiO | | | | | | |
| SiS | | | | | | |
| HF | | | | | | |
| SH | | | | | | |

Table 1. The molecules observed in the ISM to date (adapted from www.ajmarkwick.com/achemnet/stats.php?mode=1&flat=0).

Chapter 1. Introduction

The first observations of molecular hydrogen outside the solar system were made in 1970 by Carruthers *et al*, using an ultraviolet spectrometer launched on a rocket and focused on the star ξ Persei.⁴ The results of this experiment showed the Lyman bands of interstellar H₂ between 100 – 110 nm. In the same piece of work the Ly- α absorption of atomic hydrogen was also detected. Later, a more detailed study of molecular hydrogen in the ISM was carried out using the Copernicus satellite.⁵ A UV spectrometer was directed towards nearby stars and measurements of the rotational excitation of the H₂ were carried out. These findings resulted in the determination of the gas temperature which was found to be 81 ± 31 K.

1976 saw the detection of the first infrared emissions from interstellar molecular hydrogen using ground-based instruments.^{6,7} These measurements had to be carried out at wavelengths that could penetrate the Earth's atmosphere (between 2.2 and 2.4 microns). The quadrupole emission of hydrogen was observed and the rotational temperature of the gas was determined and found to be 2000 K, considerably higher than expected. This high temperature was attributed to high internal excitation of H₂ that had formed on dust grain surfaces.

Details about the abundance of molecular hydrogen in the ISM can be derived through the observations of other molecules, particularly CO which is the second most abundant molecule. When both H₂ and CO can be observed in a cloud, the ratio of the molecules is typically $n(\text{H}_2) = 10^5 n(\text{CO})$.^{1,6} Therefore, in regions where H₂ cannot be directly observed, for example in dark clouds, the abundance of H₂ can be inferred through the determination of the CO abundance, since the H₂:CO ratio is believed to be constant throughout the interstellar medium.¹

1.3 Chemistry in the ISM

In the ISM the most common reaction pathways are ion-neutral or neutral-neutral reactions as these reactions proceed rapidly, with a rate constant of approximately $10^{-15} \text{ m}^3 \text{ s}^{-1}$.¹ Hydrogen dominates interstellar gas phase chemistry because, in comparison to more reactive elements such as oxygen, nitrogen, carbon, silicon and sulphur, hydrogen is

Chapter 1. Introduction

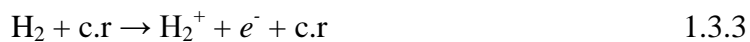
vastly more abundant. Given hydrogen's abundance the more reactive species present in the clouds are more likely to collide with atoms or molecules of hydrogen than with any other species.¹ The chemistry in the ISM particularly depends on the amount of molecular hydrogen present, as the collision of an atom of any species with H₂ will result in a more efficient reaction than a collision of another atom with atomic hydrogen. This is the case because atom-atom interactions occur on a timescale (10⁻¹³ s) too fast to enable the excess energy formation energy to be radiated away, hence any proto-molecule will fall apart before it can become energetically stabilised.¹



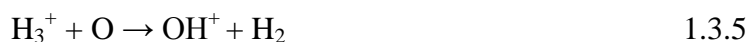
In the case of reactions with H₂ and atoms of other elements, or reactions between other molecules and H₂, the reaction pathway is more efficient due to rearrangements to remove the excess energy that can occur before the species fall apart, for example:



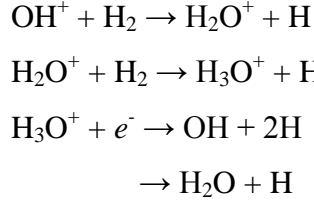
Larger molecules are often formed through interactions with molecular hydrogen, *via* the formation of the H₃⁺ ion. The ionisation of H₂ is as a result of interactions with cosmic rays, usually high energy protons. The H₂⁺ ions form H₃⁺ by a further reaction with H₂ molecules:



The consequent reactions of H₃⁺ lead to the formation of a variety of other molecules such as water *via* reactions with oxygen atoms in schemes such as:



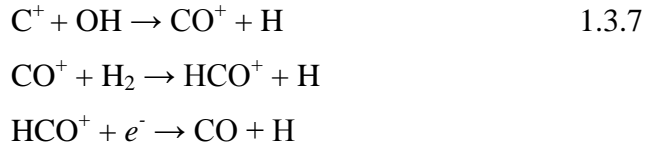
Chapter 1. Introduction



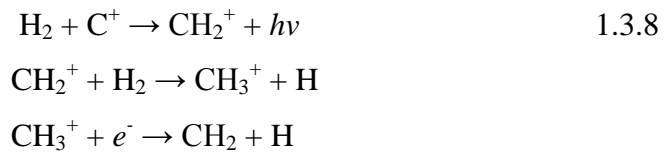
Water and OH are found in relatively high abundances in the ISM and their presence can lead to the formation of other molecules such as CO, the second most abundant molecule in the ISM.



Or



Radiative association reactions between C^+ and molecular hydrogen give rise to simple hydrocarbons, for example:



The formation of these molecules in the ISM, particularly those with dipole moments such as CO, is vital as they can act as coolants of interstellar clouds which can lead to the collapse of the clouds to form stars.^{1,2} Molecular clouds collapse under their own gravity and form stars when their density is great enough for nuclear fusion to occur, when the mass of the cloud is higher than a critical mass M_{crit} . As the cloud begins to collapse the gravitational potential energy is released and converted into kinetic energy in the molecules in the cloud. The increase in kinetic energy results in a rise in temperature and

pressure which means that the cloud becomes resistant to collapse. Clouds are able to collapse due to the presence of molecules such as CO, H₂O and OH as they can radiate away the excess energy.^{1,2} For clouds at lower temperatures (10 – 100 K) CO is the most important coolant and, as mentioned previously, for clouds at higher temperatures H₂ acts as a coolant. Molecular hydrogen does not have a dipole moment so it does not radiate by electric dipole transitions, instead it radiates by electric quadrupole transitions and only $\Delta J = \pm 2$ transitions are allowed.

1.4 Hydrogen Formation in the ISM

A significant problem for astronomers has been accounting for the high abundance of hydrogen in the interstellar medium. As discussed above, molecular hydrogen is approximately 10^5 times more abundant than CO, the next most abundant molecule. Hence, H₂ must have a highly efficient formation mechanism to counteract the destruction of H₂ by cosmic rays and account for its large number density. Calculations show that an H₂ molecule in a diffuse cloud will have a lifetime of approximately 1000 years, which on an astrophysical timescale, is very short.²

As discussed previously, in the early Universe molecular hydrogen was formed through electron and proton catalysed reactions. However, in the modern day Universe electrons and protons are a minor constituent of interstellar clouds, so reactions catalysed by electrons and protons are very slow.^{2,7} Reactions due to electrons and protons are only able to explain an H₂ abundance of ~ 1 part per billion with respect to the number of H atoms, which is approximately 1000 times less than the smallest observed H₂ abundances.² Under atmospheric conditions the simple H + H gas phase reaction would be the most common formation mechanism. However, as mentioned previously, conditions in the ISM mean that the contact time between the two H atoms is insufficient to radiate away the ~ 4.5 eV binding energy that is released on H₂ formation. Hence, this reaction occurs infrequently.



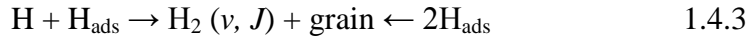
Chapter 1. Introduction

Three body reactions such as:



could be more efficient as the third body, M, could remove the excess energy from H_2^* . However, the chance of the three bodies colliding is slim given that the pressure in the ISM is very low and this reaction pathway becomes insignificant at H atom densities below $\sim 10^{14} \text{ m}^{-3}$.^{1,2}

The most widely accepted formation mechanism for H_2 in the ISM is that it forms *via* heterogeneous catalysis on the surface of interstellar dust grains in the following reaction:^{4,7-29}



H_{ads} indicates an H atom adsorbed on a dust grain surface. This catalytic process is believed to be highly efficient and it is thought that every H atom arriving at a grain surface will leave as part of a hydrogen molecule.^{14,16} It is this formation mechanism that forms the basis of the experiments described in this thesis.

1.5 Interstellar Dust Grains

Dust grains were first observed, albeit accidentally, in 1784 by William Herschel.³⁰ It was noted by Herschel that there were entire regions of the sky where there appeared to be no stars, which he referred to as ‘holes in the sky’. These areas were most apparent against the rich star fields of the Milky Way.^{30,31} Initially, it was not obvious whether there was something blocking the light from the background stars or in fact a complete absence of stars. It is now well documented that the medium blocking the starlight are dust grains which not only absorb radiation from stars but also scatter it.³⁰

Dust grains are now known to play a vital role in the chemistry of the ISM and make up approximately 1% by mass of interstellar space. As discussed already, dust grains are

Chapter 1. Introduction

believed to be active sites for molecule formation; but that is not their only role, they are important in establishing thermal equilibrium in interstellar clouds and in controlling the collapse of clouds to form stars.

Grains in diffuse clouds have a surface temperature of approximately 15 K^{15} as a result of a kinetic balance between the emission and absorption of radiation. In dense clouds, which are much more shielded from background radiation, the temperature of the dust is much lower, at around $5 - 10 \text{ K}$. The gas and dust in interstellar clouds does not have to be at the same temperature and often the gas will be warmer than the dust.



Figure 1.5.1 Barnard 68. The dust grains present in this dense interstellar cloud result in the extinction of the background starlight. Image taken from astronomyonline.org/Stars/Introduction.asp

Since the early observations of interstellar clouds, the evidence supporting the presence of dust grains has been mounting. The obstruction of starlight is termed extinction and a significant piece of evidence for dust grains is the stellar extinction curve, Figure 1.5.2. This plot illustrates the normalised rate of the extinction of starlight as a function of wavelength. Evidence suggests that the extinction of light is most effective when there is an approximate match between the size of the dust grain and the wavelength of the light they obscure.³² The stellar extinction curve shows a steady rise from infrared

wavelengths up to visible, where a large bump is observed: after this the curve continues to rise into the ultraviolet wavelengths.

The extinction curve can be modelled by a distribution of dust grain sizes ranging from a few nanometres up to a micron.³⁰ The curve can also provide details about the composition of the dust grains. Models of the extinction curve have included various materials including silicates and carbonaceous materials. Suggestions have been made that the bump in the curve at 4.1 μm is due to graphite and the plot below shows the expected graphite contribution.

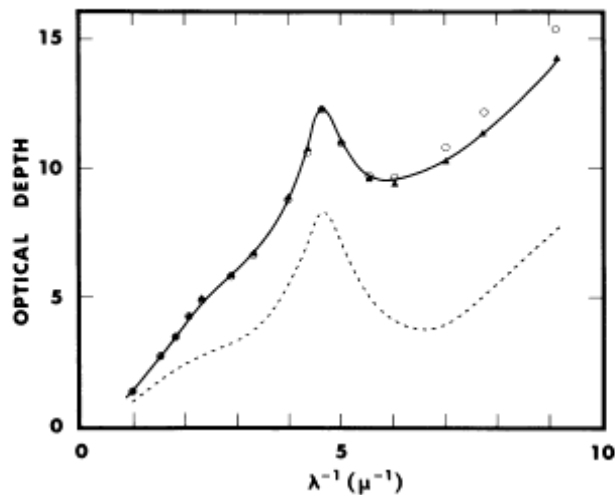


Figure 1.5.2 Stellar extinction curve, taken from reference³³. The dotted line indicates the proposed contribution of graphite to the curve.

Starlight is generally linearly polarised after passing through dust clouds, the amount of polarisation appears to be proportional to the amount of starlight extinction. For polarisation of the light to occur the dust grains must not be spherical and must also have a certain degree of alignment, which is caused by the interstellar magnetic field.^{1,30} The polarisation is only a few percent as the grains are rotating and their positions can be affected by collisions. Further information about the composition of the grains can be inferred from interstellar elemental depletion.³² It is assumed that the relative abundances of the various elements observed in the sun are similar across the galaxy, given that the sun is thought to have formed from a typical interstellar cloud. Observations show that

Chapter 1. Introduction

many elements are less abundant in dust clouds compared with the sun. This difference can be explained if some of the gas present in the clouds is cooling and forming stable solids, i.e. silicates, graphite and metal oxides, which then form dust grains. Studies have been carried out on a dust cloud near the star Zeta Ophiuchi, showing that elements such as Fe, Ca and Ti are greatly depleted and the amounts of carbon are only slightly reduced. However, the total abundance of carbon is considerably greater than most of the metals and hence the percentage of carbon in dust grains is thought to be high. The grains are thought to scatter diffuse starlight; this scattering cannot be attributed to atoms or molecules but to species the size of dust grains. When the dust clouds are close to bright stars this scattering can occasionally be detected; cases such as these are called reflection nebulae (Figure 1.5.3).



Figure 1.5.3 Reflection nebula NGC 1999, image captured by the Hubble Space Telescope. Image from www.telegraph.co.uk/science/picture-galleries

Infrared (IR) spectroscopy is one of the most effective tools for investigating the composition of dust grains. Carrying out ground-based observations is extremely complicated due to the nature of the Earth's atmosphere. However, accurate observations

can be carried out using the European satellite, the Infrared Space Observatory (ISO).^{15,30} By using ISO to monitor absorption of IR light, amorphous and crystalline silicates have been observed along with IR absorption by molecular ices, including H₂O, CO₂, CO and CH₃OH; polycyclic aromatic hydrocarbons (PAHs) have also been observed.^{15,30,32} In diffuse interstellar clouds there is little or no evidence of ices on the grains in this very low density environment.^{15,30} The collection of this data makes it possible to build a model of a typical interstellar grain. Generally the grains range in size from between 0.1 – 10 μm, with cores made up of metals, silicates and carbonaceous materials. In dense clouds the grains are likely to be covered in icy mantles.

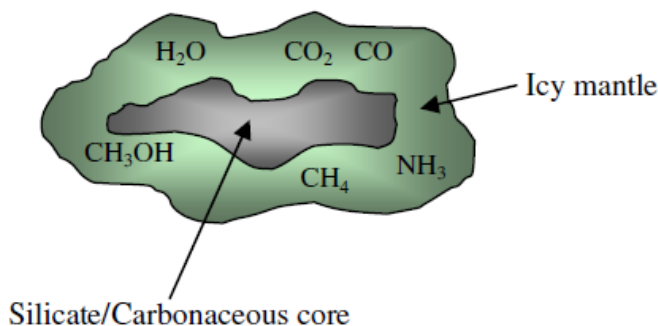


Figure 1.5.4 Schematic of a typical interstellar dust grain.

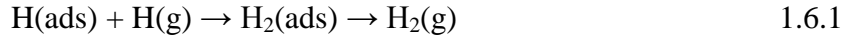
1.6 Molecule Formation Mechanisms

The study of the formation of molecules on dust grain surfaces first requires consideration of the surface processes that can occur. It is possible to consider the chemistry that occurs on such surfaces in a series of steps. Firstly, the adsorption on the surface followed by diffusion across the surface, which may lead to the possible reaction with another adsorbate. As the number of adsorbates increases an icy mantle will grow and then finally desorption will occur. Given the low temperatures in the ISM, it is probable that almost all species that collide with a grain surface will stick to it; this assumption is used in many theoretical models of dust grain surfaces where a sticking probability of unity is used.^{12,23} The mobility of the species on the surface must be considered and the nature of the mobility. Atoms and molecules can move *via* surface

Chapter 1. Introduction

diffusion or quantum tunnelling for light adsorbates, such as hydrogen atoms. The strength of the interaction of the adsorbate with the surface, and hence the mobility, leads to different reaction mechanisms.

The two major mechanisms considered for molecular hydrogen formation on dust grain surfaces are the Eley-Rideal (ER) mechanism and the Langmuir-Hinshelwood (LH) mechanism. There is also a third proposed mechanism, the ‘hot-atom’ mechanism.²⁵ In the ER process an adsorbed H atom reacts with an atom from the gas phase, after which the newly formed molecule may desorb from the surface.



In contrast, the LH mechanism involves two adsorbed and thermalised H atoms on the surface which diffuse across the surface either by tunnelling or thermal hopping, when they meet they will react on the surface and are desorbed as a molecule.



The ‘hot atom’ mechanism is an intermediate mechanism between ER and LH processes, where one of the atoms is bound to the surface and the second atom, from the gas phase, is temporarily trapped on the surface, but will react with the adsorbed H atom before thermalisation with the surface can occur.²⁵ There have been many theoretical^{10,12,14,16,23-26,34-37} investigations into these mechanisms of H₂ formation and it is still unclear which one is the main route for the production of H₂ in the ISM. The majority of theoretical studies have addressed the Eley-Rideal mechanism. However, it is the LH mechanism that is thought to be the most relevant in diffuse clouds where a relatively low coverage of H atoms on the dust grains is expected.³⁸

The different formation mechanisms should impact on the internal energy of the nascent H₂ molecules. The dominance of one mechanism over the other may depend on the sticking probability of hydrogen atoms on the surface, and other factors that could

Chapter 1. Introduction

influence the formation pathway are the grain and gas temperatures. The background gas composition could also affect the formation mechanism. If the initial coverage on the dust grain is high then this may result in the ER mechanism being the dominant process for H₂ formation, since the likelihood of a gas phase atom hitting an adsorbed atom is enhanced. At low coverages the LH mechanism will be favoured as there are fewer atoms on the surface, hence it is less likely that a gas phase atom will impact on an adsorbed atom, react and desorb as a molecule. The majority of H atoms on the surface are likely to be physisorbed as theoretical studies have shown a barrier to chemisorption, a barrier that has now been confirmed experimentally. Physisorbed atoms will diffuse more readily across the surface, hence the LH mechanism may dominate.

1.7 Previous Work

There has been a significant amount of interest in the formation of H₂ on interstellar dust grains and this has resulted in a large number of theoretical and computational studies of this process. More recently a number of experimental studies have been carried out, probing the formation of molecular hydrogen. Both the theoretical and the experimental studies are reviewed here.

1.7.1 Theoretical Studies

One of the earliest studies by Gould and Salpeter¹⁴ found that between temperatures of 10 – 20 K, on a ‘dirty ice’ surface, the formation of H₂ was efficient. This result was extended by Hollenbach and Salpeter,¹⁶ who concluded that hydrogen recombination on dust grains with a temperature below 25 K, would be approximately 100% efficient. The more recent theoretical studies of H₂ formation have concentrated on the formation mechanism and the type of surface. Work on an ideal graphite surface by Parniex and Bréchnignac³⁹ showed that nascent H₂ molecules will desorb from the surface with significant amount of kinetic energy and in highly excited vibrational states.

Farebrother and co-workers focused on the associative desorption of hydrogen atoms on a graphite surface *via* an Eley-Rideal mechanism.¹² Time-independent quantum reactive scattering calculations were carried out on a potential energy surface (PES) that had been

calculated using density functional theory (DFT). The results obtained indicated that the probability of forming H_2 on the graphite surface was high. The results of these calculations are consistent with empirical arguments based on studies of interstellar dust clouds. It was also found that when H_2 is formed *via* the ER mechanism, it possesses significant vibrational excitation. Farebrother *et al* determined that when H_2 is formed on a graphite surface there is a peak in the H_2 vibrational distribution at $v'' = 2$. A later study²³ by the same group used a newly developed PES based on plane-wave density functional calculations. These 3D calculations showed that the nascent H_2 had less vibrational excitation and the $v'' = 0$ state was the most likely to be populated. The majority of molecules have $v'' \leq 2$ for both the 2D and 3D calculations and 40 – 50% of the total amount of H_2 internal energy was translational energy. Although the amount of vibrational energy was observed to be low the hydrogen molecules were found to be highly rotationally excited, with J states of up to $J'' = 20$ populated.

Meijer *et al* performed calculations focusing on the ER mechanism of H_2 formation on a graphite surface.³⁵ This mechanism was studied using a time-dependent wave packet method. They investigated the presence of other non-reactive H atoms on the surface and their effect on the reaction dynamics. This investigation was carried out by assuming a monolayer of hydrogen physisorbed onto the graphite surface. Meijer and co-workers observed that, even when there was no particular excitation of the spectator H atoms, a significant redistribution of the energy could occur. This implies that the spectator-graphite bond can behave as a reservoir of energy during the reaction, which can then be released or retained during the H_2 desorption. Meijer *et al* also found that with the spectator hydrogen present, the highest excited states of the newly formed H_2 were $v'' = 2$ and $v'' = 3$. A later study by the same group investigated isotope effects in molecular hydrogen formation.²⁴ Again a time-dependent wave packet method was used to study the associative desorption of $\text{HD}(v, J)$ and $\text{D}_2(v, J)$. The results showed that the molecules were ro-vibrationally excited and translationally hot, significant isotope effects and possible resonance transitions during the recombination reaction were determined.

Chapter 1. Introduction

Jackson and Lemoine³⁶ have studied the formation of molecular hydrogen *via* the ER mechanism on a variety of surfaces, both metal and graphite. The results obtained indicated that the collision cross-sections for the single-collision ER process on metal surfaces were small, suggesting hot-atom mechanisms are important for H₂ formation. Whereas for graphite surfaces the cross-sections were large for the reaction of H_(g) with H_(ads).

Sha, Jackson and Lemoine went on to study the ER H₂ formation mechanism by electronic structure studies coupled with quantum scattering calculations.⁴⁰ Hydrogen atoms that were originally chemisorbed and physisorbed before reacting with an H atom from the gas phase were studied. For the chemisorbed case two scenarios were considered: firstly, with the graphite held in a fixed puckered position during the reaction and secondly, where the graphite lattice is allowed to fully relax. The reaction cross-sections were found to be large, except in two cases: (a) when the H atom was chemisorbed there was a barrier in the entrance channel, resulting in a reaction cross-section of zero for small incident energies and (b) for the physisorbed H atom, the reaction cross-section decreased rapidly when the incident energy of the impinging gas phase atom increased. All the reactions investigated led to considerable vibrational excitation but only a small amount of rotational excitation. Molecular hydrogen that had formed from the chemisorbed state had approximately 1 eV of translational energy, but H₂ from the physisorbed state had almost zero translational energy.

The most recent study by the Jackson group looked at the sticking of H and D atoms on a graphite surface and the effects of coverage and energy dissipation.⁴¹ Classical trajectory methods were utilised and DFT calculations were carried out to model the potential energy surface, in 3D, of the incident atom. The incident atoms were chemisorbed to the surface, it was found that the sticking cross-section reached a peak at 0.5 eV and then falls to zero as the atom becomes more energetic, resulting in a destabilisation of the C-H bond. Jackson and co-workers estimated that the sticking probability for D atoms at 150 K was in the range of 5 – 10%. They also observed that the sticking probability at the

Chapter 1. Introduction

para site, directly across the six fold carbon ring from an already adsorbed H atom, can be four times larger than the zero coverage sticking cross-section.

A considerable body of work investigating the formation of molecular hydrogen has been carried out by the Sidis group. One of the earliest studies by Jeloica and Sidis³⁷ revealed that, on a graphite surface, there is a 0.2 eV barrier to chemisorption. It was observed that the chemisorption site on a graphite ring was located at an 'on-top' site of a carbon atom; for chemisorption to occur, significant surface relaxation is required. In contrast physisorption was completely site independent and compatible with a high mobility of H atoms on the surface. The results of these calculations have had a significant impact as they indicate that the ER mechanism can occur for both chemisorbed and physisorbed atoms, whereas the LH mechanism can only arise when the atoms are physisorbed, as the chemisorbed atoms are restricted from diffusing across the surface.

Work by Morisset *et al* has been carried out on the formation of H₂ on graphite surfaces *via* both the ER and LH mechanisms.^{25,26} The dynamics of the reaction and the important role of surface relaxation have been considered. For the Eley-Rideal mechanism it was observed that a large amount of energy was released upon the formation of the H₂, with $\nu'' = 7$ having the highest population. For the studies of the LH mechanism, H atoms that were initially physisorbed on the surface were considered. These atoms diffused across the surface, reacted and then desorbed as H₂. It was again determined that a large amount of the formation energy goes into vibration of the nascent H₂. The most recent study by the Sidis group⁴² again investigates the ER formation mechanism but allows the graphite surface to fully relax during the reaction. It was observed that upon the arrival of a gas phase H atom, the adsorbant C atom is attracted to the H and causes the surrounding surface atoms to pucker up. The hillock that is formed as a result of this remains puckered until the nascent H₂ molecule is released. As a result of this movement within the surface more of the 4.5 eV binding energy is imparted to the surface, reducing the highest populated vibrational state of the H₂ from $\nu'' = 7$ to $\nu'' = 4$ or 5.

Chapter 1. Introduction

The Sidis group have also carried out further studies of the Langmuir-Hinshelwood mechanism⁴³ on a carbonaceous porous material, allowing the nascent H₂ to collide with a pore wall before desorbing. The results indicated that in the first 5 to 15 impacts of the H₂ with the pore walls there was a substantial conversion of vibrational energy into rotation. The energy conversion from vibration to rotation mediates the flow of the molecule's internal energy into translational energy and surface heating. The molecules are cooled but the internal energy change is slow, in fact only 0.10 eV of the ~4.5 eV binding energy is lost per impact. Despite these losses the rotational and vibrational excitation was still observed to be high with $\nu'' = 0 - 10$ and $J'' = 10 - 30$ (Figure 1.7.1).

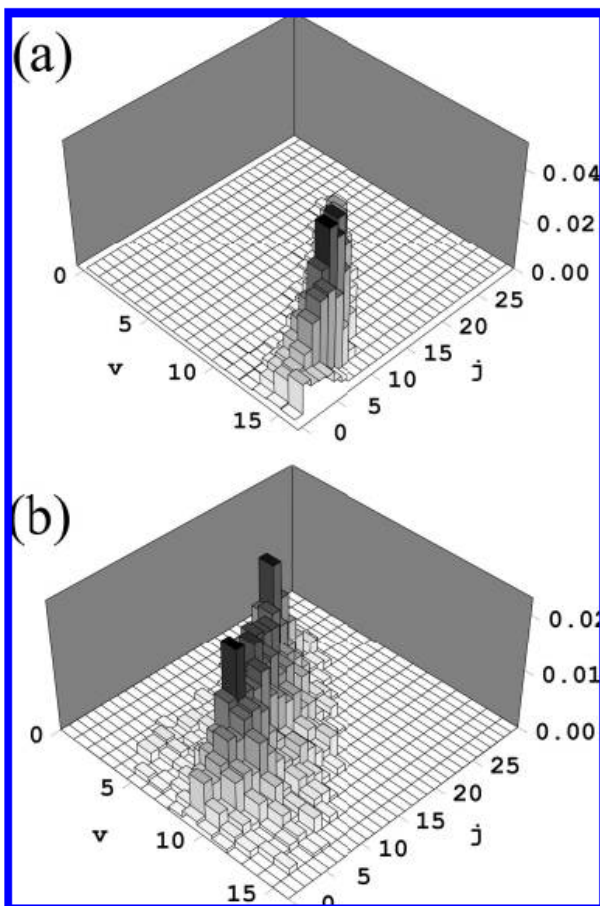


Figure 1.7.1 Figure taken from the work of Sidis *et al*⁴³ on the Langmuir-Hinshelwood formation mechanism. Figure depicts the ro-vibrational distribution for H₂ formed on a flexible grapheme surface at 200 K. (a) nascent H₂ molecules from formation *via* LH mechanism. (b) reflected molecules after one collision with the surface.

Chapter 1. Introduction

Cazaux and Tielens have modelled H_2 formation on ‘grain surfaces’ under ‘astrophysically relevant conditions’.^{11,34} The results of the two studies described here indicate the efficiency of the LH formation mechanism. It was observed that molecular hydrogen can form efficiently on grains over a range of surface temperatures, from ~ 6 K to ~ 300 K. It was determined that up to approximately 100 K H_2 forms by the recombination of a physisorbed H atom with a chemisorbed H atom and this process was highly efficient. At higher temperatures physisorbed H atoms desorb too quickly from the surface to react, hence two chemisorbed H atoms were required to form H_2 . The reaction of two chemisorbed H atoms was less efficient than the reaction between the physisorbed and chemisorbed atoms.¹¹ Cazaux and Tielens developed a model for hydrogen formation on grain surfaces which takes into account physisorbed and chemisorbed atoms along with quantum mechanical diffusion and thermal hopping; the results from this model were compared with the experimental data of Pirronello *et al.*^{38,44,45} The time evolution of the system was found to be governed by the binding energies and barriers against diffusion of the adsorbed species. At low temperatures physisorbed H atoms reacting with chemisorbed H atoms was found to be highly efficient. At higher temperatures the chemisorbed atoms became mobile and could also recombine.

When comparing the results from these theoretical studies to experimental work and to the conditions of the ISM it is important to note that grain surfaces are modelled as ‘perfect’ or ‘ideal’, which of course is not the case in experiment or in the ISM.

1.7.2 Experimental Studies

In the experimental field there have been a number of studies of the formation of molecular hydrogen on various surfaces of astrophysical interest carried out by Pirronello and co-workers. These investigations have included work on silicate surfaces, modelled by olivine, amorphous carbon surfaces and recently amorphous water-ice surfaces. Their initial study involved the olivine surface on which they carried out temperature programmed desorption (TPD) experiments.⁴⁵ Rather than studying the formation of H_2 , HD was probed from H and D atoms created by radio frequency dissociation of H_2 and D_2 . This method prevented any undissociated H_2 or D_2 from affecting the results, as only

Chapter 1. Introduction

HD formed on the surface would be in the vacuum chamber. The results indicated that the recombination efficiency (the sticking probability, S , multiplied by the probability of recombination upon H-H encounter, γ) was lower than model-based estimates. However, it was observed that the recombination efficiency increased as the surface temperature decreased, but at astrophysically relevant grain temperatures (10 – 15 K) the recombination efficiency was $\sim 0.03 - 0.05$, considerably lower than the value determined by Hollenbach and Salpeter of 0.3.⁴⁶ Pirronello *et al* proposed that their results could be reconciled with average estimates of the recombination rate from astronomical observations, if the actual surface of the dust grain and the surface area is larger than the estimates considered in the models.

Follow up work by the Pirronello group,⁴⁴ again carried out measurements of the HD formation on an olivine slab as a function of surface temperature. They observed that there are two main regimes of H surface coverage that are astrophysically important: low coverage at low surface temperatures and higher coverages that are still below a monolayer coverage. The higher coverages showed first order desorption kinetics, which suggests that H_2 molecules formed at low temperatures do not desorb until the temperature is raised. In contrast, in the low coverage regime the kinetics were observed to be second order, indicating that the atoms remain on the surface as H atoms and also stayed localised without recombining. These results indicate that the ~ 4.5 eV of binding energy released on the formation of H_2 does not immediately force the H_2 into the gas phase and that a significant amount of energy could be deposited into the surface. A similar set of experiments have been carried out more recently by the Pirronello group on amorphous silicate surfaces.⁴⁷ Similar observations were made, that the recombination efficiency H atoms strongly depends on the surface temperature and that H_2 formation could take place on amorphous silicate surfaces at temperatures relevant to the ISM.

The Pirronello group replaced the olivine slab with a ‘carbonaceous grain’ analogue and studied the formation of molecular hydrogen on this surface.³⁸ As with the olivine the results showed that the recombination of HD was thermally activated. However, with the carbonaceous grains the activation temperature was higher than with olivine and the

Chapter 1. Introduction

recombination efficiency was also higher, despite the experiments being carried out under the same conditions as the olivine experiments. The energy barrier for H₂ formation was found to be higher for carbonaceous materials than for silicates as the H is more strongly bound to the carbonaceous surface than the insulating silicate surface. This will result in the residence of the H atoms on the carbonaceous surface being longer, allowing the atoms more time to overcome the barrier for recombination if they have enough energy.

To analyse the results of their experiments Pirronello and co-workers have developed a complex rate equation model that is applicable to both the olivine and carbonaceous experiments.²¹ It was assumed that the mechanism of formation was Langmuir-Hinshelwood and hence the formation of H₂ was diffusion-limited. Investigations showed that a model in which HD desorbed from the surface immediately upon formation could not reproduce the experimentally obtained desorption curves. Differences in the recombination efficiency for the silicate surfaces compared with the carbonaceous surfaces were determined. Recombination on the silicate surfaces was more efficient at temperatures that are too low to be astrophysically relevant, however, the amorphous carbon surfaces enable the most efficient recombination of H atoms at temperatures of ~8 – 14 K, temperatures which are more applicable to interstellar clouds.

The most recent studies by the Pirronello group have focused on the formation of H₂ on amorphous water ice surfaces.^{48,49} In the first of these studies⁴⁸ both low and high density amorphous ice were considered. Low density amorphous ice (LDI) is obtained by depositing water vapour on an inert surface at 77 K, the resulting solid has a density of $0.94 \pm 0.03 \text{ g cm}^{-3}$. This LDI has been found to be microporous in nature, hence increasing the effective surface area of the film. In contrast, high density amorphous water ice (HDI) is made by depositing water vapour on a substrate held at ~10 K and has a density of $1.1 \pm 0.1 \text{ g cm}^{-3}$. The experiments carried out showed that the recombination efficiency of hydrogen was affected by the surface structure and that the recombination efficiency increased when the surface temperature was ~10 K. It was concluded that H₂ formation would be more efficient on the LDI. The second study by Pirronello and co-workers⁴⁹ investigated the kinetic energy of D₂ molecules desorbing from amorphous

Chapter 1. Introduction

water ice, using TPD data. The results suggested that the nascent molecules desorbed from the surface as if they were thermally equilibrated. Finally, Pirronello *et al* returning to the LDI and HDI water ice surfaces, concluded that the formation of H₂ both surfaces was efficient in the temperature range ~14 – 20 K.⁵⁰

Gough *et al* studied the formation of vibrationally excited hydrogen from a carbon surface, with the surface held at temperatures ranging from 90 – 300 K.¹³ These experiments showed that H₂ could form in vibrationally excited states and the states up to $\nu = 7$ were detected. The techniques used here were based on ‘dissociative attachment of low energy electrons to ro-vibrationally excited H₂’. The temperatures at which this work was carried out are too high to be grain temperatures in the ISM. Gough and co-workers concluded that H₂ could be expected to form in ro-vibrationally excited states on dust grain surfaces in the ISM.

Work carried out by Zecho *et al* has focused on the adsorption of H and D atoms on highly orientated pyrolytic graphite (HOPG) surfaces.⁵¹ These experiments involved the use of thermal desorption (TDS), electronic (ELS) and high-resolution electron-energy-loss (HREELS) spectroscopies. Zecho and co-workers used 2000 K hydrogen and deuterium atom sources to obtain chemisorbed D atoms on the surface, the temperature of which was 150 K. The adsorbed layers of D atoms were then subjected to a beam of H atoms and the resultant HD was monitored using a quadrupole mass spectrometer (QMS). The results of these experiments confirmed the 0.2 eV barrier to chemisorption that had been determined theoretically.³⁷ Further work by this group investigated the effect of adsorbed water on the graphite surface on the ER reaction of H and D atoms.⁵² It was discovered that a water monolayer on the surface prevented the adsorption of 2000 K H atoms and that an overlayer of water above a chemisorbed layer of D atoms also prevented reaction.

The group of Zecho *et al* have also used low energy electron diffraction (LEED) and scanning tunnelling microscopy (STM) to study the adsorption of H and D atoms on graphite⁵³ and on surfaces that have been bombarded with Ar.⁵⁴ The LEED studies

Chapter 1. Introduction

showed that the H and D atoms randomly adsorb on the surface and the STM images indicated that C atoms would pucker out of the plane of the surface when D atoms were adsorbed on the surface. Further TDS studies by Zecho and co-workers looked at the chemisorption of D atoms on terraces and terrace edges of HOPG and natural graphite surfaces.⁵⁵ The spectra obtained in this study showed that for D atoms adsorbed on (0001) terraces, there were 2 peaks and a shoulder that were specific to D atoms on terraces and not related to any defects in the surface. Deuterium atoms that were adsorbed at terrace edges were found to react with the graphite to produce hydrocarbons which then desorbed in the TDS runs. More recent studies by Zecho *et al* have involved further STM experiments of D atoms on graphite.⁵⁶ These experiments showed that at low D coverages only isolated D atoms were observed. However, when the coverage was increased pairs of D atoms dominated the surface. Three different types of deuterium dimers were identified: the ortho pair and two different arrangements where the D atoms are paired across adjacent C₆ rings.

The group of Hornekaer *et al* have investigated the influence of morphology of the surface on both H₂ formation in the ISM and on D₂ desorption kinetics. For both studies TPD was employed and the surface consisted of films of amorphous solid water (ASW) on a copper substrate.^{17,18} The morphology of the ice surface was found to have a significant effect on the fate of the 4.5 eV of binding energy released upon the formation of H₂. The TPD data showed a large HD signal from porous ice surfaces but when the surface was non-porous little or no formation of HD was observed. This result could be explained by HD molecules that had formed in the pores, thermalising with the surface within the pores and then desorbing when the temperature was increased to carry out the TPD. The lack of HD signal for the non-porous surface suggested that the molecules had immediately desorbed upon formation, possibly in highly vibrationally and rotationally excited states.

Hornekaer and co-workers have also considered the chemisorption of deuterium atoms on graphite surfaces.¹⁹ This work has been carried out by imaging D atoms adsorbed on a HOPG surface using STM imaging in conjunction with TPD studies (Figure 1.7.2). Hot (2200 K) D atom beams were used to chemisorb atoms onto the graphite surface and the

adsorption of these atoms was probed using TPD experiments. STM images showed that the deuterium on the graphite surface had two different characteristic structures, one with the D atoms in the ortho position, adjacent on the graphite ring, and the other with the D atoms bonded to opposite carbon atoms (para) in a graphite hexagon. These results are similar to those obtained by Zecho *et al.*⁵⁶ The experiments of Hornekaer *et al* showed that the recombination path of D atoms occurs through the para structure. Further work by the Hornekaer group has confirmed this lowest energy recombination path for the para dimer, this was achieved using laser assisted associative adsorption (LAAD) combined with TPD experiments.²⁰ To indentify the velocity distributions of the chemisorbed $H_2(D_2)$ desorbing at different angles from the graphite surface time-of-flight measurements were utilised. It was observed that the nascent $H_2(D_2)$ molecules desorbing normal to the surface have translational energy independent of the temperature increase induced by the laser, this indicates that for these molecules, the translational energy comes only from the desorption energy. The average translational energy of the $H_2(D_2)$ moving normal to the surface was found to be 1.3 eV, this left approximately 60% of the desorption energy to flow into the surface or be converted into vibrational excitation of the molecule.

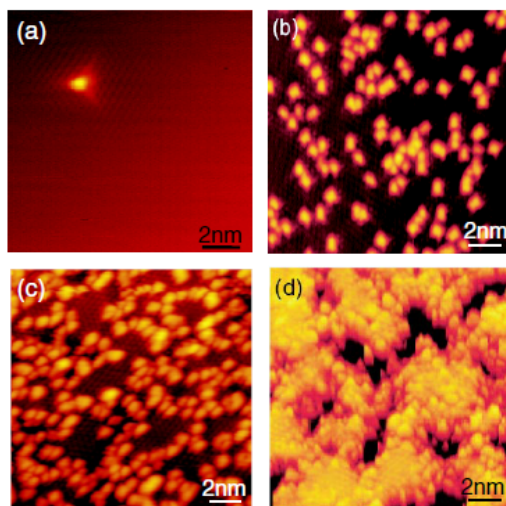


Figure 1.7.2 Figure taken from the work of Hornekaer *et al.*¹⁹ Figure shows STM images of a graphite surface after increasing doses of D atoms, (a) one bright spot on the graphite surface, (b) after dosing D atoms for 1 min, (c) after dosing D atoms for 6 mins and (d) after dosing D atoms onto the graphite for 24 mins.

Chapter 1. Introduction

The most up-to-date studies by the Hornekaer group have again used STM imaging to study the structures of metastable hydrogen adsorbed on an HOPG surface.⁵⁷ Two different structures were observed, a hydrogen dimer structure that was present after thermal annealing to 525 K at both high and low hydrogen coverages. The other structure was more complex and not previously observed. This structure appeared only after thermal anneals at high hydrogen coverage and was observed to exhibit long range orientation within each micro-crystalline region on the HOPG surface.

The group of Lemaire and co-workers has focused on the recombination of D atoms and the interactions of D₂ on amorphous water ice surfaces at temperatures ranging from 8 to 30 K.⁵⁸ They have performed TPD experiments, detecting the nascent D₂ with a QMS. It was observed that the sticking coefficient of D₂ increases linearly with the number of deuterium molecules already adsorbed on the surface. The formation of D₂ from adsorbed D atoms was found to be a prompt reaction with the nascent D₂ desorbing immediately and these newly formed molecules had considerable vibrational excitation ($\nu = 1 - 7$). The recombination efficiency increased with the presence of D₂ molecules already adsorbed on the surface, this is probably due to an increase in sticking probability of the atoms. Results from these experiments also showed that when D₂ is present on the amorphous ice surface and the temperature is increased, the recombination efficiency decreases and reaches zero at 13 K. Lemaire and co-workers have also studied the different adsorption energies for the addition of ortho- and para- D₂ to an amorphous ice surface.⁵⁹ The desorption profiles of ortho- and para- D₂ are different, this is due to the shift in the adsorption energy distribution of the two lowest rotational states. Molecules in $J'' = 1$ are generally more strongly bound than those in $J'' = 0$. The experiments carried out in this study estimate this energy difference to be 1.4 ± 0.3 meV.

Later work by Lemaire *et al* investigated the mobility of D atoms on porous amorphous water ice surfaces.⁶⁰ In these experiments O₂ was deposited on the surface prior to the D atoms and then TPD experiments were run, simultaneously monitoring O₂ and D₂ desorption. The results showed that the amount of O₂ that desorbs from the surface decreases as the D atom exposure time is increased. The O₂ was easily destroyed by the D atoms which, indicates that the D atoms could be mobile at 10 K on the water ice

Chapter 1. Introduction

surface. Using a simple rate equation they determined the barrier to desorption to be 22 ± 3 meV, this implies that hydrogenation can take place efficiently on interstellar dust grains.

Perry and co-workers designed and commissioned the experiment used in this thesis. Initially the ro-vibrational distribution of H₂ molecules formed on a cold (30 – 50 K) HOPG surface was investigated.^{61,62} The laser technique of resonance enhanced multiphoton ionisation (REMPI) was employed to successfully measure H₂ formed in the ro-vibrationally excited states $v'' = 1, J'' = 0 - 3$. The rotational temperature of the nascent H₂ was calculated and found to be much greater than the temperature of the surface. These results implied that a considerable proportion of the 4.5 eV binding energy is deposited into the surface. Creighan *et al* continued the work on this experiment and found that the $v'' = 1$ and 2, $J'' = 0 - 4$ states are populated when both H₂ and HD form on the HOPG surface.⁶³ These results compare well with aspects of work by both the Pirronello group and the Hornekaer group. Pirronello *et al* suggested that some of the binding energy must be deposited into the surface given that the molecules do not appear to desorb immediately upon formation.⁴⁴ However, the detection of ro-vibrationally excited molecules by Perry *et al* implies that some of the molecules must desorb immediately, as proposed by Hornekaer and co-workers.¹⁷

Before all the studies reviewed in this section, experiments on the adsorption of hydrogen on cold (4 K) surfaces were carried out by Govers *et al*.⁶⁴ Although this experiment was not initially designed to be applicable to the ISM the results prove to be useful when considering the hydrogen formation problem. This group used molecular beams of H₂ and D₂ incident on a liquid helium cooled bolometer as an energy detector, to investigate the sticking and accommodation of molecular hydrogen and deuterium on low temperature substrates. Investigations into the recombination of atomic hydrogen physisorbed on low temperature substrates, taking into consideration the coverage of molecular hydrogen were also carried out by Govers and co-workers.⁶⁵ From these experiments they were able to extract the sticking probability and accommodation coefficient of H₂ on the cooled surface on the bolometer, as a function of H₂ coverage. These results were obtained by monitoring the energy deposited in the bolometer as a

function of time; the associated temporal behaviour of the newly formed H_2 was monitored using a mass spectrometer. A set of experiments were run with the bolometer surface pre-dosed with D_2 and then H atoms deposited on top. The sticking probability and reaction probability of the incident H atoms were determined as a function of D_2 coverage. Govers and co-workers found that the H atoms were highly mobile on the surface, even at the very low temperature of 4 K and that recombination could also arise at these temperatures; this contradicts the results of Pirronello *et al.*^{39,45,46} This data from the Govers group casts doubt on the assumption made by Pirronello and co-workers that any H or D on their surface would be immobile at low temperatures and hence no reactions can occur until the surface is heated to run a TPD experiment. The work of Govers *et al* further validates the interpretation of the Hornekaer *et al* experiments that saw a reduced HD signal from their non-porous surface. If the atoms had recombined and desorbed at a lower temperature, no signal would be expected when the TPD run is performed.

1.8 The UCL Cosmic Dust Experiment

Despite the increasing body of work that has been carried out on the formation of hydrogen on interstellar dust grain surfaces, there are still some unanswered questions. In particular there is still minimal experimental data on the distribution of the ~ 4.5 eV of binding energy upon the formation of H_2 ; how much of this energy goes into rotational, vibrational and translational excitation and how much is deposited into the grain surface? These questions may have a significant impact on the overall energy budget and chemistry of the dust clouds. For example, faster reaction rates may occur for H_2 molecules with higher internal excitation. Highly excited H_2 will also be easier to ionise, either directly or by charge transfer with H^+ , which is usually an endothermic reaction. This could lead to higher abundances of H_3^+ , which as discussed in Section 1.3 is of great interstellar importance. Indeed, astronomers have observed that the column densities for H_3^+ are in fact larger than anticipated in the diffuse ISM.⁶⁶ It has been proposed by McCall *et al* that an enhanced rate of H_2 ionisation may be able to account for the increased abundance of H_3^+ , which could be possible if H_2 was formed in vibrationally excited states. Another plausible suggestion for the high abundance of H_3^+ is a reduced

electron fraction and a smaller value for the H_3^+ dissociative recombination rate than implied by experiments.⁶⁶ Large amounts of translationally excited H_2 could result in local heating of the dust clouds *via* inelastic scattering.

The UCL cosmic dust experiment has been designed to probe the ro-vibrational distribution of H_2 , and other small molecules, formed on an interstellar dust grain analogue. The experiment utilises the well established technique of resonance enhanced multiphoton ionisation (REMPI) in conjunction with time-of-flight (TOF) mass spectrometry, to state selectively ionise and detect nascent H_2 molecules. The experiments are carried out under vacuum and the surface temperature is 15 K, conditions designed to mimic the interstellar medium.

1.9 Interstellar Ices and OCS in the ISM

As mentioned previously dust grains in dark clouds are often coated with icy mantles from the freeze out of simple molecules. The composition of these ices can vary in different regions of the ISM but they have been observed to predominantly consist of molecules such as H_2O , CO and CO_2 , with species such as methanol, methane, formaldehyde, OCS and formic acid also having relatively high abundances.^{30,32} However, in the gas phase the only molecule abundant enough to account for the deposition of its ice by freeze-out in a short enough timescale is CO . Therefore, an alternative mechanism for the formation of the other molecules observed in the interstellar ices is required. Similarly to H_2 formation, the formation of these other molecules is believed to take place on the dust grain surfaces, where the nascent molecules are retained.⁶⁷

In the ISM there are comparatively few molecules that contain sulphur, and the majority of these compounds include hydrogen, so OCS is in the minority. OCS is most commonly found in warm dense clouds, where it has a column density of $\sim 2 \times 10^{15} \text{ cm}^{-2}$.⁶⁸ However, as mentioned above, OCS is also a constituent of interstellar ices and hence can be found in dark clouds. Some of the first observations of OCS in dark clouds were made by Matthews *et al* in 1987, where they observed that OCS has a mean fractional abundance

Chapter 1. Introduction

relative to hydrogen of $\sim 3 \times 10^{-9}$, a value that is approximately four times greater than the abundance observed for giant molecular clouds. There have been a variety of mechanisms proposed for the formation of OCS, some that would take place in the gas phase and others in dust grain surfaces by the reaction of HCO^+ and SH^- . Millar⁶⁹ suggested that the gas phase formation of OCS would proceed in the following way:



Whereas Mitchell *et al*⁷⁰ thought with H_2 densities greater than 10^3 cm^{-3} that the route to the production of OCS was as follows:



Finally, Watt and Charnley⁷¹ proposed that radiative association was the predominant reaction pathway:



There has not been much experimental work carried out on the gas phase formation of OCS, however there has been some work done on the formation of OCS on interstellar ices. It is now apparent that when molecules such as CO, CO_2 , H_2S and SO_2 , all of which are observed in ices, are on the surface of dust grains and it is possible to form OCS when the grain is exposed to background radiation.⁷² Interstellar ices are not the only extraterrestrial source of OCS, it has been observed in the atmosphere of both Venus⁷³ and Jupiter⁷⁴ as well as in cometary comae.⁷⁵

1.10 Molecular Dications in the ISM and Planetary Atmospheres

Molecular dications are believed to be the building blocks for some of the largest molecules observed in the ISM such as PAHs and C_{60} . Experimental work has been carried out by Roithová and Schröder that indicates that dications such as $\text{C}_7\text{H}_6^{2+}$ can be involved in reactions with C_2H_2 to form larger hydrocarbons.⁷⁶ They observed that these

reactions can take place at low temperatures and pressures, conditions relevant to the ISM. It is thought that molecules such as acetylene undergo reactions to produce hydrocarbons up to C_7H_n . Once at this size any interactions with background radiation will cause ionisation and it is these dications that can go on to react to produce the PAHs so readily observed in the ISM. It has been proposed that doubly charged PAHs should be present in the ISM and these molecules have been included in models for the formation of larger hydrocarbons.⁷⁷ Similarly, it is proposed that C_{60} could exist in the ISM and research has shown that there are several mechanisms available for the double ionisation of C_{60} in interstellar and circumstellar environments.⁷⁸ These mechanisms include sequential photoionisation, direct double ionisation by cosmic rays and an electron transfer/electron detachment reaction with He^+ . The C_{60}^{2+} ions can go on to react with a variety of other hydrocarbon species resulting in long chain molecules.⁷⁹

Smaller molecular dications have been predicted to be present in planetary atmospheres, including Earth's.⁸⁰ Species such as N_2^{2+} , O_2^{2+} and O^{2+} are believed to be present in Earth's atmosphere and models have been designed to probe their formation and destruction. Similarly it is thought that the atmosphere of Mars⁸¹ is likely to contain CO_2^{2+} ions that are produced on the dayside by the ionisation of carbon dioxide and can be destroyed by dissociative recombination with thermal electrons or by chemical reactions with CO_2 . Titan's atmosphere is also predicted to contain doubly charged ions such as N_2^{2+} ; again these ions are produced on the dayside through the ionisation of nitrogen and lost by dissociative recombination with thermal electrons or reaction with N_2 or CH_4 . It is thought that it should be possible to detect these ions as 10% of the ions are created in an excited state which should give observable fluorescence.⁸²

1.11 Ionisation Cross-Sections

The ionisation of many small molecules and their subsequent fragmentation into monocations and dications can be probed by measuring the ionisation cross-section. In this thesis the ionisation cross-section of OCS which, as discussed above, is an astrophysically relevant molecule, has been investigated. The ionisation of small molecules is an important process in many environments, in planetary atmospheres

photons and cosmic rays, of high enough energy, can cause ionisation. Many plasmas used for industrial purposes i.e. in the semiconductor industry, rely on the ionisation of small molecules such as CF_4 ,⁸³ Cl_2 ,⁸⁴ NF_3 ,⁸⁵ N_2O ⁸⁶ and BCl_3 .⁸⁷ To be able to reliably model the environments where dissociative ionisation can occur, information about the formation efficiency of the molecular ion and any ionic fragments is required. Mass spectrometry can provide such information, the yield of the ionic products formed from an ionising event are expressed in the form of total, σ_c , (equation 1.11.1) and partial, $\sigma[X^{m+}]$, (equation 1.11.2) ionisation cross sections (PICS), which are defined as:

$$\sigma_c = \frac{\sum N[X^{m+}]}{I_0 n l} \quad 1.11.1$$

$$\sigma[X^{m+}] = \frac{N[X^{m+}]}{I_0 n l} \quad 1.11.2$$

where $N[X^{m+}]$ represents the total number of ions, X^{m+} formed by ionisation events involving the formation of X^{m+} , I_0 is the initial electron flux, l is the distance that the electrons have to travel through a target gas of number density, n .

The measurement of accurate PICS requires a degree of care. Initially the identification of the products from the ionisation event is required and it must also be ensured that all of the ions are detected with the same efficiency, regardless of their initial kinetic energy or mass. Early experiments designed to study ionisation utilised quadrupole mass spectrometers (QMS) or magnetic sector instruments. The collection of energetic ions in these instruments was inefficient in comparison with that for ions of lower energies. However, in more recent experiments the collection of high energy ions has been considerably more accurate and such measurements indicate that multiple ionisation events can contribute significantly to the total ionisation yield.^{84,86,88,89}

1.12 Multiply Charged States of Small Molecules

Multiply charged states of small molecules are generally very short-lived and unstable in the gas phase. This is due to the proximity of the two or more like charges and as a result the ions rapidly fragment to charge separated products. These fragments can possess a large amount of kinetic energy; approximately 6 eV is a typical value for an ion pair from a diatomic dication.⁹⁰ However, given that some molecular dications have been detected by the use of mass spectrometry, indicates that the dications must have a relatively long lifetime as they must survive for at least 1 μ s to be detected. There are several well known examples of small molecular dications that have at least one electronic state in which there is a barrier to charge-separating dissociation.⁹¹ This barrier allows the molecule to possess kinetic stability, although many are thermodynamically unstable as the potential well lies above the asymptote for charge separation; such electronic states are termed metastable.

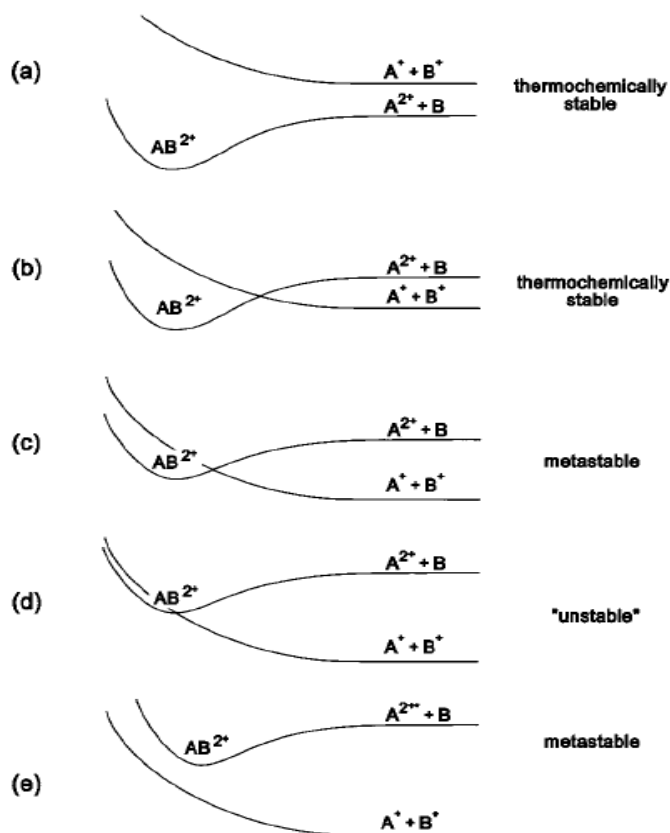


Figure 1.12.1 Schematic representation of the potential energy curves for a dication AB^{2+} , taken from reference⁹²

Chapter 1. Introduction

The potential well of metastable dications can support several bound vibrational levels and even some ‘continuum’ levels above the barrier.⁹³ The amount of vibrational excitation that a molecular dication possess can therefore significantly affect its lifetime. Low lying vibrational states are effectively trapped behind the barrier to charge separation so these states should be long-lived. However, high lying vibrational states can tunnel through the barrier, hence the lifetimes for these states will be considerably shorter. The most probable decay pathway for dications in low lying vibrational states is curve crossing to repulsive electronic states (Figure 1.12.2),⁹³ or alternatively a repulsive electronic state may be reached by the metastable ion emitting a photon.

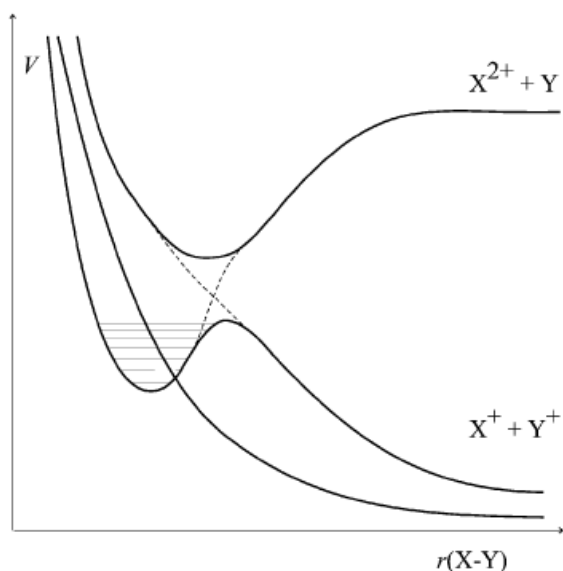


Figure 1.12.2 Schematic potential energy curves describing the avoided crossing of two potentials, one corresponding to monocation-monocation potential and the other to dication-neutral potential, forming a thermodynamically unstable, but long-lived metastable dication. The vibrational levels for a metastable state are indicated, the lifetimes of these states are influenced by curve-crossings to dissociative potentials.⁹³

A less probable decay path is radiative charge transfer, which has been demonstrated for doubly charged argon dimers where the double charge is localised on one of the argon atoms.^{95,96} The localised double charge is spread over the two argon atoms as a photon is emitted from the dimer and the electrostatic repulsion causes the dimer to fragment:



There are two interpretations for the existence of metastable dication states. Firstly, that in these states the Coulombic repulsion between the two like charges is overcome by the bonding interaction to produce a metastable well. This model has been found to work well for F_2^{2+} where the potential energy curves have been well reproduced by using the curves for an isoelectric neutral species and adding the Coulomb repulsion potential.⁹⁴ However, for molecules which have a small internuclear separation and hence both positive charges can be on one atom, such as HCl^{2+} , this model is not always obeyed. The second and more commonly used interpretation, as shown in Figure 1.12.2, considers the potential energy surfaces of a molecular dication as an adiabatic composite of a pair of diabatic surfaces which describe asymptotic dissociation, one to a pair of cations and the other to a dication and a neutral. The relative energy of the two dissociation asymptotes and the bound minimum determine the thermodynamic stability of the molecular dication.

There are many formation routes for molecular dications including: photoionisation or bombardment by high energy particles such as high energy electrons or protons. In experimental investigations both ionisation methods can be employed and both techniques can yield thermochemical data⁹⁵ as well as electronic structures from multiple ion/electron coincidence studies.⁹⁰ Information about dication energetics can also be obtained from charge stripping⁹² and double charge transfer experiments.⁹⁶ As well as these direct methods of dication production, dissociative double ionisation of neutral molecules may also form doubly charged fragments. The electron impact ionisation of CF_4 can result in fragmentation to form CF_2^{2+} in an electrostatic state that has a long enough lifetime to be detected.



To be able to understand the chemical and physical properties of molecular dications the development of new experimental techniques, such as multiple ion/electron coincidence

Chapter 1. Introduction

techniques, Doppler-free kinetic energy release spectroscopy⁹⁷ and threshold photoelectron coincidence spectroscopy, has been invaluable. In this thesis the technique of multiple ion/electron coincidence has been used to probe OCS and the resulting ionic fragments.

1.13 Summary

This chapter has introduced the background for both the UCL Cosmic Dust experiment and the ion/electron coincidence experiment used to probe OCS. An overview has been given of what is currently known in the field of astrochemistry. The following chapters will describe the experimental apparatus and the results obtained regarding the internal energy distribution of molecular hydrogen formed on a graphite surface under conditions designed to reproduce the interstellar medium. Later chapters discuss the experimental set-up for the electron impact ionisation experiment and the results obtained from that investigation.

1.14 References

- 1 J. E. Dyson and D. A. Williams, *The Physics of the Interstellar Medium*, 2nd ed ed. (Institute of Physics, Bristol, 1997).
- 2 T. W. Hartquist, Williams, D.A., *The Chemically Controlled Cosmos*, 1 ed. (Cambridge University Press, 1995).
- 3 G. B. Field, Somervil.Wb, and K. Dressler, *Annual Review of Astronomy and Astrophysics* **4**, 207 (1966).
- 4 G. R. Carruthers, *Astrophysical Journal* **161**, L81 (1970).
- 5 L. Spitzer and E. B. Jenkins, *Annual Review of Astronomy and Astrophysics* **13**, 133 (1975).
- 6 B. Richter P., H., Margggraf, O., and Boer K.S.D., *H₂ absorption line measurements with ORFEUS in Molecular Hydrogen in Space*. (Cambridge University Press, 2000).
- 7 W. Duley and D. A. Williams, *Interstellar Chemistry*. (Academic, London, 1984).
- 8 T. N. Gautier III, U. Fink, R. R. Treffers, and H. P. Larson, *Astrophysical Journal* **207**, L129 (1976).
- 9 O. Biham, I. Furman, N. Katz, V. Pirronello, and G. Vidali, *Monthly Notices of the Royal Astronomical Society* **296**, 869 (1998).
- 10 S. Cazaux and A. Tielens, *Astrophysical Journal* **577**, L127 (2002).
- 11 S. Cazaux and A. Tielens, *Astrophysical Journal* **575**, L29 (2002).
- 12 A. J. Farebrother, A. J. H. M. Meijer, D. C. Clary, and A. J. Fisher, *Chemical Physics Letters* **319**, 303 (2000).
- 13 S. Gough, C. Schermann, F. Pichou, M. Landau, I. Cadez, and R. I. Hall, *Astronomy and Astrophysics* **305**, 687 (1996).
- 14 R. J. Gould and E. E. Salpeter, *Astrophysical Journal* **138**, 393 (1963).
- 15 J. M. Greenberg, *Surface Science* **500**, 793 (2002).
- 16 D. J. Hollenbach and E. E. Salpeter, *Astrophysical Journal* **163**, 155 (1971).
- 17 L. Hornekaer, A. Baurichter, V. V. Petrunin, D. Field, and A. C. Luntz, *Science* **302**, 1943 (2003).
- 18 L. Hornekaer, A. Baurichter, V. V. Petrunin, A. C. Luntz, B. D. Kay, and A. Al-Halabi, *Journal of Chemical Physics* **122** (2005).
- 19 L. Hornekaer, E. Rauls, W. Xu, Z. Sljivancanin, R. Otero, I. Stensgaard, E. Laegsgaard, B. Hammer, and F. Besenbacher, *Physical Review Letters* **97** (2006).
- 20 L. Hornekaer, Z. Sljivancanin, W. Xu, R. Otero, E. Rauls, I. Stensgaard, E. Laegsgaard, B. Hammer, and F. Besenbacher, *Physical Review Letters* **96** (2006).
- 21 N. Katz, I. Furman, O. Biham, V. Pirronello, and G. Vidali, *Astrophysical Journal* **522**, 305 (1999).
- 22 Y. H. Kim, J. Ree, and H. K. Shin, *Chemical Physics Letters* **314**, 1 (1999).
- 23 A. J. H. M. Meijer, A. J. Farebrother, D. C. Clary, and A. J. Fisher, *Journal of Physical Chemistry A* **105**, 2173 (2001).
- 24 A. Meijer, A. J. Fisher, and D. C. Clary, *Journal of Physical Chemistry A* **107**, 10862 (2003).
- 25 S. Morisset, F. Aguilon, M. Sizun, and V. Sidis, *Chemical Physics Letters* **378**, 615 (2003).
- 26 S. Morisset, F. Aguilon, M. Sizun, and V. Sidis, *Physical Chemistry Chemical Physics* **5**, 506 (2003).

Chapter 1. Introduction

- 27 S. Morisset, F. Aguillon, M. Sizun, and V. Sidis, *Journal of Physical Chemistry A*
28 **108**, 8571 (2004).
- 28 S. Morisset, F. Aguillon, M. Sizun, and V. Sidis, *Journal of Chemical Physics*
29 **121**, 6493 (2004).
- 29 S. Morisset, F. Aguillon, M. Sizun, and V. Sidis, *Journal of Chemical Physics*
30 **122**, art. no. (2005).
- 30 D. A. Williams and E. Herbst, *Surface Science* **500**, 823 (2002).
- 31 M. P. Collings, J. W. Dever, H. J. Fraser, and M. R. S. McCoustra, *Astrophysics*
32 *and Space Science* **285**, 633 (2003).
- 32 a. W. D. A. Millar T.J., *Dust and Chemistry in Astronomy*. (Institute of Physics,
33 1993).
- 33 J. S. Mathis, W. Rumpl, and K. H. Nordsieck, *Astrophysical Journal* **217**, 425
34 (1977).
- 34 S. Cazaux and A. Tielens, *Astrophysical Journal* **604**, 222 (2004).
- 35 A. Meijer, A. J. Farebrother, and D. C. Clary, *Journal of Physical Chemistry A*
36 **106**, 8996 (2002).
- 36 B. Jackson and D. Lemoine, *Journal of Chemical Physics* **114**, 474 (2001).
- 37 L. Jeloica and V. Sidis, *Chemical Physics Letters* **300**, 157 (1999).
- 38 V. Pirronello, C. Liu, J. E. Roser, and G. Vidali, *Astronomy and Astrophysics*
39 **344**, 681 (1999).
- 39 P. Parneix and P. Brechignac, *Astronomy and Astrophysics* **334**, 363 (1998).
- 40 X. W. Sha, B. Jackson, and D. Lemoine, *Journal of Chemical Physics* **116**, 7158
41 (2002).
- 41 J. Kerwin and B. Jackson, *Journal of Chemical Physics* **128** (2008).
- 42 D. Bachellerie, M. Sizun, F. Aguillon, D. Teillet-Billy, N. Rougeau, and V. Sidis,
43 *Physical Chemistry Chemical Physics* **11**, 2715 (2009).
- 43 D. Bachellerie, M. Sizun, F. Aguillon, and V. Sidis, *Journal of Physical*
44 *Chemistry A* **113**, 108 (2009).
- 44 V. Pirronello, O. Biham, C. Liu, L. O. Shen, and G. Vidali, *Astrophysical Journal*
45 **483**, L131 (1997).
- 45 V. Pirronello, C. Liu, L. Y. Shen, and G. Vidali, *Astrophysical Journal* **475**, L69
46 (1997).
- 46 D. J. Hollenbach, M. W. Werner, and E. E. Salpeter, *Astrophysical Journal* **163**,
47 165 (1971).
- 47 H. B. Perets, A. Lederhendler, O. Biham, G. Vidali, L. Li, S. Swords, E. Congiu,
48 J. Roser, G. Manico, J. R. Brucato, and V. Pirronello, *Astrophysical Journal* **661**,
49 L163 (2007).
- 48 J. E. Roser, G. Manico, V. Pirronello, and G. Vidali, *Astrophysical Journal* **581**,
50 276 (2002).
- 49 J. E. Roser, S. Swords, G. Vidali, G. Manico, and V. Pirronello, *Astrophysical*
51 *Journal* **596**, L55 (2003).
- 50 H. B. Perets, O. Biham, G. Manico, V. Pirronello, J. Roser, S. Swords, and G.
52 Vidali, *Astrophysical Journal* **627**, 850 (2005).
- 51 T. Zecho, A. Guttler, X. W. Sha, B. Jackson, and J. Kupperts, *Journal of Chemical*
52 *Physics* **117**, 8486 (2002).
- T. Zecho, A. Guttler, and J. Kupperts, *Chemical Physics Letters* **370**, 366 (2003).

Chapter 1. Introduction

- 53 A. Guttler, T. Zecho, and J. Kupperts, *Chemical Physics Letters* **395**, 171 (2004).
54 A. Guttler, T. Zecho, and J. Kupperts, *Surface Science* **570**, 218 (2004).
55 T. Zecho, A. Guttler, and J. Kupperts, *Carbon* **42**, 609 (2004).
56 A. Andree, M. Le Lay, T. Zecho, and J. Kupper, *Chemical Physics Letters* **425**,
99 (2006).
57 L. Hornekaer, W. Xu, R. Otero, E. Laegsgaard, and F. Besenbacher, *Chemical*
Physics Letters **446**, 237 (2007).
58 L. Amiaud, F. Dulieu, J. H. Fillion, A. Momeni, and J. L. Lemaire, *Journal of*
Chemical Physics **127** (2007).
59 L. Amiaud, A. Momeni, F. Dulieu, J. H. Fillion, E. Matar, and J. L. Lemaire,
Physical Review Letters **100** (2008).
60 E. Matar, E. Congiu, F. Dulieu, A. Momeni, and J. L. Lemaire, *Astronomy &*
Astrophysics **492**, L17 (2008).
61 J. S. A. Perry, J. M. Gingell, K. A. Newson, J. To, N. Watanabe, and S. D. Price,
Measurement Science & Technology **13**, 1414 (2002).
62 J. S. A. Perry and S. D. Price, *Astrophysics and Space Science* **285**, 769 (2003).
63 S. C. Creighan, J. S. A. Perry, and S. D. Price, *Journal Of Chemical Physics* **124**
(2006).
64 T. R. Govers, L. Mattera, and G. Scoles, *Journal of Chemical Physics* **72**, 5446
(1980).
65 T. R. Govers, <http://hal.ccsd.cnrs.fr/ccsd-00004273/en/> (2005).
66 B. J. McCall, K. H. Hinkle, T. R. Geballe, G. H. Moriarty-Schieven, N. J. Evans,
K. Kawaguchi, S. Takano, V. V. Smith, and T. Oka, *Astrophysical Journal* **567**,
391 (2002).
67 P. A. Gerakines, W. A. Schutte, and P. Ehrenfreund, *Astronomy and Astrophysics*
312, 289 (1996).
68 H. E. Matthews, J. M. Macleod, N. W. Broten, S. C. Madden, and P. Friberg,
Astrophysical Journal **315**, 646 (1987).
69 T. J. Millar, *Monthly Notices of the Royal Astronomical Society* **199**, 309 (1982).
70 G. F. Mitchell, J. L. Ginsburg, and P. J. Kuntz, *Astrophysical Journal Supplement*
Series **38**, 39 (1978).
71 G. D. Watt and S. B. Charnley, *Monthly Notices of the Royal Astronomical*
Society **213**, 157 (1985).
72 R. F. Ferrante, M. H. Moore, M. M. Spiliotis, and R. L. Hudson, *Astrophysical*
Journal **684**, 1210 (2008).
73 L. W. Kamp and F. W. Taylor, *Icarus* **86**, 510 (1990).
74 H. A. Weaver, Leiden, Netherlands, 1996 (unpublished).
75 M. J. Mumma, M. A. DiSanti, N. Dello Russo, K. Magee-Sauer, E. Gibb, and R.
Novak, Houston, Texas, 2002 (unpublished).
76 J. Roithova and D. Schroder, *Journal of the American Chemical Society* **128**,
4208 (2006).
77 E. L. O. Bakes, A. Tielens, C. W. Bauschlicher, D. M. Hudgins, and L. J.
Allamandola, *Astrophysical Journal* **560**, 261 (2001).
78 T. J. Millar, *Monthly Notices of the Royal Astronomical Society* **259**, P35 (1992).
79 R. K. Milburn, A. C. Hopkinson, J. Sun, and D. K. Bohme, *Journal of Physical*
Chemistry A **103**, 7528 (1999).

Chapter 1. Introduction

- 80 C. Simon, J. Liliensten, O. Dutuit, R. Thissen, O. Witasse, C. Alcaraz, and H.
Soldi-Lose, *Annales Geophysicae* **23**, 781 (2005).
- 81 O. Witasse, O. Dutuit, J. Liliensten, R. Thissen, J. Zabka, C. Alcaraz, P. L. Blelly,
S. W. Bougher, S. Engel, L. H. Andersen, and K. Seiersen, *Geophysical Research
Letters* **29** (2002).
- 82 J. Liliensten, O. Witasse, C. Simon, H. Solidi-Lose, O. Dutuit, R. Thissen, and C.
Alcaraz, *Geophysical Research Letters* **32** (2005).
- 83 M. R. Bruce, L. Mi, C. R. Sporleder, and R. A. Bonham, *Journal of Physics B-
Atomic Molecular and Optical Physics* **27**, 5773 (1994).
- 84 P. Calandra, C. S. S. O'Connor, and S. D. Price, *Journal of Chemical Physics* **112**,
10821 (2000).
- 85 C. Szymtkowski, A. Domaracka, P. Mozejko, E. Ptasinska-Denga, L. Klosowski,
M. Piotrowicz, and G. Kasperski, *Physical Review A* **70** (2004).
- 86 N. A. Love and S. D. Price, *Physical Chemistry Chemical Physics* **6**, 4558 (2004).
- 87 N. A. Love and S. D. Price, *International Journal of Mass Spectrometry* **233**, 145
(2004).
- 88 S. J. King and S. D. Price, *Journal of Chemical Physics* **127** (2007).
- 89 M. R. Bruce and R. A. Bonham, *International Journal of Mass Spectrometry and
Ion Processes* **123**, 97 (1993).
- 90 S. D. Price, *Journal of the Chemical Society-Faraday Transactions* **93**, 2451
(1997).
- 91 S. D. Price, *International Journal of Mass Spectrometry* **260**, 1 (2007).
- 92 D. Schroder and H. Schwarz, *Journal of Physical Chemistry A* **103**, 7385 (1999).
- 93 S. D. Price, *Physical Chemistry Chemical Physics* **5**, 1717 (2003).
- 94 J. Senekowitsch and S. Oneil, *Journal of Chemical Physics* **95**, 1847 (1991).
- 95 C. S. O'Connor and S. D. Price, *International Journal of Mass Spectrometry* **184**,
11 (1999).
- 96 F. M. Harris, *International Journal of Mass Spectrometry and Ion Processes* **120**, 1
(1992).
- 97 M. Lundqvist, P. Baltzer, D. Edvardsson, L. Karlsson, and B. Wannberg, *Physical
Review Letters* **75**, 1058 (1995).

Chapter 2 Experimental

Overview

The experimental apparatus in the UCL Cosmic Dust Laboratory has been designed to probe the internal rotational and vibrational energy distribution of molecular hydrogen formed on an interstellar dust grain analogue; the experiments discussed in this thesis have focussed on the formation of HD. In this experiment single beams of H and D-atoms directly impinge on a surface analogous to cosmic dust. These atoms then recombine on the surface to produce, H₂, D₂ and HD through one of the surface mechanisms described previously, either the Eley-Rideal or Langmuir-Hinshelwood mechanism or a combination of the two.

It is not possible to use an actual interstellar dust grain in these experiments so the analogue chosen is highly orientated pyrolytic graphite (HOPG). The surface is used to simulate the carbonaceous grains that are found in the ISM and also allows our results to be easily compared to theoretical studies. The dimensions of the HOPG surface are 10 mm x 20 mm x 2mm, with a mosaic spread of $3.5^\circ \pm 1.5^\circ$. The mosaic spread refers to how ordered the atomic layers are with respect to each other, a more ordered sample has a lower mosaic spread. The layered structure also means it is easier to cleave, giving a fresh surface for new experiments.

The experiment uses the laser technique of Resonance Enhanced Multiphoton Ionisation (REMPI) to ionise the nascent HD molecules from a particular (v, J) ro-vibrational quantum state.¹ This laser technique will be described in detail in a later chapter. The ions formed are then detected using a time-of-flight mass spectrometer (TOFMS), which is discussed in detail later in this chapter. In order to mimic the ISM the experiments are carried out under ultrahigh vacuum (UHV) with low grain surface temperatures of 10-15 K, achieved using cryogenic cooling methods. This chapter will describe the various parts of the experimental set-up.

2.1 Vacuum Set-up

The experimental set-up that is currently in use is an adaptation of the apparatus described by Perry *et al.*² The vacuum system is comprised of two UHV stainless steel chambers that are sealed with conflat flanges, see Figure 1. The first chamber is the ‘source chamber’ as this is where the H and D-atoms sources are housed; the second chamber houses the HOPG target and is hence known as the ‘target chamber’. The base pressure that can be reached in the target chamber is approximately 10^{-10} Torr without the atom sources in use; this is not as low as the pressures found in the ISM which can reach 10^{-13} Torr.³ These experimental conditions are reached by the use of turbomolecular pumps, which have a pumping speed of 400 l s^{-1} backed by two-stage rotary pumps on both chambers. On the target chamber there is also a titanium sublimation pump (TSP), this ensures that the pressure remains as low as possible which is vital to the experiments. The pressure in the source chamber is monitored by a Penning gauge and in the target chamber by an ion gauge.

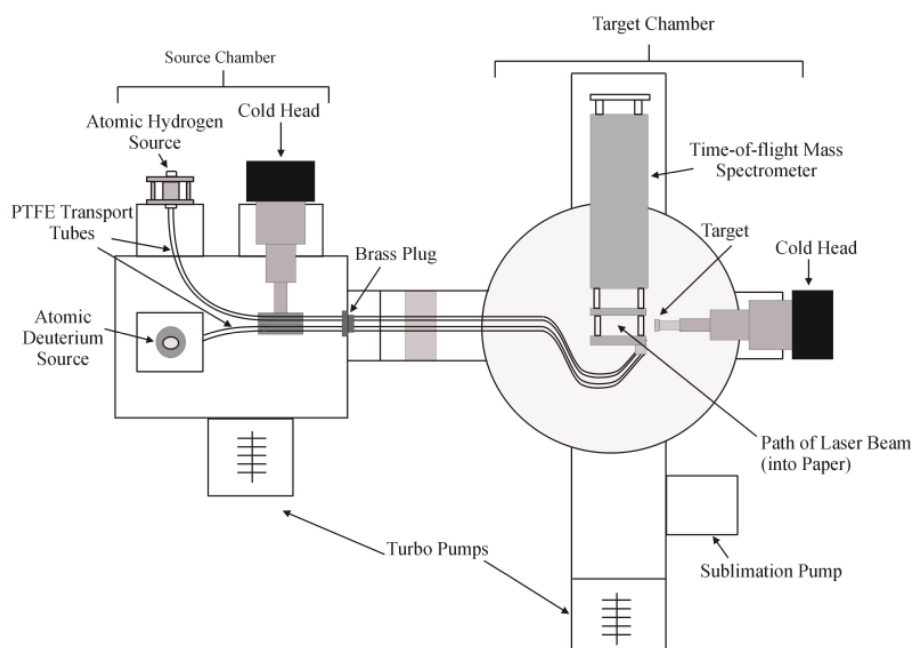


Figure 2.1.1 Schematic diagram of vacuum chamber set-up (not to scale).

2.2 H-atom and D-atom Generation

The hydrogen and deuterium atom beams are both produced in the same fashion, *via* microwave dissociation of high purity H_2 and D_2 gases in separate Pyrex cells. The gases are piped into the Pyrex cells (260 mm long, outer diameter 25.5 mm) and the cells are surrounded by cylindrical 2-piece slotted copper radiators, as designed by

Chapter 2. Experimental

McCullough *et al.*^{4,5} The radiators are designed to fit closely around the Pyrex cells; this allows efficient coupling of the microwaves into the gas. The radiators function by establishing a potential difference (electric field) between the walls of the slots when the microwaves are fed into the radiator.

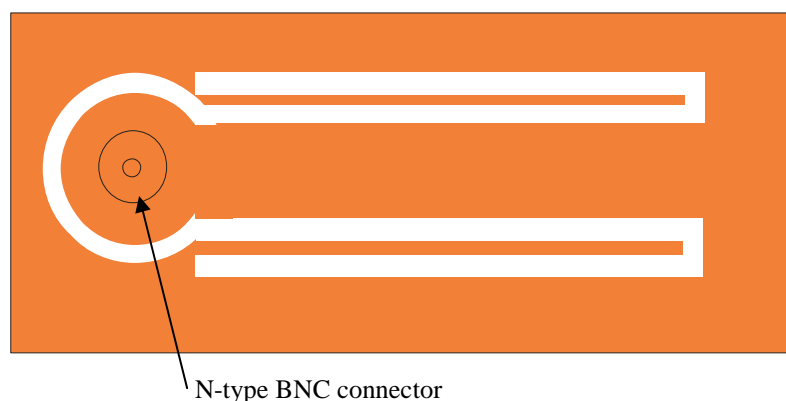


Figure 2.2.1. One half of a microwave radiator showing two sets of slots.

The electrons in this field oscillate back and forth and cause the H_2 and D_2 to dissociate. The radiators are designed so that no tuning of the cavity, where the cell is housed, is required. This is achieved by setting the length of the slots so that the midpoint of the two slots, on each half of the radiator, are half a wavelength apart and the end of each slot is a quarter wavelength from the midpoint of the adjacent slot (see Figure 2.2.1). This configuration results in the creation of a standing wave in the discharge cell that couples the microwave power to the plasma with high efficiency.

The microwaves (2.45 GHz, 180 W) are supplied by a Sairem microwave generator using two Sucoflex waveguides attached to either side of the radiator. Both the H and D-atom sources are supplied with microwaves from the same generator and any gaps around the radiators are sealed with copper tape to prevent any microwave leakage. The radiators have water-cooled copper flanges at each end to keep the atomic discharges cool, since the probability of hydrogen recombination on Pyrex increases with temperature.⁶ The copper flanges are also useful in preventing the cells from overheating due to the microwave radiation. It is necessary to keep the reflected power back to the generator at a level below 10%; this has been achieved by connecting a second external reflected power meter to the microwave generator, from which both sets of sucoflex waveguides are connected to the sources. Two cables are

Chapter 2. Experimental

required for one source; there is a half wavelength difference in the length of one of the cables, this gives rise to more efficient coupling of the microwaves into the plasma.

A schematic of an atom source is shown in Figure 2.2.2. Hydrogen and deuterium gases are piped through separate gas manifold lines into individual Pyrex cells. The tubing in the manifolds is a combination of $\frac{1}{4}$ inch PTFE, copper and glass. A Cajon o-ring seal connects the gas line tubing to the glass-to-metal seal at the top of each cell. Both gas lines can be pumped by a rotary pump.

The H and D atoms leave their respective cells through a 1 mm diameter capillary, 4 cm long, at the base of the cells and are then piped through PTFE tubing up to the target, after being differentially pumped, which will be described in detail later. PTFE has been chosen due to its low recombination efficiency for hydrogen;⁶ PTFE is also safe to use under UHV conditions. Before the cells are installed in the experimental set-up they are soaked in concentrated ortho- H_3PO_4 for at least 12 hours and then rinsed in distilled water. This procedure is carried out to passivate the glass surface and minimise the possibility of any recombination of H and D-atoms.⁷

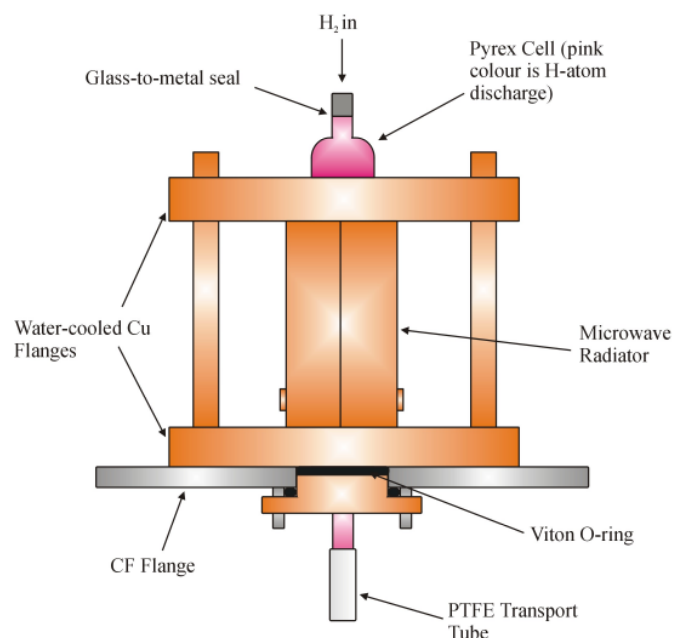


Figure 2.2.2 Schematic diagram of a H or D-atom source.

Chapter 2. Experimental

The sources required ‘conditioning’ over 2-3 days to achieve optimum H or D-atom production. For this reason the sources run continuously, with appropriate safety trips and are only turned off when it is essential. The safety trips fitted to the apparatus are designed to turn off the microwave generator and shut off the flow of the gases to the chamber should any of the following situations arise: the pressure in the source chamber reaches $\geq 6 \times 10^{-5}$ Torr, the pressure in the target chamber reaches $\geq 1 \times 10^{-5}$ Torr, the temperature of the cells is greater than 25 °C or the brightness of the plasma in the cells falls below a given threshold. There are both temperature and light sensors positioned on both the cells to check the temperature and brightness. The output from these detectors is fed into an interlock unit, this unit uses relays to control the mains output to the microwave generator and also to the solenoid valves fitted to the gas lines. If the conditions fall below the optimum the microwave generator and the gas lines will be shut off. It is possible to bypass the trip system if necessary. Figure 2.23 below shows a basic circuit diagram for one set of the safety trips.

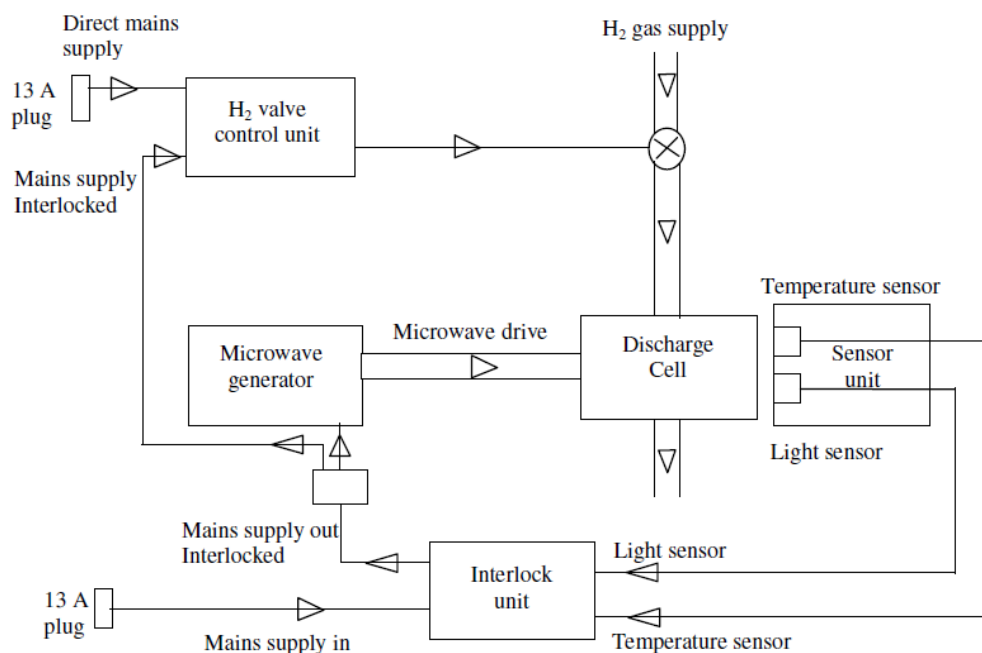


Figure 2.2.3 Basic circuit diagram of the safety trips for the H and D atom sources.

2.3 Atom Beam Transport

When the H and D atoms leave the microwave dissociation cells they pass through a narrow capillary and are then piped separately through PTFE tubing directly onto the

HOPG target. The PTFE tubing leading from the capillary at the base of each cell has a 6 mm outer diameter and is connected to a PTFE block of 5 mm inner diameter by means of a PTFE plug. This plug has two ‘pumping’ holes of diameter 2 mm drilled through it, which allows a large amount of the gas beam to escape into the source chamber. This arrangement ensures that the pressure in the target chamber stays low while allowing the discharge cells to be kept at optimum pressure (0.5 Torr) for maximum dissociation.

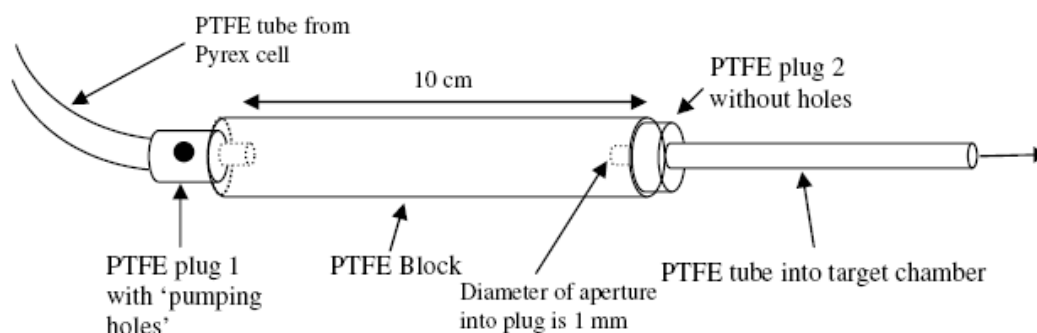


Figure 2.3.1 Schematic diagram to show how the H and D-atoms are piped through the PTFE tubes and blocks. The pumping holes allow some of the gas to escape into the source chamber so that the pressure in the target chamber stays low, but the dissociation cells can still be kept at an optimum pressure for H and D dissociation.

The PTFE block is then connected to another length of PTFE tubing, of outer diameter 3 mm by a second PTFE plug. This plug does not have any pumping holes in it and the diameter of the exit aperture is 1 mm. The tube then passes through a hole in a brass seal separating the source chamber from the target chamber so that only gas from the tube enters the target chamber. This arrangement results in a pressure of approximately 1×10^{-6} Torr in the source chamber and with both sources on, the pressure in the target chamber is about $\sim 5 \times 10^{-8}$ Torr.

An important part of the experiment is to ensure that the flux of the H and D-atoms is sufficient for any recombination to be observed and also to ensure that the atoms are directed at the surface. This requires a mount in which to place the PTFE transport tubes so the atoms exiting the tube directly impinge on the HOPG surface. The mount was designed so that both the H and D-atom tube could be held in place and attached to the repeller plate of the time-of-flight mass spectrometer (see Figure 2.3.2). This

meant that both the tubes could be directed towards the target at the same angle and at the same distance from the surface. The mount is made of aluminium and has two holes, one for each PTFE tube and directs the atom beams onto the target surface; there is a gap of approximately 2 mm between the end of the tubes and the HOPG surface. Checks are carried out to ensure that the PTFE tubes come all the way through the holes in the mount so that neither the H nor D-atoms could interact with the aluminium. This tube mount was redesigned to allow for the H and D-atoms to be cooled to approximately 50 K. The details of the new design are discussed later in this thesis.

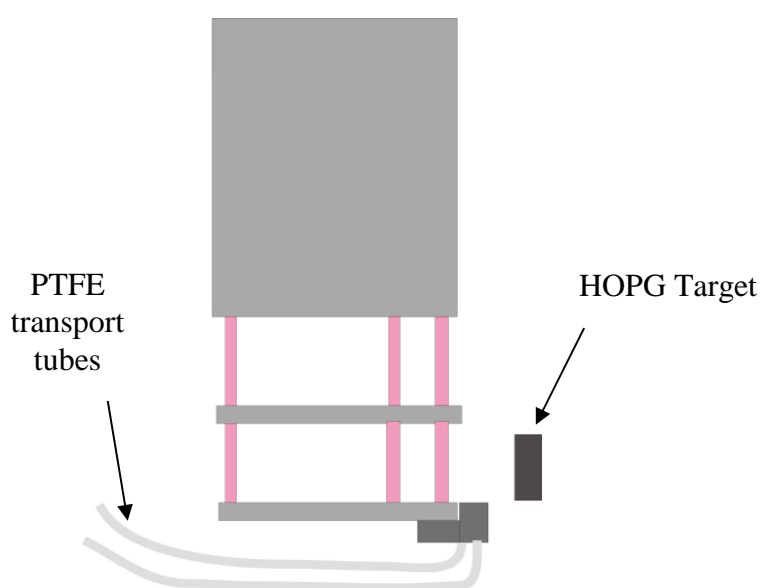


Figure 2.3.2 Schematic diagram to show how the H and D-atom transport tubes are mounted on the repeller plate of the time-of-flight mass spectrometer.

2.4 Target Mount and Coldhead

This experiment requires that the HOPG target is mounted in such a way that it can be cooled to temperatures of approximately 10 – 20 K to model the interstellar medium,⁸ but also heated to around 500 K^{9,10} to clean the surface. The target has to be positioned in the chamber close enough to the laser interaction region and mass spectrometer so that the nascent HD molecules are detectable as soon as they leave the surface and cannot interact with the walls of the chamber first. The laser interaction region is approximately 2 cm from the HOPG surface therefore; only newly formed molecules will be ionised and detected once they have been desorbed from the surface. Any molecules that do not enter the laser interaction region will be

Chapter 2. Experimental

lost: this is the case because when the H and D atom source are switched off there is no REMPI signal, indicating there is no residual HD left in the chamber.

The target is cooled cryogenically by a closed cycle helium compressor which drives a two-stage 12 W coldhead. This coldhead can reach temperatures of 9 K from room temperature in 45 minutes and has a maximum working temperature of 330 K. The temperature of the coldhead is monitored using a silicon thermodiode which is attached to the base of the coldhead, below the copper rod, which is described later.

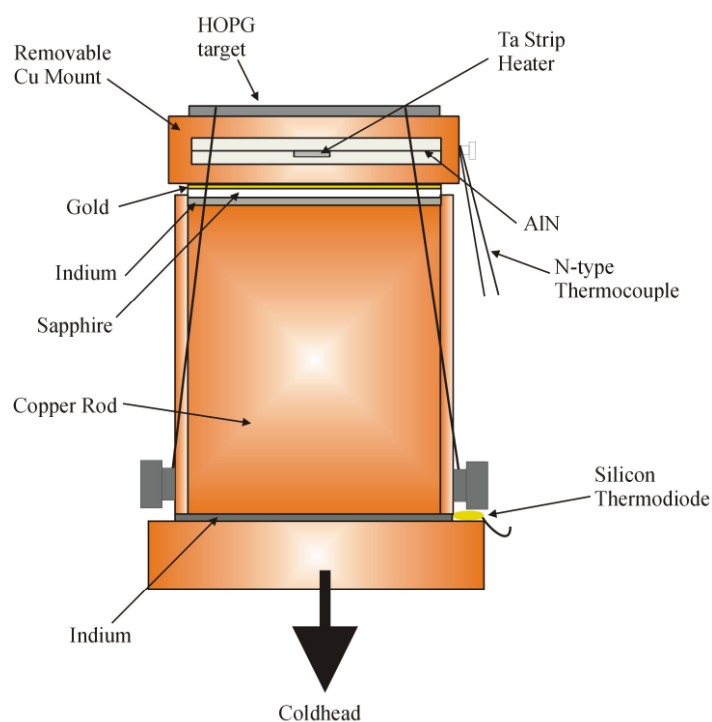


Figure 2.4.1 Schematic diagram of target mount set-up.

The design of the target mount is such that the target is attached to a removable copper mount on the end of a copper rod which is fixed to the coldhead. The removable copper mount surrounds two pieces of AlN, between which a tantalum strip is held. This strip allows resistive heating of the surface to remove any unwanted adsorbates before starting the experiments. As mentioned previously the heater allows the HOPG surface to reach in excess of 500 K. However, temperatures above 330 K would damage the coldhead, which presents a problem, see Figure 2.4.1.

Chapter 2. Experimental

This problem is solved by using a piece of 1 mm thick sapphire, placed between the removable copper mount and the copper rod. Below 50 K the sapphire is a very efficient thermal conductor, but when heated above 200 K it is a poor thermal conductor.¹¹ Hence, when the target is being heated, while the coldhead is on, there is minimal heat flow back into the coldhead which prevents it from being damaged. A strip of indium is placed between the sapphire and the copper rod and a length of gold is between the sapphire and the removable copper mount. Both these metals are used to improve the thermal contact between various sections of the mount and the coldhead to ensure that the target temperature is as close as possible to that of the coldhead.

The target is secured to the top of the mount using Ni tensioning wires which are held tight with a set of 'sprung' washers and nuts (see Figure 2.42). The 'sprung' washers keep the wires tight should anything loosen on the mount, for example when it is heated. An n-type thermocouple (Nickel-Chromium-Silicon) is attached to the side of the copper mount, very close to the target, to monitor the temperature of the target. A second n-type thermocouple is attached to various places on the mount in order to monitor the temperature of different regions. Finally an aluminium radiation shield is attached to the end of the coldhead and surrounds the target mount set-up, this prevents any radiative heating of the target from the chamber and helps to keep the temperature as close to 10 K as possible.

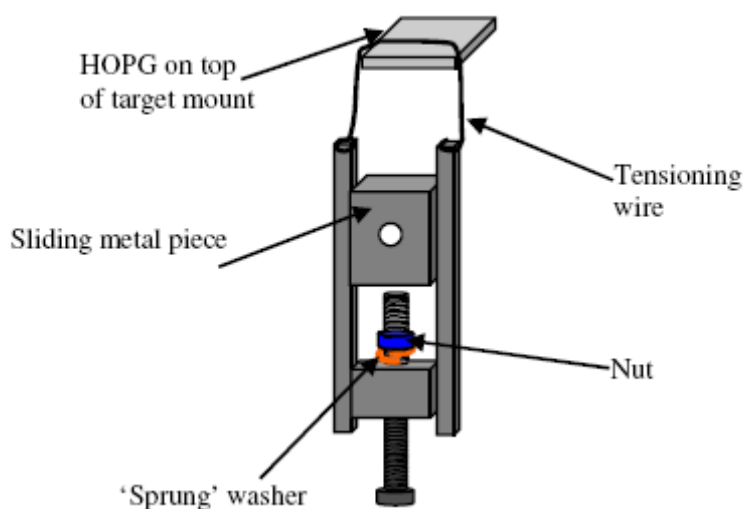


Figure 2.4.2 Diagram showing the metal clamp and tensioning wire system that holds the HOPG surface in place. One clamp is used on either side of the target for security.

2.5 Time of Flight Mass Spectrometry

As discussed previously any new molecules which are formed on the HOPG surface can enter the laser interaction region and be ionised. Once the nascent molecules have been ionised the HD^+ ions are detected using time-of-flight mass spectrometry (TOFMS). The technique is particularly effective for detecting ions from pulsed sources such as the pulsed laser used in this experiment. Time-of-flight mass spectrometers do not require accurate magnetic fields, are compact in size and do not have any complex moving parts. The TOFMS used in this experiment is a conventional spectrometer, based on the design of Wiley and McLaren.¹²

The TOFMS uses a series of electric fields to accelerate ions into an area of uniform potential called the drift tube. Given that mass, kinetic energy and velocity are related, ions of different masses will arrive at the end of the drift tube at different times. Hence, by measuring the time of flight of an ion through the drift tube, its mass can be determined.¹² It can be shown (Appendix A) that the time of flight and the mass of an ion are related by:

$$t = k\sqrt{m} + C \quad 2.5.1$$

Where k is a constant related to the magnitude of the electric fields and the physical dimensions of the spectrometer and C is a constant from the electronic timing system. The spectrometer in this experiment is comprised of a repeller plate of 50 mm diameter and a middle plate also 50 mm in diameter, mounted 30 mm above the repeller plate, and a drift tube, see Figure 2.51. The middle plate has a grid of fine Ni mesh fitted across it to ensure the electric field applied remains uniform. The grid allows 98% transmission of the ions. The drift tube is mounted 30 mm above the middle plate and is 360 mm long, this also has a grid at either end to maintain a uniform electric potential throughout its length.

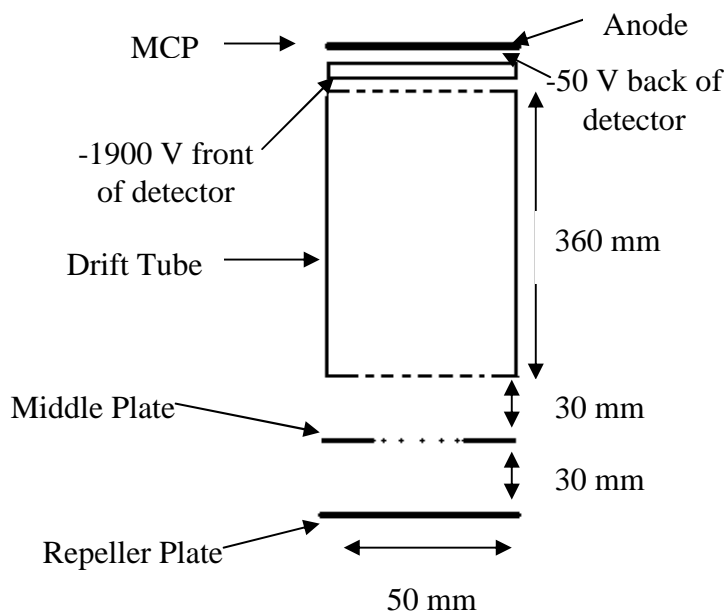


Figure 2.5.1 Schematic diagram of physical arrangement of the TOFMS.

Above the exit of the drift tube is mounted a pair of Micro Channel Plates (MCPs). The plates are made up of an array of $10\ \mu\text{m}$ wide glass channels; these channels are coated in a compound with a very low work function. When ions hit the MCP they collide with the walls of the channels and release electrons. These electrons release further electrons through collisions with the channel walls until a cascade of electrons leaves the surface of the MCP. In general, approximately 10^4 electrons are released per ion, hence from two plates the number of electrons given out is 10^8 . A small negative potential of $-50\ \text{V}$ repels the electrons away from the MCP until they hit a copper anode, mounted $5\ \text{mm}$ above the MCP and are detected.

To be able to record a mass spectrum with the TOFMS, a series of amplification and counting electronics are required. The laser sends a 'start' signal to a multi-stop time-to-digital converter (TDC) which initiates a 'look window' in which to look for ion events. After about $9\ \mu\text{s}$ the pulse generator sends a 'reset' signal to the TDC which stops it recording ions for that laser pulse. During the look window the TDC will receive ion signals from the TOFMS. However, prior to reaching the TDC the ion signal passes through a fast pre-amplifier. The signal then goes via an impedance matching circuit to an amplifier and a constant fraction discriminator (CFD) to give pulse suitable for the TDC. Finally the counts from the TDC are sent via a

CAMAC/GPIB interface to a PC where they are displayed. Figure 2.5.2 below shows diagram of the timing electronics.

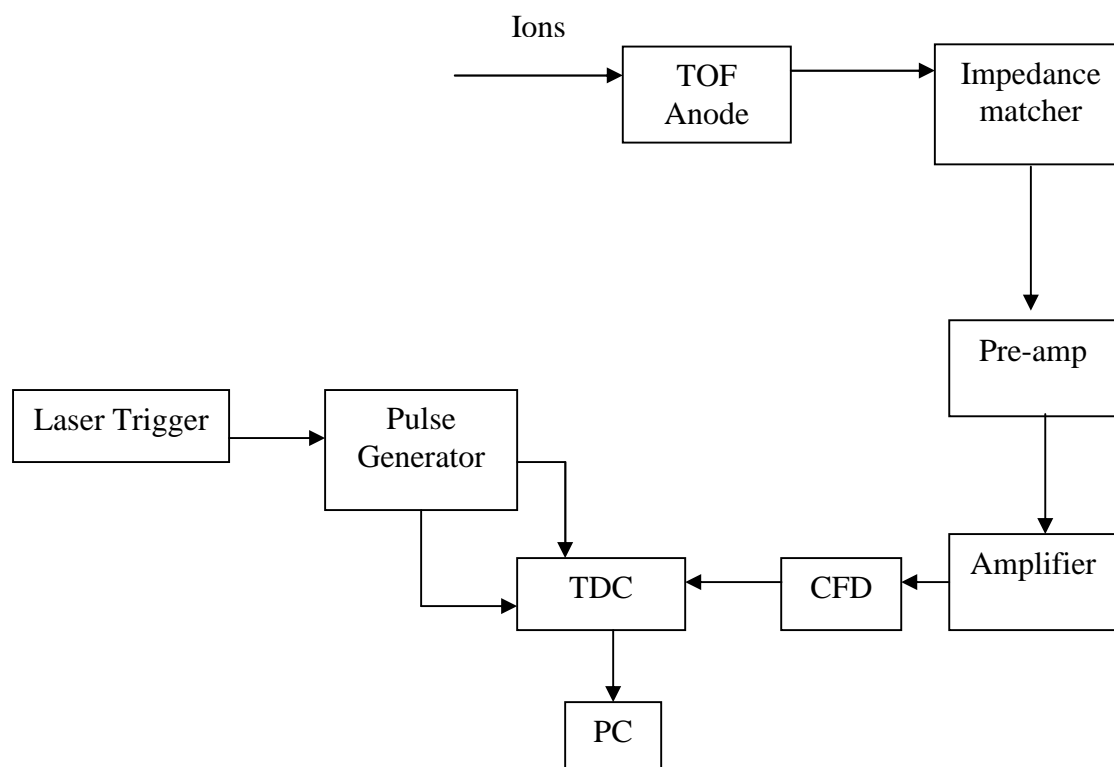


Figure 2.5.2 Block diagram to show the timing electronics for the TOFMS.

2.6 Focussing Conditions for the TOFMS

Two different focussing conditions affect the resolution of the TOFMS: they are space-focussing and energy-focussing. Space-focussing addresses the issue that not all the ions entering the drift tube will have been ionised at a constant distance, s_0 , away from the drift tube. If an ion is accelerated from a distance less or equal to s_0 then it will be overtaken by an ion that was accelerated from a distance greater than s_0 away from the drift tube. These later ions will be able to overtake ions formed closer to the drift tube because they were formed at a greater distance from the drift tube and hence have been accelerated for longer; therefore, they have a higher corresponding kinetic energy. As a result of this effect, ions of the same mass will have a spread of energies and therefore a spread of flight times, which makes it hard to separate ions of similar mass in practice. Space focussing is not a significant issue in this experiment since the HD molecules are ionised in a highly localised volume by the focused laser beam.

If

$$\left(\frac{dt}{ds}\right)_{s_0} = 0 \quad 2.6.1$$

where t is time, it is possible to find the position at which ions, that were ionised at a distance given by equation 2.6.2, pass ions which started a distance $s = s_0$ from the drift tube. The electric fields outside the drift tube can be manipulated to focus ions of the same mass so that they arrive with a small spread of flight times,¹² see Appendix A for further details.

$$s = s_0 \pm \frac{1}{2} \delta s \quad 2.6.2$$

Energy focusing in a TOFMS is a way of attempting to rectify the problem of ions of the same mass having different initial kinetic energies. Consider two ions of the same mass with the same kinetic energy, moving in opposite directions when the accelerating electric field is applied. The ion moving away from the drift tube will be decelerated by the field until it stops. This ion will then be accelerated back in the direction of the drift tube until it is travelling with the same speed as the ion that was initially travelling towards the drift tube when the field was applied. This will result in a characteristic time lag between the two ions which can be minimised by energy focusing. Energy focusing is generally harder to achieve than space focusing as it requires alterations to the physical dimensions of the spectrometer, in particular the drift tube and the size of the ionisation and acceleration regions and can be at the expense of space focusing.¹² However, energy focusing is not important in this experiment since any spread in energies of the ions can be used to give information on the translational energies of the nascent molecules. For the experiments described in this thesis, the repeller plate is at ground, the middle plate set to -400 V, the drift tube is at -1600 V and the MCP to -1900 V.

2.7 The Laser System and REMPI Technique

2.7.1 Laser System

The laser technique of Resonance Enhanced Multi-Photon Ionisation (REMPI) is employed to probe the ro-vibrational states of HD formed on the HOPG surface. The principles of REMPI and reasons for its choice will be described later. In this section the laser system used to produce the photons required to state selectively ionise the HD will be described. For the REMPI scheme used in these experiments photons of wavelength 200 – 240 nm are required in order to probe the $v'' = 0 - 7$ levels of HD. The laser system used to achieve these wavelengths consists of three parts: Nd:YAG pump laser, tuneable dye laser and a frequency doubling or tripling unit. Each of these parts will be described below.

2.7.2 Nd:YAG Laser

The Nd:YAG laser is a solid state laser that consists of a core rod of Yttrium Aluminium Garnet (YAG) $Y_3Al_5O_{12}$. Present in the YAG lattice are impurities of Nd^{3+} which are randomly distributed in the lattice, on sites that are usually occupied by yttrium ions. The Nd^{3+} ions provide the energy levels required for laser transitions. Although the YAG rod is not directly involved in the lasing action it plays an essential role in how the laser works. The electrostatic field, known as the ‘crystal field’, from the YAG matrix influences the Nd^{3+} ion impurities in the lattice. In the gas phase, Nd^{3+} ions have many degenerate energy levels. However, in the YAG rod these energy levels are perturbed, partly lifting their degeneracy. The YAG crystal field also affects the transitions probabilities between the energy levels in the Nd^{3+} so that previously forbidden transitions become available.

The complete result of the aforementioned affects is that the ground and first excited electronic states of the Nd^{3+} ions are split into groups of levels as shown in Figure 2.7.1.

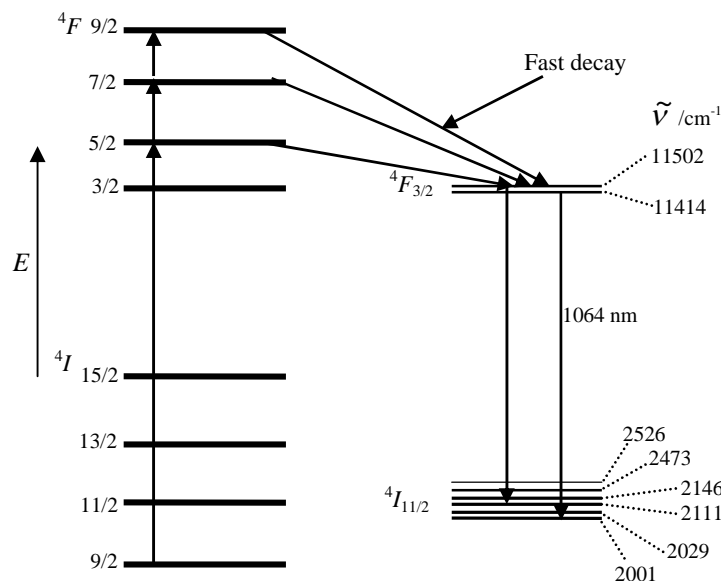


Figure 2.7.1 Energy level diagram for the transitions in the Nd:YAG laser, $\tilde{\nu}$ refers to the energy of that particular level.

These Nd levels are pumped by an intense pulse of light from two xenon flash lamps. This flash excites the Nd^{3+} ions from the ground state, $^4I_{9/2}$ to 4F levels. The number of 4F_J levels result in a large number of available pumping transitions, which in turn increases the efficiency of the laser. The upper levels undergo rapid non-radiative decay to the $^4F_{3/2}$ state, from which the laser emission occurs.¹³ The most intense transition arises at 1064 nm and is a superposition of the two transitions shown in Figure 2.7.1.

The 1064 nm light can be either frequency doubled to 532 nm by a potassium dihydrogen phosphate (KD*P KD_2PO_4) crystal or frequency tripled to 355 nm by a β -Barium Borate (BBO $\beta\text{-BaB}_2\text{O}_4$) crystal. The choice of crystal depends on the rovibrational state that is being probed, for $\nu'' = 0$ and 1, 532 nm is required and for $\nu'' = 2 - 7$, light of 355 nm is used. The power of the laser pulse can be increased by an electro-optic Q-switch, which is provided by a Pockels cell, in the cavity, before the KD*P or BBO crystal. Q-switching is a technique designed to obtain short, intense pulses of radiation from a laser. It involves introducing time-dependent losses into the laser cavity, therefore lowering the Q-factor of the cavity. With high losses in the cavity, the population inversion can reach significant values without laser action

occurring, since the poor Q-factor prevents laser action while energy is being pumped into the excited state of the Nd^{3+} . When a large population inversion has been achieved, the Q-factor is suddenly improved and the laser oscillations can begin, resulting in a short and powerful pulse. If Q-switching is to be efficient the rate of pumping must be faster than the spontaneous decay rate of the upper lasing level to prevent it depopulating faster than it can be filled. This would prevent a large population inversion from occurring. The Q-switch should switch rapidly compared with the build up of laser oscillations; if it does not then the laser oscillations will only build up gradually, leading to a longer pulse with lower peak power.^{13,14} The YAG laser pulses at 10 Hz with pulse of 4 – 6 ns in length. The 532 nm second harmonic has energies of approximately 400 mJ per pulse whereas the 355 nm third harmonic has energies of approximately 300 mJ per pulse. Either the second or third harmonic is used to pump the dye laser, described in the next section.

2.7.3 Tuneable Dye Laser

To be able to ionise HD from a range of ro-vibrational states, a variable-wavelength light source must be used. In this experiment the light source used is a dye laser which is pumped by either 532 nm or 355 nm light from the Nd:YAG laser. The main advantage of the dye laser is that it can be tuned over a significant wavelength range, and therefore, can be scanned over a variety of wavelengths in order to find a signal for a given ro-vibrational state.^{13,14}

The main component of the dye laser is an organic dye dissolved in a solvent such as methanol. When the dye is excited it fluoresces, at longer wavelength than the excitation source and over a broad wavelength range. The fluorescence occurs between the low lying levels in the S_1 electronic state and the ro-vibrational levels in S_0 , as shown in Figure 2.7.2. Pumping with the Nd:YAG laser results in excitation from the ground S_0 state to the first excited electronic state, S_1 . It is also possible to populate the S_2 electronic state, as shown in Figure 2.7.2. Rapid non-radiative decay by collisional relaxation to the lower ro-vibrational levels in S_1 then occurs. This results in a population inversion between these levels and the S_0 state. The laser transition is the fluorescence that occurs as the low lying S_1 states decay to the ro-vibrational states in S_0 . There are many close packed ro-vibrational levels in both

singlet states, so the possibility of many transitions is high which results in an emission spectrum which is very broad.^{13,14}

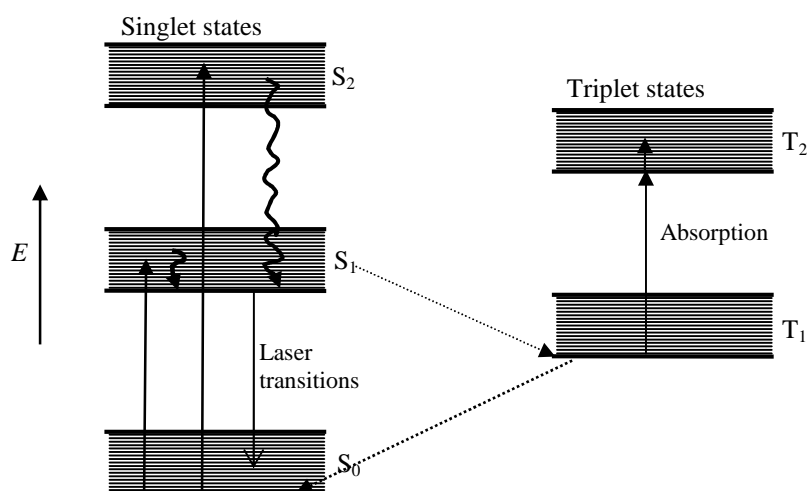


Figure 2.7.2 Schematic of the energy levels and laser transitions in a dye laser.

Shown in Figure 2.7.2 are the triplet states T_1 and T_2 , although these states are not directly involved in the laser action, they can affect it. There is a distinct probability of a non-radiative $S_1 \rightarrow T_1$ transition. This transition may lead to a reduction in the gain of the laser as the T_1 to T_2 transition is pumped by the same range of frequencies of light as the laser transition. The solution to this problem is to operate the pumping in short pulses of approximately $1 \mu\text{s}$, which is shorter than the time it takes to build up any population in T_1 . If the time between the pulses is long enough to allow the $T_1 \rightarrow S_0$ transition to occur, hence emptying the T_1 level before they can be pumped to T_2 and reduce the laser gain.

The laser dyes that are chosen for this experiment depend on the wavelength required to ionise the nascent HD molecules in a specific internal energy state. Table 1 below lists the laser dyes used to ionise HD in the vibrational states $v'' = 0 - 7$. All the dyes are dissolved in methanol.

| ν'' | Laser Dye | Wavelength/nm | Dye Tripled or Doubled? | YAG Tripled or Doubled? |
|---------|--------------|---------------|-------------------------|-------------------------|
| 0 – 1 | DCM | 201 – 211 | Tripled | Doubled |
| 2 – 3 | Coumarin 440 | 216 – 221 | Doubled | Tripled |
| 4 | Coumarin 450 | 227 – 228 | Doubled | Tripled |
| 5 - 7 | Coumarin 480 | 235 - 241 | Doubled | Tripled |

Table 1. Shows the details of the dye and YAG laser set-up for the vibrational states of HD probed.

There are three different stages to the dye laser: the oscillator, the pre-amplifier and the amplifier (Figure 2.7.3). The oscillator and the preamplifier are contained in the same dye cell but the pumping light enters at two different heights. When the pulsed light beam leaves the YAG it is reflected by two appropriately coated mirrors into the dye laser. The pumping light is split and some is sent to the oscillator, this causes the dye to fluoresce. It is important that this fluorescence is in the correct place in the dye cell to be amplified in the laser cavity. In addition, the dye cell must also be correctly located in the laser cavity so that the path of the cavity passes through the dye solution. The light in the oscillator cavity travels between the output coupler and the tuning mirror *via* a grating, which can be moved to alter the wavelength of the light that is amplified by the cavity. To increase the intensity of the dye laser beam emerging from the laser cavity the dye laser radiation passes again through the same dye cell in a more elevated position, where the dye is pumped again by a portion of the pumping beam from the YAG. As before, the position of the pump and dye laser beam must be adjusted so there is good overlap.

After pre-amplification there is one final stage of amplification which takes place in a separate capillary cell pumped by 70% of the beam from the YAG. When making adjustments to the capillary cell it is important to check the position of the dye laser beam through the cell as this will affect the beam shape. If the light passes through the cell too close to the capillary wall, the dye laser beam becomes too intense on one side and can burn the edge of the cell. The shape of the beam can be altered by moving the capillary cell up or down and in or out. A good dye beam shape allows the doubling or tripling crystals to work efficiently. With good beam shape and new dye one could expect to achieve powers of between 3 – 4 mJ in the oscillator and

approximately 15 – 18 mJ in full dye beam. The power from the dye laser will reduce over time as the dyes degrade. The Coumarin dyes degrade faster than DCM so regular dye changes are required to maintain the laser power. The power from the YAG can be reduced by altering the Q-switch setting, reducing the power in the pump beam increases the lifetime of the laser dye.

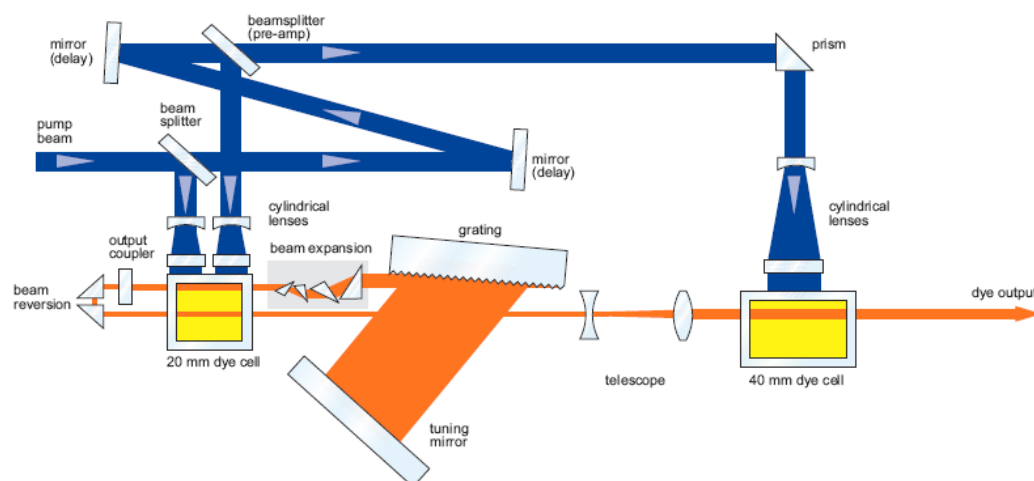


Figure 2.7.3 Schematic diagram of the optical layout of the dye laser.

2.7.4 Frequency Doubling and Frequency Mixing

The REMPI schemes used for ionising the nascent HD molecules requires the photons from the dye laser to be either frequency doubled or tripled to give photons of around 200 – 240 nm.¹⁵ This is achieved by the use of non-linear crystals of KD*P and Barium Borate (BBO) β -BaB₂O₄ to create the second and third harmonics of the dye laser beam. The light can either be frequency doubled using a BBO crystal or frequency doubled using the KD*P crystal; the light can then be frequency mixed with the residual laser dye beam in a different BBO crystal, to result in photons with a third of the wavelength of the original beam of light.

2.7.5 Frequency Doubling

When a beam of light propagates through a solid, electric dipoles are induced in the solid which interact with the oscillating electric field. The induced dipole moment, μ , is given by:

$$\mu = \alpha E \quad 2.7.1$$

Chapter 2. Experimental

where E is the oscillating electric field and α is the polarisability of the medium. This equation is only approximate and if the incident electric field is large enough it can be expressed as a power series:

$$\mu = \alpha E + \frac{1}{2} \beta E^2 + \frac{1}{6} \gamma E^3 + \dots \quad 2.7.2$$

where β is the hyperpolarisability and γ is the second order hyperpolarisability of the medium.

Non-linear effects occur as a result of these higher terms. The relationship between the vibrations in the lattice of the crystal and the irradiance by the beam of laser light becomes non-linear as the amount of light hitting the crystal increases. The magnitude of the incident electric field, E , is given by:

$$E = E_0 \sin(2\pi\nu t) \quad 2.7.3$$

where E_0 is the amplitude of oscillation, ν is the frequency.

Given that:

$$E^2 = E_0^2 (\sin(2\pi\nu t))^2 \quad 2.7.4$$

$$= \frac{1}{2} E_0^2 (1 - \cos(2\pi 2\nu t)) \quad 2.7.5$$

the radiation scattered from the crystal will have twice the original frequency of the incident wave; this is known as second harmonic generation. It is only possible for this to take place in non-centrosymmetric crystals which have a non-linear response to an applied field.^{13,14}

The technique of phase-matching is employed to ensure that the second harmonic light is at maximum power. The optical properties of the crystals used to produce the

doubled light mean that the refractive index of the crystal, and therefore the speed of the light travelling through it, depends on the wavelength.^{13,14} This effect will result in the doubled light travelling through the crystal at a different speed to the fundamental beam. The fundamental beam is continuously generating the frequency-doubled beam on its way through the crystal and hence, the doubled light cannot stay in phase with itself. A large enough phase difference will result in the frequency-doubled beam becoming completely out of phase with itself and destructive interference will take place, dramatically reducing the power of the doubled light.

These problems can be solved using appropriate phase-matching. Phase-matching chooses a path through the crystal where the velocity of the fundamental beam, which corresponds to the O-ray (ordinary ray) of frequency ν and refractive index n_o^ν , is the same as the frequency of the doubled beam, which corresponds to the E-ray (extraordinary ray) of frequency 2ν and refractive index $n_o^{2\nu}(\theta)$, see Figure 2.7.4. Therefore, a path is chosen where $n_o^\nu = n_o^{2\nu}(\theta)$, both beams will remain in phase and the second harmonic irradiance will build up.

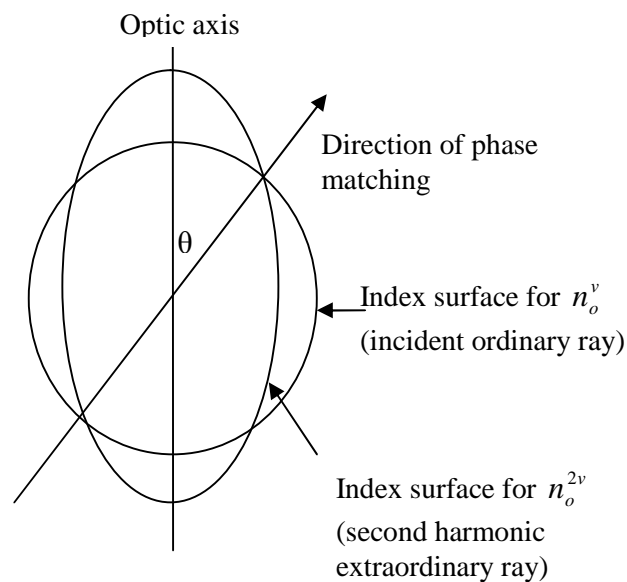


Figure 2.7.4 Wave ellipsoid for incident and second harmonic rays. The circle and ellipse indicate how the phases of the electric fields of the O-ray and E-ray alter as they go through the crystal.^{13,14}

Chapter 2. Experimental

Achieving a build up of the second harmonic irradiance can be a difficult process and a number of factors need to be taken into consideration when attempting to get successful phase matching. The refractive indices of the crystals are temperature dependent, so it is necessary to control the temperature. Here, the BBO doubling crystal is attached to a heater that maintains a constant working temperature of 50 °C. The laser beam divergence must be minimised, as only one direction of propagation through the crystal is perfectly phase matched. This is achieved by creating ‘look-up’ tables for the crystal position as a function of wavelength. Look-up tables are set up for both the doubling and tripling crystals and involve changing the rotation of the crystals in small steps to find the optimum position for the crystal to give maximum conversion at each wavelength. The optimum positions for both the BBO and KD*P crystals are stored in a computer so that the crystal can return to the correct position for a given wavelength, hence maintaining maximum power throughout the scan. The production of the third harmonic is described below.

2.7.6 Frequency Mixing

Once the second harmonic light is generated, the dye beam and the doubled light are mixed in a BBO crystal to give light of the required wavelength to ionise HD via a (2+1) REMPI scheme. The frequency of the light produced by the BBO crystal will be the sum or difference of the frequencies of the two beams entering the crystal. The frequency mixing works in the following way:^{13,14} for two beams of frequency ν_1 and ν_2 with amplitudes E_1 and E_2 , the second order polarisation term from equation 5 becomes:

$$\beta(E_1 \sin \nu_1 t + E_2 \sin \nu_2 t)^2 \quad 2.7.6$$

Expanding this term gives:

$$\beta(E_1^2 \sin^2 \nu_1 t + E_2^2 \sin^2 \nu_2 t + 2E_1 E_2 \sin \nu_1 t \sin \nu_2 t) \quad 2.7.7$$

The third term in this equation can be rewritten as:

$$E_1 E_2 \beta [\cos(\nu_1 - \nu_2)t - \cos(\nu_1 + \nu_2)t] \quad 2.7.8$$

which finally gives us terms that show that light emitted from the crystal with the frequency:

$$\nu_3 = \nu_1 \pm \nu_2 \quad 2.7.9$$

Therefore, we obtain photons with three times the frequency (or a third of the wavelength) of the fundamental dye laser beam.

2.7.8 Frequency Doubling and Frequency Mixing Optics

As discussed in the previous section, light from the dye laser can be either frequency doubled or frequency tripled to generate the required photons for the HD REMPI process. The wavelength of these photons is dependent on the ro-vibrational state of HD that is to be ionised; the wavelength required can vary from 200 nm to 240 nm. For shorter wavelengths the third harmonic is used and to achieve longer wavelengths the second harmonic of the dye laser beam is used. Doubling and tripling requires two different optical set ups: these are shown below in Figures 2.7.5 and 2.7.6.

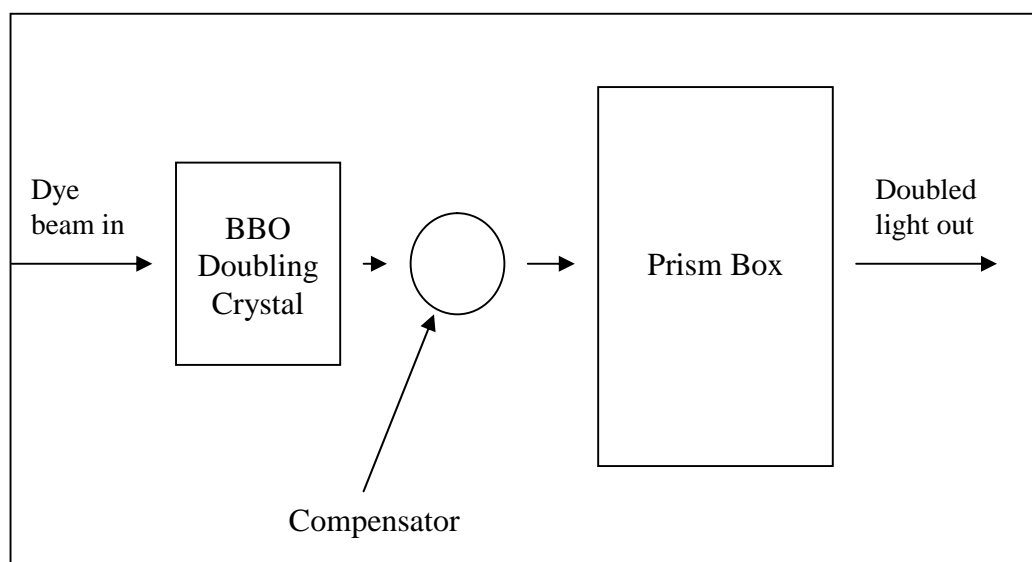


Figure 2.7.5 Schematic diagram showing the set-up of the doubling optics.

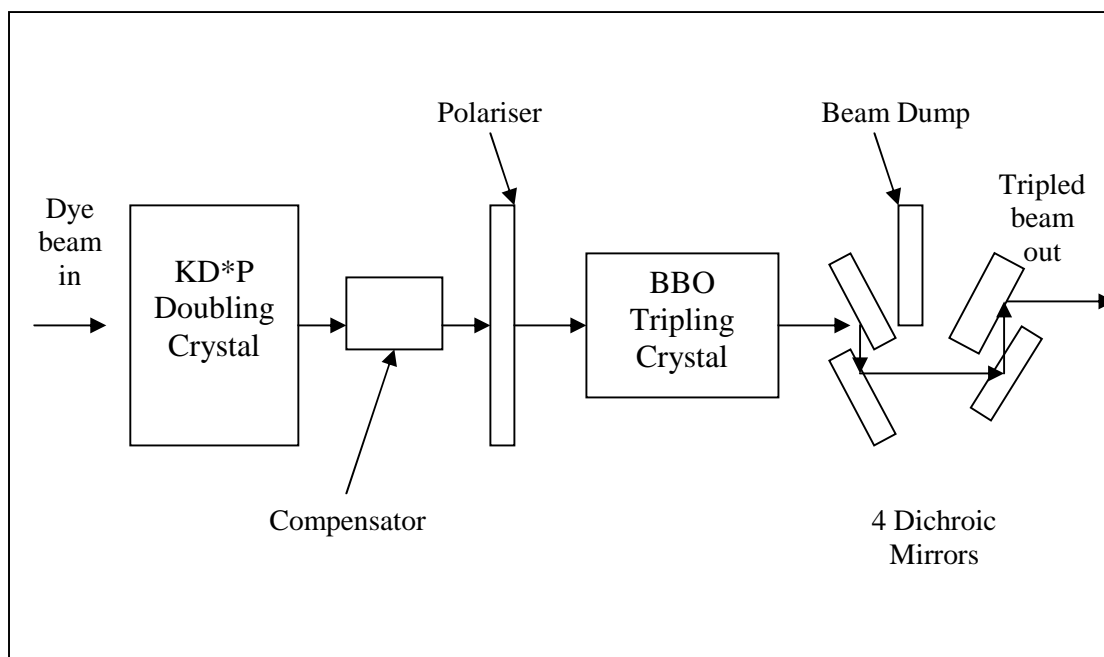


Figure 2.7.6 Schematic diagram showing the set-up of the tripling optics.

In both the doubling and tripling set-ups the dye laser beam enters the doubling crystal, the position of which is controlled by look-up tables as described previously. The compensators are quartz crystals which act to compensate for any ‘beam walk’ that may occur as a result of the twist of the doubling crystal. The quartz crystals are also linked to the look-up tables, so as the doubling crystal moves over the course of a scan the compensator moves as well, in order to maintain optimal beam power. The doubling crystals are not 100% efficient, so both the doubled and fundamental beam leave the crystals. In the doubling only regime (Figure 2.7.5) the light then passes through a series of Pellin-Broca prisms where the fundamental beam is separated out so only the frequency doubled light can pass, via two UV light-reflecting steering mirrors, into the target chamber. In the tripling regime (Figure 2.7.6) the doubled and dye laser beams leave the doubling crystal vertically polarised. The light passes through a $\lambda/2$ wave plate to horizontally polarise the beams before they reach the KD*P tripling crystal. Again, the twist of the tripling crystal is controlled by a look-up table to ensure maximum efficiency. Upon leaving the KD*P crystal the light is directed through a series of dichroic mirrors and a beam dump to separate out any remaining fundamental dye laser beam before the light travels, using the above mentioned steering mirrors, into the vacuum chamber.

Chapter 2. Experimental

Typical beam energies for the UV (doubled) light are around 1.5 – 2.5 mJ. The tripled light generally has lower powers of between 0.5 – 1.5 mJ. These powers depend heavily on the quality of the dye laser beam and, for the tripled light, how well the dye beam and the frequency doubled overlap in the BBO crystal. For the light to be of sufficient intensity for REMPI it has to be focused down to an intense spot, so prior to entering into the target chamber the light passes through a lens of focal length 30 cm. This focuses the beam down into an intense spot of radius 0.15 mm, area $7.1 \times 10^{-4} \text{ cm}^2$. The resulting power density per pulse is then:

$$\frac{1 \times 10^{-3}}{7.1 \times 10^{-4}} \cdot \frac{1}{4 \times 10^{-9}} = 0.35 \text{ GW cm}^{-2} \quad 2.7.10$$

for an average pulse length of 4 ns at the lens focus. The laser pulses at 10 Hz, so this power density must be multiplied by 10 Hz to give a time-averaged power density of 3.5 GW cm^{-2} , which is in agreement with groups who have successfully carried out REMPI of H_2 .^{15,16}

To minimise stray photoelectrons from reflecting off the chamber walls, baffles are employed. Scattered photons from the laser beam could release photoelectrons from the steel vacuum chamber walls, which could ionise other gas molecules in the chamber and swamp the HD REMPI signals. To reduce the possibility of this occurring a set of conical baffles sit just inside the quartz entry window to the chamber, to minimise the stray light entering the chamber. Attached to the end of the baffles is a copper tube of diameter 10 mm, the inner surface of which is roughened, so that any stray light that passes through the baffles will be reflected around the inside of the copper tube and hence does not reach the interaction region of the time-of-flight mass spectrometer.

As a final measure to reduce a scattered light the exit window is at Brewster's angle, this means that the window is held at an angle so that the reflections off its surface are minimal and the UV light should be perfectly transmitted through the quartz. The Brewster's Angle for a quartz surface is calculated as follows:

$$\Theta_B = \arctan\left(\frac{n_2}{n_1}\right) \quad 2.7.11$$

where Θ_B is the Brewster's angle and n_1 and n_2 are the refractive indices of the two media. In this case the two media are air and silica which have refractive indices for UV of 1 and 1.53 respectively, so the equation becomes:

$$\Theta_B = \arctan\left(\frac{1.53}{1}\right) \quad 2.7.12$$

Therefore, the Brewster's angle for the exit window of the vacuum chamber is 56.8° . The window has been designed to be an add-on to the existing exit viewport on the chamber, a schematic of which is shown below in Figure 2.7.7.

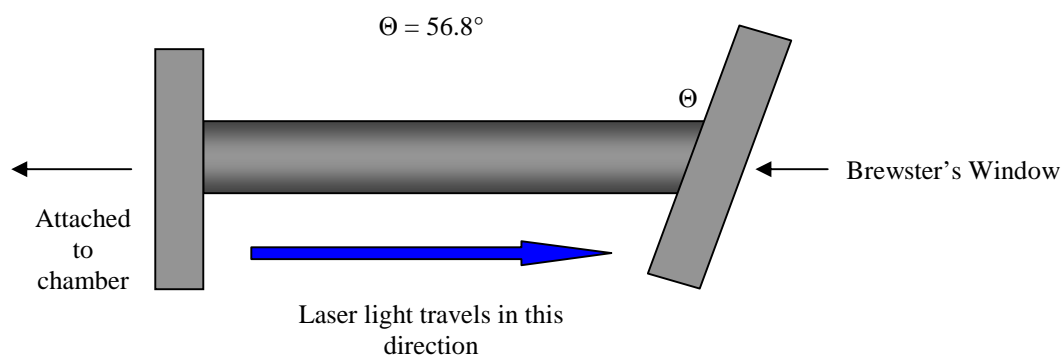


Figure 2.7.7 Schematic of Brewster's Angle window.

2.8 Resonance Enhanced Multiphoton Ionisation (REMPI)

Resonance Enhanced Multiphoton Ionisation (REMPI) is a well established laser technique which allows the state specific ionisation of molecules.^{15,17} The REMPI process uses one or more photons to excite a molecule to a resonant electronic state; the molecule is then ionised with further photons and the ions are detected using a time-of-flight mass spectrometer (TOFMS). REMPI processes are labelled (X+Y) where X corresponds to the number of photons required to excite the molecule to the

resonant state and Y is the number of photons used to ionise the molecule from the resonant electronic state. It is possible to excite a molecule via a non-resonant ‘virtual state’ if more than one photon is used.^{17,18} A virtual state is not an eigenstate of the molecule and is very short lived ($\sim 10^{-15}$ s). As a result of this the photon density must be high enough for the relevant number of photons to be absorbed by the molecule before the virtual state decays. It is not necessary for the photons to be of the same frequency as long as the combination of their energies is sufficient to excite the molecule to the resonant state.¹⁸ Figure 2.8.1 is a schematic of the (1+1) and (2+1) REMPI schemes.

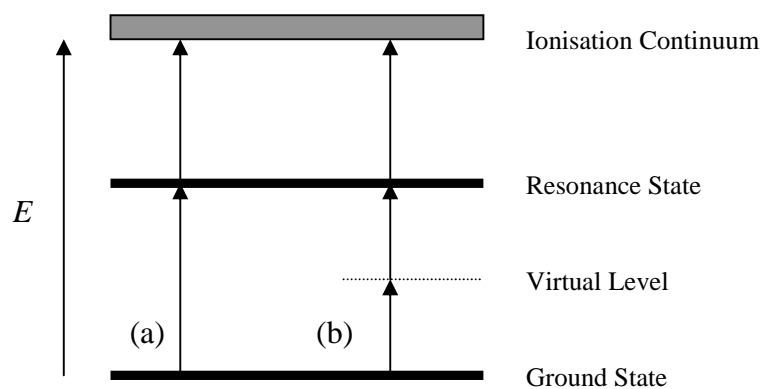


Figure 2.8.1. Schematic diagram of the (1+1) and (2+1) REMPI processes.

To state selectively ionise HD a (2+1) REMPI scheme is required. This is a well understood scheme and shown in Figure 2.8.2 below.

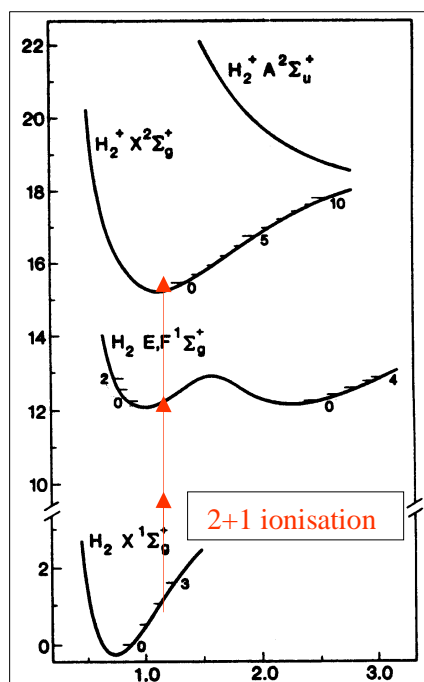


Figure 2.8.2 (2+1) REMPI scheme taken from reference ¹⁵

REMPI has advantages over other laser techniques such as Laser Induced Fluorescence (LIF) as it detects ions rather than photons. The detection of ions is more efficient than the detection of photons and so REMPI is a more sensitive spectroscopic technique.¹⁷ REMPI has advantages over non-resonant multi-photon ionisation because the ionisation process goes via a comparatively long-lived resonance state, hence there is a bigger cross section for a resonantly excited molecule absorbing another photon and being ionised than a non-resonantly excited molecule, which will increase signal strength.

Two photons are used to excite the HD molecules from a specific ro-vibrational level in the ground electronic state, $X^1\Sigma_g^+(v'', J'')$, via a virtual level to the ground vibrational level of $E,F^1\Sigma_g^+$ resonant electronic state. A third photon of the same frequency as the previous two photons is then used to ionise the HD. As the state selective step is a two photon process the change in the rotational quantum number is J is $\Delta J = 0, \pm 2$. The energy of the photons required for these transitions are calculated using the standard spectroscopic equations for electronic, rotational and vibrational energies, these energies are then converted to wavelength.

Chapter 2. Experimental

$$E_v = \left(v + \frac{1}{2} \right) \omega_e - \left(v + \frac{1}{2} \right)^2 \omega_e x_e \quad 2.8.1$$

and

$$E_J = \left[B_e - \alpha \left(v + \frac{1}{2} \right) \right] J(J+1) - DJ^2(J+1)^2 \quad 2.8.2$$

In the above equations the terms have the following definitions:

E_v is the energy of the vibrational state, vibrational quantum number v

E_J is the energy of the rotational states, rotational quantum number J

ω_e is the fundamental vibration wavenumber

x_e is the anharmonicity constant

B_e is the equilibrium value of the rotational constant B

α is a vibration-rotation interaction molecular constant

D is the centrifugal distortion constant

The total energy of each state is given by:

$$E_{total} = E_{elec} + E_v + E_J \quad 2.8.3$$

where E_{elec} is the energy of the electronic state.

The constants required in these equations are widely known and the values used in these experiments come from the NIST online database. An example of the calculated photon wavelengths for HD $v = 1$ are shown in Table 2 below.

| J'' | v'' | λ / nm |
|-------|-------|-----------------------|
| 0 | 1 | 209.0118 |
| 1 | 1 | 209.0937 |
| 2 | 1 | 209.2568 |
| 3 | 1 | 209.5002 |
| 4 | 1 | 209.8222 |
| 5 | 1 | 210.2206 |
| 6 | 1 | 210.6928 |
| 7 | 1 | 211.2351 |
| 8 | 1 | 211.8437 |
| 9 | 1 | 212.5135 |
| 10 | 1 | 213.2391 |

Table 2. Photon wavelengths for the transition $X^1\Sigma_g^+(v'' = 1, J'') \rightarrow E,F^1\Sigma_g^+(v' = 1, J' = J'')$

As previously described the laser system used in this experiment is tuneable over a range of wavelengths. The wavelength is altered by a stepper motor that moves the grating. This movement is not always 100% accurate due to backlash in the motors that move the gratings which control the wavelength, and hence the REMPI transitions will often occur at different wavelengths to those predicted from the spectroscopic constants. The ‘laser offset’ is the difference between the predicted wavelength for a v'', J'' transition and the wavelength where the transition is actually observed. This offset is constant, so once one v'', J'' transition is found the REMPI spectra can be calibrated to determine which peak corresponds to which transition.

2.9 Commissioning of the Position Sensitive Detector

The Cosmic Dust experiment is designed to provide information about how the 4.5 eV of H_2 binding energy is partitioned between internal excitation and the dust grain surface. The experimental set-up described so far allows the ro-vibrational energies to be probed. To gain a more complete picture the translational energy needs to be known as well. This can be achieved by the use of a position sensitive detector (PSD). In this section the experimental set-up for the PSD will be described and the attempts made to obtain correct ion images.

Chapter 2. Experimental

The position sensitive detector includes a pair of MCPs that detect the HD^+ ions, as described previously. The MCPs are supported by two partially metallised ceramic rings, behind which is an anode that consists of two wire-wound delay lines: one delay line for the x dimension and the other for the y dimension. Each of the delay lines is made up of a pair of wires wound round a former to make a plane perpendicular to the axis of the TOFMS. From each pair of wires, one is the signal wire that is used to collect the pulse of electrons emitted from the MCPs; the other wire is the reference wire and is appropriately electrically biased to force the electrons onto the signal wire. In the set-up used in the Cosmic Dust experiment the signal wire is at +300 V and the reference at +250 V. Behind the first delay line there is a second identical delay line, which is wound at 90° to the first and still perpendicular to the TOFMS. The two perpendicular delay lines allow for the detection of both the x and y positions of the ion arrivals.

When an ion hits the MCP a pulse of electrons is generated, this pulse then hits the wires of the delay line anode. The position of the ion is recorded by detecting the arrival time of the charge pulse at both ends of the signal wire. The difference between the arrival times of the signal at each end of the wire is proportional to the position of the ion 'hit' on the MCP in the respective dimension. This means the positional information can be encoded by four different arrival times. The propagation delay along the signal wire is constant, therefore the sum of the arrival time at the end of each wire, relative to the arrival time of the ion at the MCP, is constant for each event. This property is used to distinguish real signals from electrical noise. There are a total of five pulses generated by the arrival of one ion on the detector, one from the back of the MCP and four pulses from the two delay lines. It is these times that need to be recorded by the signal processing electronics. To interpret the times that are collected it has been necessary to update the gather software used for the original detector, ensuring that the shorter times are collected before the later times to achieve an accurate mass spectrum.

Velocity map imaging (VMI) involves the mapping of a 3D distribution of charged particles onto a 2D detector; the success of this depends heavily on the electrode configuration used to form the extracting field.¹⁹ There are two widely used set-ups for the electrodes in a time-of-flight: the conventional grid electrodes¹² and a simple

three-plate electrostatic lens configuration, with open electrodes.¹⁹ The electrostatic lens avoids the image distortions that commonly arise with the grid system. The ion lens also has the advantage that particles with the same initial velocity vector are mapped onto the same point on the detector, regardless of their initial distance from the ion lens axis, hence the name velocity map imaging. The performance of VMI depends on the mapping function of the ion optics, which should fulfil the following set of criteria:¹⁹

1. The ‘cloud’ of charged particles moving towards the detector from the ionisation region should be collapsed in one dimension, along the time-of-flight axis for each mass formed. This ‘pancaking’ allows minimal spread in the time-of-flight of the cloud so that mass selectivity and homogeneous detection is achieved.
2. The size of the image must be linearly proportional to the expansion speed for any kinetic energy release.
3. Any shape or directional influence on the ions from lasers or molecular beams should be kept to a minimum, so that any blurring of the image related to the size of the ionisation volume will be small as possible.

With the PSD installed in the Cosmic Dust Experiment and prior to collecting positional information for the formation of HD, several tests were carried out with oxygen. The grids that had originally covered the middle plate and the mouth of the drift tube were removed, with the aim of achieving focusing with an electrostatic lens. Oxygen released directly into the target chamber gave rise to a significant O_2^+ REMPI signal that could be used to collect preliminary images and positional data. Carrying out these tests highlighted several issues, mainly that the ceramic legs of the TOFMS as shown in Figure 2.9.1 become charged and hence distort the image.

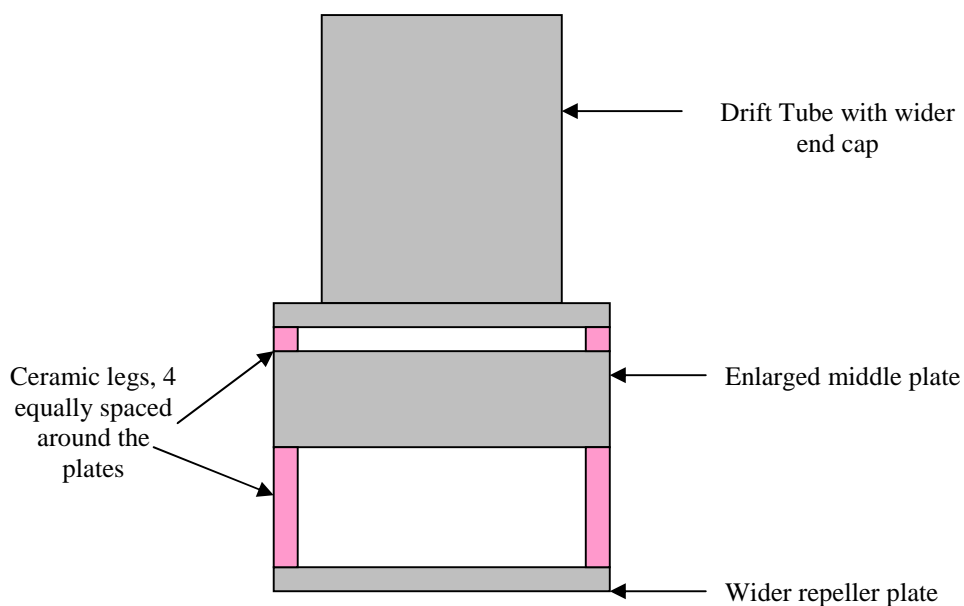


Figure 2.9.1. Schematic of redesign for the source and acceleration regions of the time-of-flight to reduce the effect of charging on the ceramic legs.

The current design of the TOFMS was plotted in SIMION, a computer programme that simulates ion trajectories, in an attempt to further understand the details of the design and charging problems. The effect of the legs could be lessened by increasing the size of the repeller plate and middle plate, but not making the aperture in the centre of the middle plate any larger and having four legs instead of three to make them symmetrical. To achieve cylindrically symmetric fields in the acceleration region an enclosed acceleration region was designed with ceramic insulators separating this from the drift tube as can be seen in Figure 2.9.1. Despite these alterations the effect of the ceramic legs could still be seen and it became apparent that the target and radiation shield surrounding the coldhead were also contributing to the perturbation of the field, hence a radical redesign of the source and acceleration region is required before accurate velocity map imaging can be achieved.

2.10 Summary

This chapter has described the experimental set-up used to probe the internal energies HD formed on a HOPG surface under astrophysically relevant conditions. The laser system and REMPI technique employed has also been discussed. The following chapters will describe the results obtained from these experiments.

2.11 References

- 1 E. E. Marinero, C. T. Rettner, and R. N. Zare, *Physical Review Letters* **48**, 1323 (1982).
- 2 J. S. A. Perry, J. M. Gingell, K. A. Newson, J. To, N. Watanabe, and S. D. Price, *Measurement Science & Technology* **13**, 1414 (2002).
- 3 J. E. Dyson and D. A. Williams, *The Physics of the Interstellar Medium*, 2nd ed ed. (Institute of Physics, Bristol, 1997).
- 4 D. P. Higgins, R. W. McCullough, J. Geddes, J. M. Woolsey, M. Schlapp, and H. B. Gilbody, *Advances in Engineering Materials* **99-1**, 177 (1995).
- 5 R. W. McCullough, in *Application of Accelerators in Research and Industry*, edited by J. L. Duggan and I. L. Morgan (AIP Press, New York, 1997), pp. 275.
- 6 H. Wise and B. J. Wood, *Advances in Atomic and Molecular Physics* **3**, 291 (1967).
- 7 A. Donnelly, M. P. Hughes, J. Geddes, and H. B. Gilbody, *Measurement Science & Technology* **3**, 528 (1992).
- 8 J. M. Greenberg, *Surface Science* **500**, 793 (2002).
- 9 A. S. Bolina, A. J. Wolff, and W. A. Brown, *Journal of Chemical Physics* **122** (2005).
- 10 V. Pirronello, C. Liu, L. Y. Shen, and G. Vidali, *Astrophysical Journal* **475**, L69 (1997).
- 11 R. Berman, E. L. Foster, and J. M. Ziman, *Proceedings of the Royal Society A* **231**, 130 (1955).
- 12 W. C. Wiley and I. H. McLaren, *Review of Scientific Instruments* **26**, 1150 (1955).
- 13 J.W.J. Hawkes, *Optoelectronics an Introduction*, 3rd ed. (Prentice Hall Europe, 1998).
- 14 J.W.J. Hawkes, *Lasers, Principles and Applications*, 1st ed. (Prentice Hall Europe, 1987).
- 15 K. D. Rinnen, M. A. Buntine, D. A. V. Kliner, R. N. Zare, and W. M. Huo, *Journal of Chemical Physics* **95**, 214 (1991).
- 16 D. J. Kligler, J. Bokor, and C. K. Rhodes, *Physical Review A* **21**, 607 (1980).
- 17 S H Lin, H J Neusser, E J Schlag, *Multiphoton Spectroscopy of Molecules*, 1st ed. (Academic Press Inc, 1984).
- 18 J M Hollas, *Modern Spectroscopy*, 4th ed. (John Wiley & Sons Ltd, 2004).
- 19 A. Eppink and D. H. Parker, *Review of Scientific Instruments* **68**, 3477 (1997).

Chapter 3

Results of the Formation of HD on a Graphite Surface

Overview

This chapter discusses the results obtained from the cosmic dust experiment. The particular experimental details and the data analysis procedures are described below. The results obtained for the formation of HD on a cold HOPG surface are presented in detail and compared with the literature.

3.1 Experimental Methods

This section describes the experimental procedures used to collect the relevant data to calculate the rotational populations, resulting in the determination of the average rotational temperature of the nascent HD molecules. The experiments described in this chapter focussed on the ro-vibrational states of $v'' = 3 - 7$. The data collection was carried out in two parts with the vibrational states $v'' = 3$ and 4 detected initially, followed by a brief hiatus, due to problems resulting from a power failure, after which the $v'' = 5 - 7$ states were observed. During the detection of $v'' = 3, 4$ the H₂ and D₂ sources were set a pressures of 0.24 Torr and 0.2 Torr respectively, this resulted in a target chamber pressure of 1.5×10^{-7} Torr. The source pressures were raised for $v'' = 5 - 7$ to 0.37 Torr for H₂ and 0.29 for D₂, with a background chamber pressure of 7×10^{-8} Torr. The change in the source pressure was not for any experimental advantage, simply that the calibration in the Pirani ion gauge had altered with time.

Once it has been decided which ro-vibrational line of nascent HD is to be probed the relevant wavelengths are calculated, as discussed in Chapter 2. A 'look-up' table for these wavelengths is then set up to allow us to scan the dye laser without considerable power fluctuations. In order to record the data from the REMPI process, the data collection PC for the time-of-flight mass spectrometer (TOFMS) uses a program that communicates with the laser. This program sets a wavelength range over which to scan the laser, in small, incremental steps which are typically 0.003 nm in size. The laser can be set to dwell at each wavelength point for a given accumulation time. This length of time depends on the strength of the REMPI signal and can range from 30 s for a strong signal to 320 s for a weak signal. Before each scan the HOPG surface is

heated to 500 K and then allowed to cool back down to 15 K to clean the surface. The heating and cooling process takes approximately 20 minutes.

The area under a REMPI peak is proportional to the rotational population. To be able to correctly determine the rotational populations of the nascent HD molecules, the counting electronic of the TOFMS are set to integrate only over flight times that contain HD^+ ions. To determine this flight time a photoelectron mass spectrum is taken. This is achieved by allowing the off resonance laser beam into the target chamber. The laser beam creates photoelectrons by stray photons hitting the stainless steel chamber walls and releasing electrons. The photoelectrons will ionise the background gas in the chamber from which H^+ can easily be identified in a mass spectrum. Once it is known where H^+ lies in the mass spectrum the positions of the other lines observed can be assigned to HD^+ and D_2^+ given the differences in mass. An integration window, that only encompasses the HD^+ resonance, can then be chosen for recording ions during the experiment. Figure 3.1.1 below shows an on resonance mass spectrum for $\nu'' = 4, J'' = 1$. The H^+ peak appears at approximately 250 ns, H_2^+ at 680 ns, HD^+ at 940 ns and D_2^+ at 1250 ns.

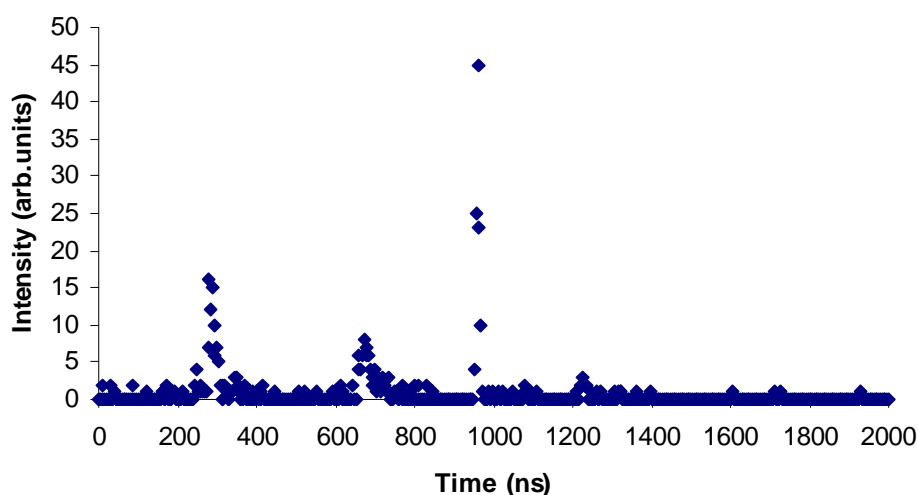


Figure 3.1.1 On resonance mass spectrum for $\nu'' = 4, J'' = 1$, showing the peaks for H^+ , H_2^+ , HD^+ and D_2^+ .

The timing electronics of the TOFMS used to count the ions are only fast enough to accurately count one ion of a given mass per laser shot. This is due to the ‘dead time’

Chapter 3. Results of the Formation of HD on a Graphite Surface

associated with the constant fraction discriminator, which means that any ions that arrive at the detector within this dead time will not be counted. The laser has a repetition rate of 10 Hz so, to avoid counting an incorrect number of ions per wavelength step, the laser power must be low enough to fulfil the relationship:

$$\frac{\text{Ion of a given mass count per laser step}}{10 \times (\text{accumulation time})} \leq 1 \quad 3.1.1$$

If required the laser power can be adjusted to ensure that this condition is met.

3.1.1 Calibration of Laser Power

The output power of the laser varies as it scans across the wavelength range, due to the laser dyes used having output powers that are wavelength dependent. The organic dyes have an optimum power output at a given wavelength, scanning the wavelength away from this optimum reduces the efficiency of the dyes. To record accurate rotational populations of the nascent formed HD molecules the signal area must be corrected for laser power. The intensities of the ion signals detected using the TOFMS vary with the laser output power and this variation follows the power dependence:^{1,2}

$$\text{Ion signal} \propto (\text{laser power})^n \quad 3.1.2$$

To determine the value of n in the above equation, HD⁺ signals are measured for different laser outputs. A graph of ln(laser power / mJ) versus ln(ion signal) is plotted, this gives rise to a straight line with a gradient n . This has been carried out for HD $\nu'' = 3 - 7$, an example of such a plot is shown in Figure 3.1.2 and a table of the values obtained for all these vibrational states is presented below.

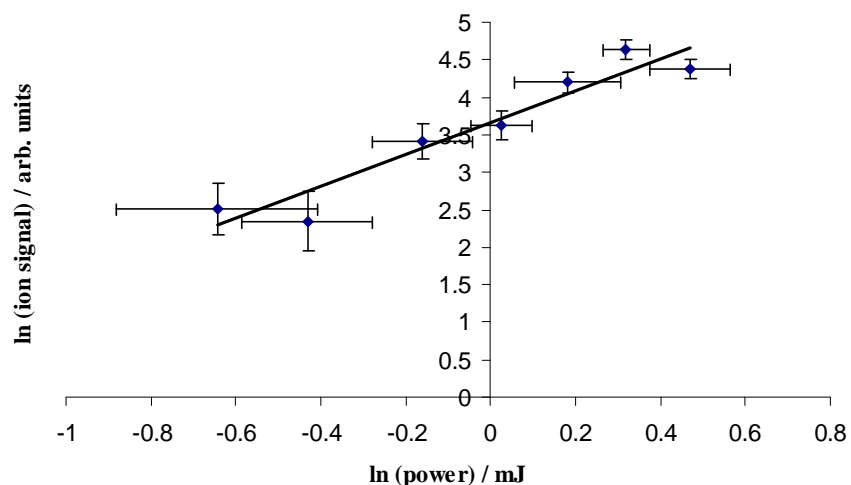


Figure 3.1.2. Plot of $\ln(\text{ion signal})$ vs $\ln(\text{laser power})$ to determine the laser power dependence factor for HD formed in $v'' = 5$. The solid line is a weighted least squares fit, the gradient of which gives the values of n described in the text.

| Vibrational Level | n |
|-------------------|-----------------|
| 3 | 1.43 ± 0.11 |
| 4 | 1.62 ± 0.17 |
| 5 | 2.13 ± 0.29 |
| 6 | 2.69 ± 0.32 |
| 7 | 3.32 ± 1.23 |

Table 1. Table to show the laser power dependence factors determined for each vibrational state of HD.

An average value for n is used for each vibrational state, regardless of the rotational state. The rotational populations of the rotational states are corrected for laser power by dividing the areas under the TOFMS peaks by the laser power raised to the relevant value of n . Given that the ionisation dependence on the laser power follows a power law, a non-saturating 3-photon process would be expected to give a value of $n = 3$.^{1,2} Saturation occurs when more than 16 ions hit the MCP in one laser shot; if a transition is saturating flat topped REMPI peaks are observed. If the ionisation step or 2-photon resonance step of the (2+1) REMPI scheme were saturating a value of $n = 3$ would be expected, so a normal value of n for the 2-photon process would be $n = 2$.^{1,2} Table 1 indicates that $n = 3.32 \pm 1.23$ for $v'' = 7$, this would suggest that the transition

was saturating, however it was not, but given the large error the actual value of n could be nearer 2.

3.1.2 Determination of Rotational Temperature

Once the rotational populations have been found it is possible to determine the average rotational temperature for each vibrational state; this is achieved by constructing a Boltzmann plot. The Boltzmann distribution describes the population of the rotational levels P_J relative to the population of the $J'' = 0$ level:

$$\frac{P_J}{P_0} = g_J(2J + 1)\exp\left(-\left(\frac{E_J}{kT}\right)\right) \quad 3.1.3$$

Where g_J is the nuclear spin degeneracy ($g_J = 1$ for HD), k is Boltzmann's constant, J is the rotational quantum number, E_J is the corresponding rotational energy and T is the temperature.

Rearranging equation 3.1 gives:

$$-k \ln\left(\frac{P_J}{g_J(2J + 1)}\right) + k \ln(P_0) = \frac{E_J}{T} \quad 3.1.4$$

From equation 3.2 we can see that by plotting $-k \ln\left(\frac{P_J}{g_J(2J + 1)}\right)$ vs E_J gives a straight line, the gradient of which is $1/T$ and the intercept is $k \ln(P_0)$. If the rotational populations previously determined lie along this straight line then the distribution is Boltzmann and the gradient of the least squares fit to the data can be used to find the rotational temperature, T . If the data does not lie on the straight line then the rotational distribution is non-Boltzmann; however, it is still possible to find the average rotational temperature *via* an average rotational energy. This is done using statistical mechanics, which is described below.

The average rotational energy (E_{rot}) is given by:

$$\langle E_{rot} \rangle = \sum_J P_J E_J \quad 3.1.5$$

and then the average rotational temperature is given by:

$$\langle T_{rot} \rangle = \frac{\langle E_{rot} \rangle}{k} \quad 3.1.6$$

A line of best fit to a Boltzmann plot where the data does not lie on the straight line can also give us the average rotational temperature from the gradient. The rotational populations are found using equation 3.1.7.

$$P_J = \frac{I_J}{\sum_J I_J} \quad 3.1.7$$

Where I_J is the power normalised ion signal detected for the rotational state J .

3.2 HD Formation on HOPG

This section will describe the results obtained for the formation of HD from H and D-atoms recombining on a HOPG surface held at 15 K. Initially the vibrational states $v'' = 3$ and 4 were probed followed by $v'' = 5 - 7$. It was observed that the REMPI signals for $v'' = 3$ and 4 were the most intense with $v'' = 4$ giving rise to the largest signals; there was a considerable drop in signal strength from $v'' = 4$ to $v'' = 5$ with a continuous decrease to $v'' = 7$.

3.2.1 HD formed in $v'' = 3$ and 4

The reaction of H and D atoms on a cold (15 K) graphite surface has been probed to discover if the reaction gives rise to nascent HD formed in the $v'' = 3$ and 4 vibrational states. There are a number of different potential vibrational levels within the intermediate $E, F \ ^1\Sigma_g^+$ state, each of which has a different probability of being populated from $v'' = 3$ or $v'' = 4$. To determine which transition has the highest probability, and hence best to use for the REMPI experiment, the Franck-Condon factors (FCF)³ for the different transitions were considered. For both $v'' = 3$ and 4 the most appropriate intermediate state was the $E, F \ ^1\Sigma_g^+ \ v' = 1$ for which the FCFs were

0.18 and 0.28 for $v'' = 3$ and 4 respectively. Each of the ro-vibrational ($v'' = 3 - 4$, $J'' = 0 - 6$) levels gave a detectable rise in the REMPI ion count, as shown in Figure 3.2.1. The experiments showed that these vibrational states are in fact significantly populated and the rotational states $J'' = 0 - 6$ were observed. A typical signal-to-noise (S/N) value for a strong signal is in excess of 20 and for a weak signal the S/N is approximately 5. The integrated area under the REMPI peak can be processed to give the relative population of the ro-vibrational states from which the REMPI event occurred. The higher rotational states of $J'' = 7$ and 8 were searched for by scanning over the relevant wavelengths (for $v'' = 4$, $J'' = 7$ and 8, $\lambda = 229.581$ nm and 230.13 nm respectively, for $v'' = 3$, $J'' = 7$ and 8, $\lambda = 221.902$ nm and 222.467 nm respectively) for 200 s a point. However, these states were not detected (S/N = -0.2) which indicates that either HD is not formed in these higher rotational states or the population of these states is so small that it was masked by the experimental background counts. These background counts result from ionisation events initiated by photoelectrons formed by stray laser photons, which have been accelerated across the source region of the time of flight mass spectrometer.

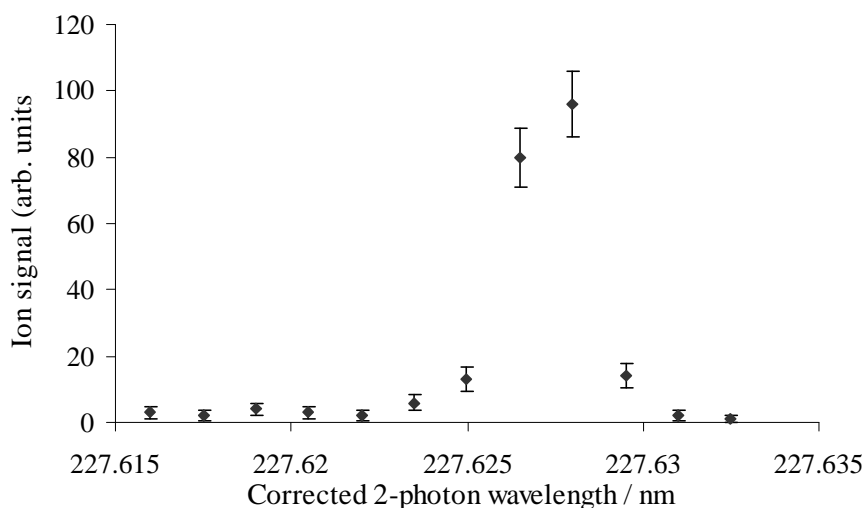


Figure 3.2.1 REMPI spectrum for the transition $X^1\Sigma_g^+ (v'' = 4, J'' = 1) \rightarrow E, F X^1\Sigma_g^+ (v' = 1, J' = J'')$ from HD formed on a HOPG surface held at 15 K.

Boltzmann analysis, as described previously, is performed on the REMPI signals to give the rotational temperatures, for $v'' = 3$ this was found to be 330 ± 26 K and for $v'' = 4$, 368 ± 22 K. A typical Boltzmann plot is shown in Figure 3.2.2 for the populated levels in $v'' = 4$. As shown in Figure 3.2.2, the fit to the Boltzmann distribution is

good ($r^2 = 0.97$) but not perfect and the experimental data appear as a curve rather than a straight line; this indicates that the detected rotational states have a greater population in low and high J values than a thermal distribution. Previous work⁴ on the vibrational states $v'' = 1$ and 2 of HD has shown the lower vibrational states have lower rotational temperatures than those observed for $v'' = 3$ and 4, indicating that the degree of rotational excitation increases with increasing v'' in the nascent HD. The expectation that the rotational states populated in the recombination of H and D atoms should obey a Boltzmann distribution might not be an obvious one. However, rotational distributions have been observed to be approximately Boltzmann, sometimes with rotational temperature greater than the temperature of the surface.⁵⁻⁸ Experiments carried by Winkler⁷ have shown that the recombination of D atoms on a Ni(110) surface at held at 180 K gave rise to a rotational distribution that was approximately Boltzmann and that the rotational temperature decreased with increasing vibrational quantum number. The rotational temperatures determined by Winkler were also considerably higher than the temperature of the surface. Murphy and Hodgson⁵ observed Boltzmann distributions for the formation of D_2 formed on a Ag(111) surface. The use of (2+1) REMPI allowed Murphy and Hodgson to investigate the rotational temperature of the D_2 formed and it was found that the temperature of the nascent molecules was notably higher than that of the surface, 550 K compared with 210 K.⁵ Rotational temperatures greater than the temperature of the surface on which the molecules were formed is not a general trend. Schröter *et al* observed that when H_2 recombinatively desorbs from Pd(100) the rotational populations do follow a Boltzmann distribution but the rotational temperature (281 K) was lower than the surface temperature (570 K).⁶

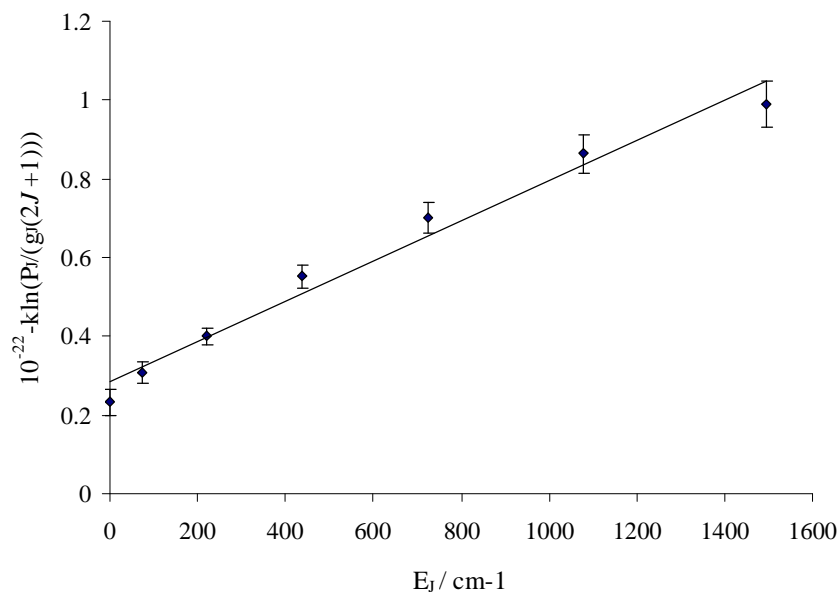


Figure 3.2.2 Boltzmann plot for HD formed in $v'' = 4$ on a HOPG surface held at 15 K. The solid line is a weighed least squares fit to the data, the gradient of which yields the rotational temperature.

Figure 3.2.3 shows the ro-vibrational distribution for $v'' = 3$ and 4.⁹ Quantifying the vibrational distribution is a complex procedure: to be able to calculate the relative populations of the vibrational states from our data it is necessary to allow for the difference in the probability of the REMPI process from different vibrational states. A quantified vibrational distribution would be valuable for the modelling of the energy budget in interstellar clouds.

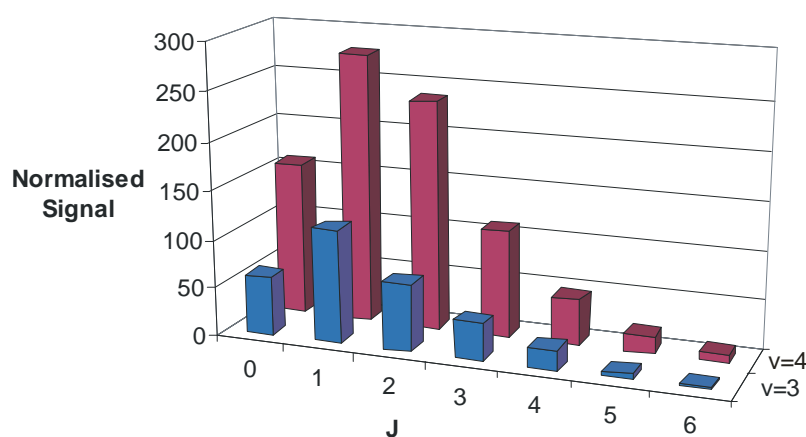


Figure 3.2.3 Ro-vibrational distribution for HD formed on a cold graphite surface in the $v'' = 3$ and 4 vibrational states.

As previously discussed, the REMPI process involves a transition from a (v'', J'') level in the X state to a (v', J') level in the E, F state. These two transitions have different probabilities of occurring for the different values of the rotational and vibrational quantum numbers. A measure of the REMPI transition probability is its two-photon transition moment $|M_{fo}|^2$. The two-photon transition moment has been calculated by Huo and Zare¹⁰ for the REMPI transitions of H_2 and HD from different ro-vibrational levels in the X state (v'', J'') via E, F $(v' = 0, J' = J'')$. This work found that the magnitude of $|M_{fo}|^2$ varies significantly with the value of v'' but is not strongly dependent on the value of J'' . Huo and Zare compared their calculated values of $|M_{fo}|^2$ for the H_2 transitions with the $X \rightarrow E, F$ Franck Condon factors (FCFs), which are a measure of the overlap of two vibrational states.¹⁰ The work by Huo and Zare found that the probability of a REMPI transition occurring is dominated by the relevant FCF. When considering HD we see that upon comparison of the two-photon transition moments calculated by Huo and Zare with the relevant FCFs, the probability of a REMPI transition occurring is again dominated by the Franck Condon factor. Table 2 details the values Huo and Zare calculated for $|M_{fo}|^2$ and the corresponding FCFs³ for the HD transitions $X \ ^1\Sigma_g^+ v'' = 1 - 6$ to $E, F \ ^1\Sigma_g^+ v' = 0$. Table 2 also shows the FCFs for the transitions that were actually used during the experiments detailed in this thesis. For $v'' = 4, 5$ and 6 it is obvious from the comparison of FCFs why different E, F levels were chosen, as the higher the FCF the more likely the transition.

| v'', v' | $ M_{fo} ^2$ | FCFs for transition to $E, F v' = 0$ | v'', v' used in experiments | FCFs |
|-----------|--------------|--|----------------------------------|------|
| 1, 0 | 22.12 | 0.31 | 1,0 | 0.31 |
| 2, 0 | 28.50 | 0.33 | 2,0 | 0.33 |
| 3, 0 | 19.07 | 0.18 | 3,1 | 0.18 |
| 4, 0 | 7.18 | 0.053 | 4,1 | 0.28 |
| 5, 0 | 1.53 | 0.0089 | 5,1 | 0.15 |
| 6, 0 | 0.18 | 0.0008 | 6,2 | 0.24 |

Table 2. Table detailing the different Franck Condon factors³ and $|M_{fo}|^2$ for HD in $v'' = 1 - 6$, $v'' = 7$ is not included in this table as Huo and Zare¹⁰ did not calculate values of $|M_{fo}|^2$ for vibrational states higher than $v'' = 6$.

To probe the $v'' = 3$ and 4 vibrational states of HD the intermediate state of $E, F v' = 1$ was used not $v' = 0$, which was investigated by Huo and Zare.¹⁰ As previously mentioned the $E, F v' = 1$ state was chosen because of its significantly larger FCF with $v'' = 3$ and 4. There are no calculations of $|M_{fo}|^2$ in the literature for the ionisation of HD ($v'' = 3, 4$) via the $E, F v' = 1$ state. Hence, we have extended the conclusions made by Huo and Zare and assume that the REMPI transition probability is dominated by the applicable FCFs. This approximation also includes the assumption that $|M_{fo}|^2$ does not change significantly with J'' , as observed by Huo and Zare. Therefore, to put the relative rotational populations of all the vibrational states in the same units, the REMPI signal must be scaled by the Franck Condon factor for the transition. Considering the difference between the relevant FCFs and the calculated $|M_{fo}|^2$ for adjacent vibrational levels for the ionisation of HD via $E, F v' = 0$ in the X state, the uncertainty introduced by the use of the FCFs to estimate the transition strength is approximately 25%.

Figure 3.2.3 shows scaled $v'' = 3$ and 4 data; this plot indicates that $v'' = 4$ is approximately twice as populated as $v'' = 3$. The sum of the scaled rotational populations for each vibrational state give a population ratio, $v'' = 4$ to $v'' = 3$ of 1.8 ± 0.6 . For the above comparison to be valid it has been assumed that several experimental parameters are essentially constant for the two sets of experiments. For example, any dramatic changes in the atom fluxes from the sources or changes in the position of the laser focus would invalidate the comparison between $v'' = 3$ and 4. However, since these data sets were recorded consecutively, every attempt was made to ensure the experimental conditions remained constant throughout. In particular the source pressures, laser alignment, beam shape and the surface cleaning regime were effectively identical for both experiments. Therefore, it is felt that this comparison is reliable and indicative of the relative fluxes. The TOFMS measures the density of the ionised nascent HD molecules; this measurement is related to the desorbing flux by the velocity of the ion.

$$\text{Flux } (F) = \text{velocity}(v) \times \text{density}(\rho) \quad 3.2.1$$

Flux is the important parameter for astrophysical modelling, but given that the velocity of the nascent molecules is not measured directly in these experiments the

flux of the HD can only be inferred. From the width of the TOF peaks the kinetic energy of the HD^+ ions is assumed to be below 1 eV, as is discussed in detail in Section 3.3.1. Given this observation, the fluxes of $v'' = 3$ and 4 from the surface are assumed to be approximately equal.

To achieve a more complete comparison of the ro-vibrational populations of HD the data collected for $v'' = 1$ and 2⁴ have also been scaled by the relevant FCFs, 0.31 and 0.33 respectively (Figure 3.2.4). The data for these lower vibrational states was recorded some time ago, although the experimental conditions were very similar; hence, there is obviously more uncertainty attached to the relative populations calculated. The relative population plot provides an order of magnitude estimate of the population of $v'' = 1$ and 2 with respect to $v'' = 3$ and 4. Even taking into consideration the increased uncertainty associated with the relative vibrational populations, Figure 3.2.4 clearly shows that $v'' = 4$ has the greatest population.

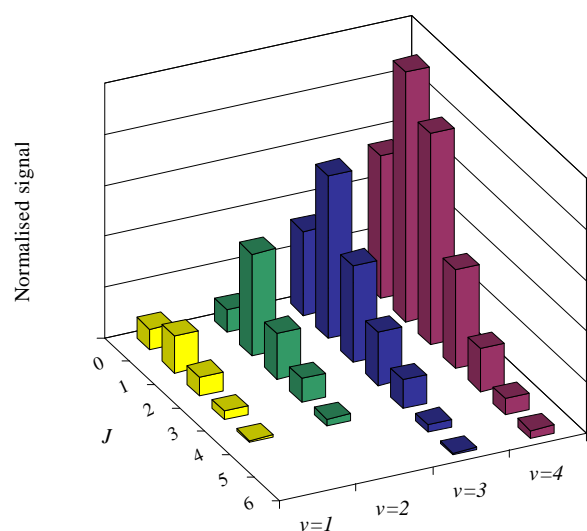


Figure 3.2.4 Relative ro-vibrational populations for HD formed in $v'' = 1 - 4$ on a HOPG surface at 15 K.

3.2.2 HD formed in $v'' = 5, 6$ and 7

As a logical continuation from the observations of $v'' = 3$ and 4, HD formed in the ro-vibrational states $v'' = 5, 6$ and 7 have been probed.¹¹ Initially there was some difficulty finding the exact position of the REMPI signals: this was due to inaccuracies in the rotational constants provided by the NIST database. These constants were initially used in the wavelength calculations and the values calculated

Chapter 3. Results of the Formation of HD on a Graphite Surface

for the transition from the X to E , F states were then incorrect for these higher vibrational states. The rotational constants obtained from the NIST database were $B_e = 24.568 \text{ cm}^{-1}$ and $D_e = 0.0123 \text{ cm}^{-1}$. The inaccuracy in the calculations indicates that care has to be taken when using such values to accurately calculate wavelengths. The wavelengths for the required REMPI transitions were recalculated using rotational constants found by Dabrowski and Herzberg.¹² The rotational constants are shown in Table 3 below.

| $v'(E,F)$ | B_v / cm^{-1} | D_v / cm^{-1} |
|-----------|------------------------|------------------------|
| 0 | 23.924 | 0.0123 |
| 1 | 22.636 | 0.0118 |
| 2 | 20.862 | 0.083 |
| 3 | 14.58 | 0.0997 |
| 4 | 9.871 | 0.0197 |
| 5 | 8.51 | 0.0074 |

Table 3. Details of the spectroscopic constants obtained from Dabrowski and Herzberg,¹² used in the calculation of the wavelengths required for REMPI transitions in $v'' = 5, 6$ and 7 . These values should be compared to the constants obtained from NIST which were $B_e = 24.568 \text{ cm}^{-1}$ and $D_e = 0.0123 \text{ cm}^{-1}$.

The values of B_v and D_v shown above were then used in the following standard equation to give the total ro-vibrational energy of the E , F state.

$$T(J, v) = (B_v + \alpha(v - \frac{1}{2}))J(J + 1) - DJ^2(J + 1)^2 + \omega_e(v + \frac{1}{2}) - \omega_e x_e(v + \frac{1}{2})^2 \quad 3.2.2$$

where:

$T(J, v)$ is the total energy for both the vibrational and rotational states, quantum numbers v and J respectively.

B_v is the state specific value of the rotational constant B .

D is the centrifugal distortion coefficient.

ω_e is the fundamental vibration wavenumber.

x_e is the anharmonicity constant.

All these values, except B_v and D_v came from the NIST database.

Once the correct wavelengths had been calculated and the first $v'' = 5$ signal found it was possible to successfully predict where the other lines should lie. Considering the high population of $v'' = 4$ it might be expected that $v'' = 5$ would have a comparable population, if not a higher population. However this was not found to be the case and the populations of the higher vibrational states were observed to have considerably lower populations than $v'' = 4$. For $v'' = 5$ detection of $J'' = 0 - 6$ rotational states was possible but for $v'' = 6$ and 7 the only states observed were $J'' = 0 - 4$ and $J'' = 0 - 3$ respectively. Due to the weakness of the REMPI transitions for $v'' = 5 - 7$ longer scan times were required, generally scanning over 12 points, residing at each point for between 120 - 320 s, depending on the strength of the signal. For strong transitions ($v'' = 5, J'' = 2$) typical signal-to-noise (S/N) values were approximately 3, whereas for weak transitions the S/N values were around 0.9. Scans were carried out looking for the higher rotational states in $v'' = 6$ and 7 but it was not possible to detect them with our current sensitivity. These non-detections indicate either that HD is not formed in these rotational states, or the population of these states is so small that it is masked by the experimental background counts. A typical S/N value for a non-detection was approximately -0.2 ± 0.01 .

Boltzmann analysis was performed for all the data collected and the average rotational temperatures calculated. These were found to be 338 ± 22 K for $v'' = 5$, 266 ± 55 K for $v'' = 6$ and 336 ± 102 K for $v'' = 7$. For the lower vibrational states of $v'' = 1 - 4$ it had been observed that with increasing vibrational quantum number there was greater rotational excitation of the nascent HD. However, the results for $v'' = 5 - 7$ do not seem to follow this trend. Taking into account the errors, the average rotational temperatures for $v'' = 5 - 7$ appear to have reached a plateau.

| Ground State, X $^1\Sigma_g^+$ v'', J'' states detected | Resonance state, $E, F X ^1\Sigma_g^+ (J' = J'')$ | Rotational Temperature (K) | Average rotational energy (cm^{-1}) |
|--|--|----------------------------------|--|
| $v'' = 0$, undetected | 0 | - | - |
| $v'' = 1, J'' = 0 - 4$ | 0 | 246 ± 24 | 177 ± 4 |
| $v'' = 2, J'' = 0 - 4$ | 0 | 282 ± 31 | 180 ± 30 |
| $v'' = 3, J'' = 0 - 6$ | 1 | 330 ± 26 | 213 ± 4 |
| $v'' = 4, J'' = 0 - 6$ | 1 | 368 ± 22 | 217 ± 3 |
| $v'' = 5, J'' = 0 - 6$ | 1 | 338 ± 20 | 224 ± 3 |
| $v'' = 6, J'' = 0 - 4$ | 2 | 267 ± 55 | 163 ± 6 |
| $v'' = 7, J'' = 0 - 3$ | 3 | 337 ± 102 | 147 ± 8 |

Table 4. Shows a complete list of all the ro-vibrational states detected and the relevant average rotational temperatures.

The deviation from the originally observed trend is likely to be due to the uncertainty in the $v'' = 5, 6$ and 7 results. This uncertainty is mainly as a result of the REMPI signals being noticeably weaker, thus the scan times were longer, which meant the laser power would fluctuate over the course of the scan, hence affecting the uncertainty of the results. Despite the uncertainty in the data obtained for $v'' = 5 - 7$ the result is still significant as it shows that H and D atoms recombining on a graphite surface held at 15 K will populate these vibrational states and that these states are not as strongly populated as $v'' = 3$ and 4 . The degree of fit (r^2) for each Boltzmann plot was calculated to be 0.95, 0.97 and 0.99 for $v'' = 5, 6$ and 7 respectively and as with $v'' = 3$ and 4 these fits are good but not perfect and the Boltzmann plots again describe a curve rather than a straight line. Hence, the rotational temperature is not the best way of characterising the rotational distribution, so the average rotational energies for $v'' = 1 - 7$ are shown in Table 4 above.

To compare the data obtained for $v'' = 5 - 7$ to the data for the lower vibrational states $v'' = 1 - 4$ it was necessary to scale the original ro-vibrational populations using the FCFs by the method discussed previously. The resulting plot is shown in Figure 3.2.5 and clearly indicates a population maximum at $v'' = 4$, with $v'' = 3$ and 2 having the

next largest populations. The TOFMS only measures the density of the HD molecules, not the flux. Density and flux are related to each other by velocity, so assuming that the nascent HD molecules do not have markedly different velocities then the fluxes of HD in the detected v, J states should be represented by the density for the vibrational states and therefore should be comparable. As discussed above the data collection for $v'' = 1$ and 2 required a different laser set-up, so there are some experimental differences between the two sets of data, but it is felt that the comparison is still valid.

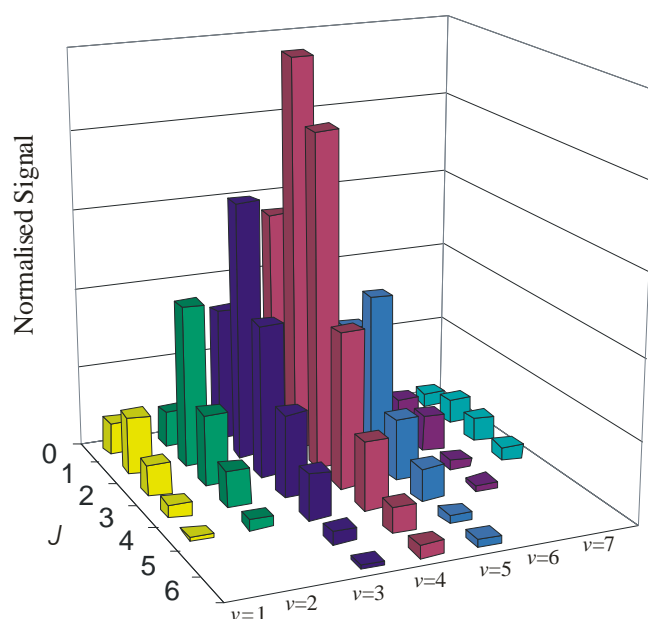


Figure 3.2.5 Derived relative ro-vibrational populations of HD formed on a HOPG surface at 15 K in the vibrational states $v'' = 1 - 7$. These ro-vibrational states are placed on a relative scale applying the methodology described in the text.

In an attempt to further validate this inter-comparison between the vibrational populations (Fig 3.2.5) a series of consecutive scans were carried out, detecting HD formed in $v'' = 3 - 7$, with the data for an individual vibrational state collected in a single day. Three REMPI scans were recorded, monitoring the signal from the most abundant J'' state in each vibrational level. The Franck Condon weighted REMPI signals from these individual rotational states were then used to scale the rotational populations for the other remaining J'' states in the different vibrational states to arrive at an estimate of the full ro-vibrational distribution, which is shown below in Figure 3.2.6. Using this different scaling method the populations of $v'' = 3$ and $v'' = 5$ are reduced relative to the previous data set, but the population of $v'' = 4$ is very similar.

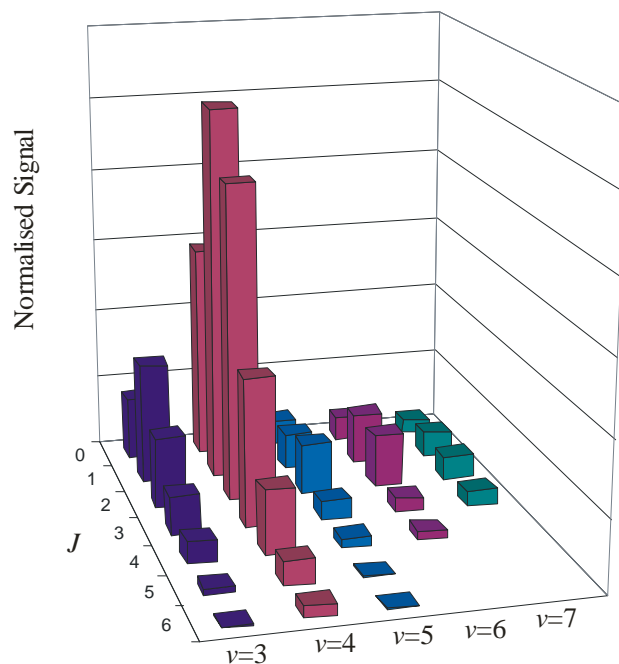


Figure 3.2.6 Relative ro-vibrational populations of HD formed on a HOPG surface at 15 K in the vibrational states $\nu'' = 3 - 7$. The data used to compile this plot was obtained from a series of consecutive scans.

When considering which of the two scaling methodologies provides the best description of the ro-vibrational distribution, a variety of factors need to be taken into account. The data used in Figure 3.2.5 was collected over a long period of time and included a significant alteration to the laser system, changing from frequency tripling to frequency doubling when moving from detecting $\nu'' = 1, 2$ to $\nu'' = 3 - 7$. However, significantly more data was recorded to yield the distributions of $\nu'' = 1 - 7$, eight spectra per J'' for each ν'' state instead of three per J'' state as was the case for Figure 3.2.6. The timescale over which the data in Figure 3.2.5 was collected was long, over several months, whereas the results shown in Figure 3.2.6 were obtained over a much shorter period, several weeks. Over a shorter time, it was possible to ensure that the experimental conditions, the laser beam alignment, beam shape and atom flux for each scan were close to identical for the scaling presented in Figure 3.2.6; the only parameter that varied was the laser power, a variation which is accounted for in the data analysis. However, every effort was made to maintain constant experimental conditions over the longer time period involved in recording the data presented in Figure 3.2.5. Tables 5 and 6 below show the numerical values for the data shown in Figure 3.2.5 and 3.2.6.

| ν'' | J'' | | | | | | |
|---------|-----------|-----------|-----------|----------|----------|---------|---------|
| | 0 | 1 | 2 | 3 | 4 | 5 | 6 |
| 1 | 79 ± 9 | 144 ± 10 | 75 ± 10 | 31 ± 9 | 9 ± 7 | - | - |
| 2 | 89 ± 26 | 400 ± 72 | 180 ± 36 | 93 ± 29 | 26 ± 21 | - | - |
| 3 | 330 ± 65 | 642 ± 105 | 379 ± 86 | 207 ± 55 | 113 ± 53 | 29 ± 16 | 8 ± 9 |
| 4 | 560 ± 137 | 983 ± 190 | 833 ± 127 | 387 ± 83 | 168 ± 46 | 64 ± 23 | 30 ± 13 |
| 5 | 209 ± 31 | 293 ± 36 | 411 ± 51 | 151 ± 23 | 80 ± 17 | 18 ± 11 | 17 ± 11 |
| 6 | 40 ± 13 | 84 ± 19 | 88 ± 19 | 23 ± 10 | 14 ± 8 | - | - |
| 7 | 33 ± 14 | 61 ± 20 | 60 ± 20 | 36 ± 15 | - | - | - |

Table 5. Experimentally estimated ro-vibrational populations for HD formed on a cold (15 K) HOPG surface for the vibrational states $\nu'' = 1 - 7$. The populations are derived using the relevant Franck Condon factors and are also displayed in Figure 3.2.5.

| ν'' | J'' | | | | | | |
|---------|----------|-----------|----------|----------|----------|---------|---------|
| | 0 | 1 | 2 | 3 | 4 | 5 | 6 |
| 3 | 168 ± 30 | 328 ± 42 | 193 ± 33 | 106 ± 24 | 58 ± 18 | 15 ± 9 | 4 ± 5 |
| 4 | 583 ± 45 | 1023 ± 60 | 866 ± 55 | 402 ± 38 | 174 ± 25 | 66 ± 15 | 32 ± 11 |
| 5 | 69 ± 21 | 97 ± 25 | 136 ± 30 | 50 ± 18 | 26 ± 13 | 6 ± 6 | 6 ± 6 |
| 6 | 65 ± 16 | 137 ± 24 | 144 ± 24 | 38 ± 13 | 22 ± 9 | - | - |
| 7 | 36 ± 15 | 67 ± 21 | 66 ± 20 | 39 ± 15 | - | - | - |

Table 6. Ro-vibrational populations for HD formed on a cold (15 K) HOPG surface for the vibrational states $\nu'' = 3 - 7$. This distribution was derived from a series of consecutive scans and is also shown in Figure 3.2.6.

The errors for the values shown in the tables above were calculated by taking the errors ($\pm\sigma$) for the unscaled populations, the calculation of which is described in Appendix B, and dividing by the FCF for that specific $X \ ^1\Sigma_g^+ \nu''$ to $E,F \ ^1\Sigma_g^+ \nu'$ transition. Upon inspection of the uncertainties of each of the two determinations of the (ν'', J'') distribution (Tables 5 and 6) it is apparent that the populations of 19 of the 30 J'' levels that were probed in $\nu'' = 3 - 7$ agree within 1σ ; whilst the populations of 28 of the 30 J'' levels agree within 3σ . Given the previously mentioned considerations

regarding the experimental methodology it would seem that, within our experimental uncertainty, the data presented in Tables 5 and 6 are consistent with sampling the same ro-vibrational distribution.

| ν'' | Relative Population |
|---------|---------------------|
| 1 | 11 ± 3 |
| 2 | 26 ± 8 |
| 3 | 42 ± 14 |
| 4 | 100 ± 3 |
| 5 | 25 ± 13 |
| 6 | 8 ± 6 |
| 7 | 4 ± 3 |

Table 7. Experimentally estimated nascent vibrational distribution for HD formed on a cold HOPG surface.

Therefore, in Table 7 an averaged vibrational distribution is shown, with the relevant uncertainties given by the differences between the two scaled populations. As discussed before, $\nu'' = 1$ and 2 could not be included in the rapid scan experiments, so the data for these vibrational states shown in Table 7 is via the scaling presented in Figure 7. Table 7 clearly indicates that the most significantly populated vibrational state is $\nu'' = 4$ and there is a drop in nascent population for the other vibrational states.

3.3 Energy Partitioning

3.3.1 Translational Energy

As discussed previously in this thesis the aim of these experiments is to determine the ro-vibrational distribution of HD formed on a dust grain analogue surface. The data collected can then be used to discover how much of the 4.5 eV bonding energy will be deposited into the HOPG surface. As described in Chapter 2 a position sensitive detector has been installed to allow the translational energy of the HD to be determined. However, as this piece of equipment has not been used to its full potential, an estimate of the kinetic energy must be made.

It is possible to determine an upper limit for the translational energy of the nascent HD perpendicular to the HOPG surface normal from the temporal widths of the TOFMS peaks. The width of the time-of-flight peaks depends on several factors: the width of a peak resulting from ion with an initial kinetic energy of zero, the instrument function which occurs from experimental parameters including the jitter in the timing electronics and any non-uniformity in the electric fields. If the initial kinetic energy of the ions is greater than zero, then the distribution in velocities of the ions will contribute to the width of the TOFMS peak. It is possible to explain the effect of the initial velocities on the temporal widths of the TOF peaks by considering two ions with the same initial kinetic energy, formed at the same point but travelling in opposite directions: ion 1 moving in the direction of the detector and ion 2 away from the detector (Figure 3.31). Ion 2 will be decelerated by the source field, E_s , until it stops and then it will be turned around and accelerated, but in the direction of the detector, passing through its point of ionisation with its initial speed. The motion of ion 2 will therefore be identical to that of ion 1, but it will lag behind ion 1 by the “turn around time”, which is twice the deceleration time, see Figure 3.3.1 below.

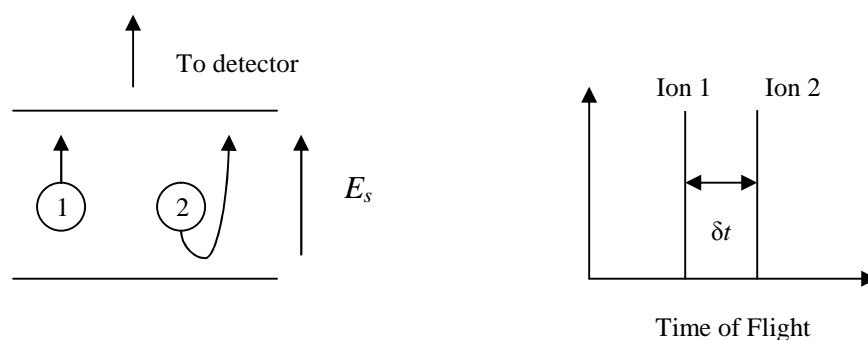


Figure 3.3.1 Schematic of the paths of two ions with opposite initial velocities and their position in the TOFMS.

The turn around time of ion 2 corresponds to the time spread, δt , of the ions hitting the detector. The peak width:¹³

$$\delta t = \frac{2(2mU_0)^{\frac{1}{2}}}{qE_s} \quad 3.3.1$$

where U_0 is the initial kinetic energy of the ions, m is the mass of the ion, q is the charge on the ion and E_s is the electric field in the source region of the TOFMS.

The flight time of an ion with zero kinetic energy, or the “thermal” flight time is given by the following equation:¹⁴

$$t_{\text{expt}} = t_0 \pm \frac{(2mU_0)^{\frac{1}{2}}}{qE_s} \quad 3.3.2$$

where t_{expt} is the measured time-of-flight of the ion with the initial kinetic energy U_0 in the direction of the detector. Given that $U_0 = \frac{1}{2}mv_0^2$, equation 3.3.2 can be rearranged to give:

$$v_z = -\left[t_{\text{expt}} - t_0\right] \frac{qE_s}{m} \quad 3.3.3$$

where v_z is the velocity of the ion in the z direction, that is in the direction of the detector in the TOFMS.

If the kinetic energy of the ions dominates the width of the HD^+ peaks, then the velocity calculated in equation 3.3.3 could be used to calculate the kinetic energy using the standard equation $E = \frac{1}{2}mv^2$. Given the assumption that the entire temporal width of the HD^+ peak is due to the ion’s kinetic energy, it is possible to calculate an upper limit for the translational energy of the nascent HD from the velocity of the ions determined using equation 3.3.3.

The average width of an HD^+ TOF peak is 40 ns. This time will correspond to ions travelling both towards and away from the detector, hence it is necessary to divide 40

ns by 2 to give the correct value of $[t_{\text{expt}} - t_0]$, 20 ns. The charge, q , on the HD^+ is 1.602×10^{-19} C, the source field E_s , is $\frac{400}{0.03} = 1.33 \times 10^4 \text{ Vm}^{-2}$, and the mass of the HD is 4.98×10^{-27} kg. The source field is derived from the voltage applied to the middle plate of the TOFMS (400 V) divided by the distance between the middle plate and the repeller plate, 0.03 m. When the above values are substituted into equation 3.3.3 the velocity is found to be $8.57 \times 10^3 \text{ ms}^{-1}$. This can then be used to calculate a kinetic energy of ~ 1.1 eV for the nascent molecules, if the whole width of the HD^+ peak was due to the kinetic energy, which of course it is not. If the vibrationally excited HD^+ were to have a translational energy component along the axis of the TOFMS in excess of 1 eV, one would expect to observe a change in the widths and/or positions of the TOF REMPI peaks; so far this has not been the case. If it is assumed that the HD desorbs from the HOPG over a full range of angles relative to the surface normal, it is possible to put an approximate upper limit on the molecules translational energy of 1 eV.

In the calculation laid out above it is assumed that the entire width of the REMPI peaks is due to the energy spread of the nascent HD^+ . However, as mentioned previously, the instrument function also contributes to the width of the peak in the mass spectrum; this implies that the energy of the HD is likely to be less than 1 eV. Work carried out by Roser *et al*¹⁵ shows that the kinetic energy of hydrogen molecules desorbing from an amorphous water ice surface was very low, in the region of 3 meV. It would therefore appear that the upper limit of 1 eV determined here is, as expected, a considerable overestimate of the translational energy, but is the most robust estimate that can currently be derived from the apparatus.

3.3.2 Internal Energy and Energy flow into the Graphite

Having shown above that the translational energy for the newly formed HD has an upper limit of ~ 1 eV, there remains a minimum of ~ 3.5 eV of the 4.5 eV bonding energy that can be distributed between rotational and vibrational excitation and the HOPG surface. Using the standard spectroscopic equations for vibrational and rotational energies, it is possible to calculate how much energy will have gone into the vibrational and rotational modes as a function of ν'' and J'' . These equations are shown below:

$$E_v = \omega_e \left(v + \frac{1}{2} \right) - \omega_e x_e \left(v + \frac{1}{2} \right)^2 \quad 3.3.4$$

$$E_J = \left(\left(B_e - \alpha \left(v + \frac{1}{2} \right) \right) J(J+1) \right) - DJ^2(J+1)^2 \quad 3.3.5$$

where:

E_v is the energy of the vibrational state, vibrational quantum number v

E_J is the energy of the rotational state, rotational quantum number J

ω_e is the fundamental vibration wavenumber

x_e is the anharmonicity constant

B_e is the equilibrium value of the rotational constant B

α is a molecular constant

D is the centrifugal distortion coefficient

The data discussed above shows that HD is formed in the vibrational states $v'' = 1 - 7$ and over a range of rotational states, Table 8 below details how the remaining energy is split between the remaining modes of HD.

| HD State | | Energy Distribution % | | | |
|----------|-------|-----------------------|-----------|----------|---------|
| v'' | J'' | Translation | Vibration | Rotation | Surface |
| 1 | 4 | 22 | 15 | 2 | 60 |
| 2 | 4 | 22 | 25 | 2 | 51 |
| 3 | 6 | 22 | 34 | 4 | 40 |
| 4 | 6 | 22 | 42 | 4 | 31 |
| 5 | 6 | 22 | 50 | 4 | 24 |
| 6 | 4 | 22 | 58 | 2 | 18 |
| 7 | 3 | 22 | 65 | 1 | 12 |

Table 8. Table detailing how the 4.5 eV of binding energy released on the formation of HD is distributed through the various possible internal energy modes and into the HOPG surface. As discussed in the text above, the value for the translational energy is an upper limit and hence the value for the energy deposited into the surface is a lower limit.

Table 8 clearly shows that anything from 40% to almost 90% of the 4.5 eV binding energy can be distributed into internal excitation and translational energy, with as little as 12% of the energy flowing into the surface. However, since the value for the kinetic energy is an upper limit and it is possible that it is much lower than 1 eV, the values stated for the energy deposited into the surface are therefore lower limits. If the translational energy is considerably less than 1 eV, more energy could flow into the surface than is suggested here. Of course, if higher ro-vibrational states that are outside of our detection limit are populated by the nascent HD then the percentage of energy going into the surface will be negligible.

3.4 Discussion

There have been many theoretical studies carried out on the recombination of H atoms on a graphite surface: these have mainly concentrated on the Eley-Rideal mechanism. This focus is probably due to the ER mechanism being easier to model theoretically than the Langmuir-Hinshelwood mechanism, because only one H atom is bonded to the surface and that atom is localised. The theoretical studies of the ER mechanism suggest that there is a significant amount of ro-vibrational excitation of the nascent H₂. This is in agreement with the experimental results discussed above. Work by the Sidis group¹⁶ has shown that when an H atom impinges on one of two *para*-chemisorbed H atoms on a graphite surface the reaction is barrierless, something that has been observed experimentally by Hornekaer *et al.*¹⁷ The vibrational energy of the nascent H₂ was observed to reach a maximum at $v'' = 5$ and $v'' = 4$ was also significantly populated. These observations are in agreement with the experimental observations made in this thesis. However, comparing the data presented in this thesis with the ER reaction is not entirely appropriate as the H(D) atoms on the HOPG do not have enough energy to overcome the 0.2 eV barrier to chemisorption¹⁶ and bond to the graphite surface. With this in mind, it is believed that in diffuse and dense interstellar clouds H₂ formation is likely to be dominated by the LH mechanism. This assumption is also in agreement with the conditions found in the ISM, given the low temperatures and pressure the coverage of H atoms on the dust grains is likely to be less than 1 atom per grain. Therefore, it is unlikely that an H atom will directly impact on another H atom already adsorbed onto the dust grain, allowing the ER reaction to take place.

Work by Morisset *et al.*¹⁸ on the LH formation mechanism indicates that H₂ formed on a graphite surface should have considerable vibrational and rotational excitation where $v'' > 8$ with a distribution maximum at $v'' = 15$ and $J'' = 0$ upwards reaching a maximum at $J'' = 12$. This work indicates that the surface plays two roles in the LH mechanism: firstly, that it holds the H atoms close to the same plane, making a hard collision between the atoms more probable than in a 3D space; secondly, and even when the surface is not corrugated, energy transfer between the relative H-H motion and the H₂-surface is allowed. Morisset *et al.*¹⁸ carried out rough calculations of the reaction kinetics and observed that in the astrophysical environment the formation of H₂ is an efficient process, in that the time spent by two H atoms simultaneously physisorbed on the grain to meet and desorb as H₂ is much shorter than the time between two H-grain collisions. The work described in this thesis is in rough agreement with this theoretical data, as ro-vibrational excitation is observed.

Theoretical work by Kerkeni and Clary¹⁹ has been carried out on the LH mechanism and has shown non-negligible vibrational excitation with a maximum peaked at $v'' = 8$; however, high probabilities were also observed for $v'' = 4$ and 5. The experimental data discussed in this thesis shows lower ro-vibrational excitation than is calculated in the theoretical work of Morisset *et al.*¹⁸ and Kerkeni and Clary.¹⁹ This could be due to surface effects as the surface in the experiment will not be a perfect graphite surface and inevitably there will be some defects that could dominate the formation of the HD. In conjunction, the formation mechanism may not be purely Langmuir-Hinshelwood and there could be contributions from both Eley-Rideal and hot-atom mechanisms, all of which might affect the ro-vibrational distribution.

The majority of experimental work has been done using temperature programmed desorption (TPD). Zecho *et al.*²⁰ have used TPD in conjunction with electronic (ELS) and high-resolution electron-energy-loss (HREELS) spectroscopies to investigate the adsorption of H and D atoms on a HOPG surface. A deuterium atom beam with a temperature of 2000 K was used to chemisorb the D atoms to the graphite surface, which was held at 150 K. The layers of D atoms were then subjected to a beam of H atoms, also at 2000 K, and the HD produced was monitored using a quadrupole mass spectrometer. The results of these experiments confirmed the presence of the 0.2 eV barrier to chemisorption that had been observed theoretically.^{16,20} It is this barrier,

determined by Zecho *et al.*, that means for the experimental conditions described in this thesis, the H and D atoms do not have sufficient energy to chemisorb, hence they are physisorbed. For physisorbed atoms the Langmuir-Hinshelwood mechanism is the most likely reaction pathway on graphite terraces. Kinetic modelling of TPD data obtained following the recombination of low-energy H and D atoms on HOPG surfaces has suggested that a significant fraction of the nascent HD resides on the surface for a length of time at least comparable with the timescale of a TPD experiment.²¹ For this to occur a considerable amount of the HD bonding energy must flow into the surface. As is shown in Table 8 for $\nu'' = 4$, the highest populated state observed by the Cosmic Dust experiment, 31% of the 4.5 eV binding energy is distributed into the graphite surface. This calculation would suggest that the residence time for the HD on the HOPG is not negligible; however, in these higher vibrational states, the amount of energy flowing into the surface is possibly not significant enough to keep the HD on the surface for the duration of a TPD experiment.

Hornekaer *et al.*²² have also considered the chemisorption of D atoms on graphite surfaces, the experimental techniques of Scanning Tunnelling Microscopy (STM) and TPD were employed to image the D atom chemisorbed on the surface. The STM images showed that the deuterium on the graphite had two different characteristic structures, one with the D atoms in the *ortho* position, adjacent on the graphite ring and the other with the D atoms bonded to opposite carbon atoms (*para*) in a graphite hexagon. The experiments by this group showed that the recombination of the D atoms occurs through the *para* structure. More recent work by Hornekaer *et al.*¹⁷ confirmed that the *para* structure had the lowest energy recombination pathway for the formation of D₂. Laser assisted association adsorption (LAAD) experiments indicated that nascent H₂(D₂) desorbing normal to the HOPG surface have translational energy independent of the temperature increase induced by the laser. This observation indicates that for H₂(D₂) the translational energy comes only from the desorption energy. Hornekaer and co-workers found that the translational energy for the nascent molecules moving normal to the surface was approximately 1.3 eV, which left around 60% of the desorption energy to flow into the surface or to be converted into ro-vibrational excitation of the molecule. As discussed above, the upper limit for the kinetic energy of the HD formed in the Cosmic Dust experiment is 1 eV, less than that observed by Hornekaer *et al.*

A significant amount of work has been performed on the formation of H₂ (HD) on amorphous water ice surfaces. The Lemaire group²³ have focussed on the formation of D₂ on amorphous water ice at temperatures between 8 and 30 K. Under these conditions it was observed that the nascent D₂ was vibrationally excited ($v'' = 1 - 7$) and that the atomic recombination efficiency increased with the presence of D₂ molecules already adsorbed onto the surface. It was also found that recombination decreases with increasing temperature and is zero at 13 K. Other TPD work on amorphous water ice has shown that HD molecules thermalise in the surface pores. The HD signals were observed to be significantly reduced when non-porous water surfaces were irradiated with H and D atoms. These results indicate that on non-porous surfaces, such as HOPG, the nascent molecules are rapidly lost to the gas-phase during the dosing and before the heating cycle. The experiments in this thesis are “continuous” therefore; such promptly desorbed molecules are detected, so the detection of the nascent molecules from a non-porous surface in this work, but not in TPD, is not surprising.

3.5 Astronomical Implications

The aim of this work is to clarify the redistribution of the energy released upon the formation of H₂ in the interstellar medium. These experiments show that a significant proportion of the energy released upon the formation of the H – D bond is converted to ro-vibrational excitation of the nascent molecule. Earlier work has shown that the rotational distribution and fluxes of H₂ formed in $v'' = 1$ and 2 were very similar to those of HD, hence the extrapolation of the HD data presented above to the formation of H₂ is justified.

The chemical effects of the formation of H₂ in excited states have been modelled by Garrod *et al.*²⁴ In this model it is assumed that any H₂ formed on a dust grain will have enough energy to overcome reaction barriers and to form OH and CH⁺, which are important radicals in the interstellar medium.



It is possible that the above reactions may initiate a rich chemistry in the interstellar medium. A correlation between the column density of CH^+ and H_2 in highly rotationally excited states have been observed, hence these reactions are particularly pertinent to the inclusion of ro-vibrationally excited H_2 . The conclusions of Garrod *et al*²⁴ were that excited molecular hydrogen formed on dust grains in fact has little effect on these reactions in the ISM. The inclusion of ro-vibrationally excited H_2 in their models only resulted in a small increase in the formation of OH and CH^+ . In the case of diffuse regions where dissociative isothermal shocks (extreme conditions) were possible, the modellers observed a significant enhancement in the formation of OH and CH^+ ; however these enhancements were only short lived.

In the interstellar medium, ro-vibrational excitation of nascent H_2 is termed formation pumping and, in theory, the relaxation of such excited molecules can be observed. Excited ro-vibrational levels in the ground electronic state of H_2 can also be populated by a process called UV pumping. This process occurs when UV radiation excites H_2 to some higher vibronic state which then decays to levels in the X state *via* radiative processes.²⁵ Modelling studies by Tine *et al*²⁶ show that in diffuse clouds formation pumping is much less important than UV pumping which would be the dominant method for populating the lower ro-vibrational levels of H_2 . However, for all other more highly excited states, formation pumping has no other competitors. It was also observed that for dense clouds formation pumping will always be the dominant pumping process with a small amount of competition for the excitation of lower ro-vibrational states from fast electron impact excitation. Hence, observations of dense clouds could be carried out with the hope of observing highly excited H_2 that can only have occurred as a result of formation pumping.

Carrying out observations of formation pumping is a non-trivial procedure as often the formation pumping signals are masked by the stronger UV pumping signal, however there have been some successful observations attributed to formation pumping. Burton *et al*²⁷ have detected the H_2 6 – 4O(3) emission line in the infrared from the diffuse cloud Messier 17. Observationally, a marked difference in the spatial distribution is observed for the 6 – 4O(3) emission and 1 – 0S(1), 2 – 1S(1) and 1 – 0S(7) emission in Messier 17, suggesting that these emission processes are not the result of the same excitation mechanisms. Burton *et al* ascribe the 1 – 0S(1), 2 – 1S(1)

and 1 – 0S(7) lines to UV pumping because of their “topology” and line intensity ratios. The 6 – 4O(3) line has a different emission topology, hence Burton and co-workers²⁷ conclude that the 6 – 4O(3) line is not due to UV pumping and could be as a result of formation pumping. This observation may be the first direct astronomical observational evidence for formation pumping of H₂ into the $v'' = 6$ level. The data detailed in this thesis gives experimental evidence that under astronomically relevant conditions it is possible to form H₂(HD) on a dust grain surface in the $v'' = 6$ vibrational level, which gives further justification to Burton *et al* attributing the 6 – 4O(3) observation to formation pumping. Earlier work by Burton and co-workers²⁸ on the reflection nebula NGC 2023 gave rise to a detection of H₂ in the $v'' = 4$ state, which the authors felt was in too great a molecular abundance to be due to UV pumping alone. Burton *et al* postulated that the excess of molecules observed in $v'' = 4$ was evidence of formation pumping; however, signal-to-noise considerations meant that the observations were not definitive.

The majority of other astronomical observations of formation pumping have been more tentative. Wagenblast²⁹ considered UV absorption spectra of three nearly diffuse clouds and observed that the populations in the excited rotational levels of $v'' = 0$, $J'' = 5, 6$ and 7 could not be explained by UV or thermal excitation. Wagenblast made the assumption that molecular formation takes place in two adjacent rotational levels within a given vibrational state (one for ortho-H₂, or odd- J and the other for para-H₂, or even- J), then calculated the possible pairings that could account for the possible ratios of the three lines. The calculations showed that H₂ would need to be formed in a rotationally hot state, $J'' \geq 7$ but with a range of vibrational states up to $v'' = 11$. Wagenblast²⁹ concluded that the population of the $v'' = 0$, $J'' = 5, 6$ and 7 states must be due to collisions with other H atoms or by formation pumping of H₂ into high J states. Federman *et al*³⁰ explored the conclusions of Wagenblast further, with additional absorption measurements from the $v'' = 3$ level in the source ζ Oph, but did not find any fit to the data particularly satisfactory.

The starburst galaxy NGC 6240 was probed by Mouri and Taniguchi,³¹ the 1.5 – 2.5 μm spectrum was considered, as a number of H₂ lines are evident in this range. Given the relative strengths of the 1 – 0S(7) and S(9) lines compared with the 1- 0S(1) the group argued that formation pumping, *via* associative attachment of H and H⁻ to form

H₂ provided an important contribution to the line intensity. However, the data upon which these conclusions were based have low spectral resolution and suffer from blending. The data collected by Mouri and Taniguchi was fitted with a model that contained a number of components of the 1 – 0S(1) line intensity: formation (10%), fluorescence (20%) and thermal excitation (70%). In conjunction, with this the 6 – 4Q(1) line observed at 1.64 μm by Elston and Maloney³² in the NGC 6240 source is weak, in comparison with the 1 – 0S(1) line, having less than 10% of its intensity and has a low signal-to-noise ratio in the spectrum. Hence, the claims of a formation pumping signature observed by Mouri and Taniguchi³¹ need to be regarded with caution. Similarly, observations by Rosenthal *et al*³³ of the infrared emission from H₂ in the molecular cloud OMC-1 should be regarded with a degree of caution. Ro-vibrational emission lines of $\nu'' = 0 - 4$ were observed and Rosenthal and co-workers hypothesized that formation pumping of H₂ could be populating the higher energy states. However, this data was recorded with a limited spatial resolution, which means their spectra may integrate regions exposed to very different excitation sources.

The formation pumping of molecular hydrogen from dust grains has been searched for by Tine *et al*²⁶ by observing two dense clouds, L1498 and L1512 which are starless preprotostellar cores. These cores are dark and quiescent regions, different to the diffuse nebula observed by Burton *et al*,²⁷ so there is minimal UV and collisional pumping. Tine *et al* search for the series of infrared lines H₂ 1 – 0S(4) to S(9) in the 1.5 to 2 μm region of the spectrum but were unable to detect a clear signal. These lines are from high rotational levels ($J'' \geq 6$) which the data presented in this thesis suggests are not densely populated by formation pumping. Future searches may have greater success if the lines to be detected originate from the $\nu'' = 3$ or 4, $J'' = 0 - 6$ levels.

3.6 Summary

The formation of HD from H and D atoms on a HOPG surface held at 15 K has been studied and the results presented here. It has been observed that HD desorbs in a range of ro-vibrational states, $\nu'' = 3 - 7$, $J'' = 0 - 6$ although only the vibrational states of $\nu'' = 3, 4$ and 5 were detected in $J'' = 5$ and 6. The populations of the ro-vibrational states have been calculated and the average rotational temperatures determined. The most densely populated state was found to be $\nu'' = 4$ and the population then reduces

Chapter 3. Results of the Formation of HD on a Graphite Surface

significantly for the higher vibrational states. The data obtained for $v'' = 3 - 7$ has been scaled using the relevant Franck Condon Factors and plotted with the original data, also scaled using the FCFs, for $v'' = 1$ and 2. This plot provides a complete rovibrational distribution for HD formed on HOPG. These observations suggest that H_2 can be formed in excited states on graphite under astronomically relevant conditions and in fact the work of Burton *et al*²⁸ has proposed that the vibrational states observed here are populated by formation pumping in the interstellar medium.

3.7 References

- 1 K. D. Rinnen, M. A. Buntine, D. A. V. Kliner, R. N. Zare, and W. M. Huo, *Journal of Chemical Physics* **95**, 214 (1991).
- 2 G. Pozgainer, L. Windholz, and A. Winkler, *Measurement Science & Technology* **5**, 947 (1994).
- 3 U. Fantz and D. Wunderlich, Report No. 457, 2004.
- 4 S. C. Creighan, J. S. A. Perry, and S. D. Price, *Journal Of Chemical Physics* **124** (2006).
- 5 M. J. Murphy and A. Hodgson, *Surface Science* **368**, 55 (1996).
- 6 L. Schroter, R. David, and H. Zacharias, *Journal of Vacuum Science & Technology a-Vacuum Surfaces and Films* **9**, 1712 (1991).
- 7 A. Winkler, *Applied Physics A-Materials Science and Processing* **67**, 637 (1998).
- 8 H. Zacharias, *Applied Physics A-Materials Science & Processing* **47**, 37 (1988).
- 9 F. Islam, E. R. Latimer, and S. D. Price, *Journal Of Chemical Physics* **127**, 064701 (2007).
- 10 W. M. Huo, K. D. Rinnen, and R. N. Zare, *Journal Of Chemical Physics* **95**, 205 (1991).
- 11 E. R. Latimer, F. Islam, and S. D. Price, *Chemical Physics Letters* **455**, 174 (2008).
- 12 I. Dabrowski and G. Herzberg, *Canadian Journal of Physics* **54**, 525 (1976).
- 13 W. C. Wiley and I. H. McLaren, *Review of Scientific Instruments* **26**, 1150 (1955).
- 14 W. P. Hu, S. M. Harper, and S. D. Price, *Measurement Science & Technology* **13**, 1512 (2002).
- 15 J. E. Roser, S. Swords, G. Vidali, G. Manico, and V. Pirronello, *Astrophysical Journal* **596**, L55 (2003).
- 16 L. Jeloica and V. Sidis, *Chemical Physics Letters* **300**, 157 (1999).
- 17 L. Hornekaer, Z. Sljivancanin, W. Xu, R. Otero, E. Rauls, I. Stensgaard, E. Laegsgaard, B. Hammer, and F. Besenbacher, *Physical Review Letters* **96** (2006).
- 18 S. Morisset, F. Aguillon, M. Sizun, and V. Sidis, *Physical Chemistry Chemical Physics* **5**, 506 (2003).
- 19 B. Kerkeni and D. C. Clary, *Chemical Physics Letters* **438**, 1 (2007).
- 20 T. Zecho, A. Guttler, X. W. Sha, B. Jackson, and J. Kupperts, *Journal of Chemical Physics* **117**, 8486 (2002).
- 21 N. Katz, I. Furman, O. Biham, V. Pirronello, and G. Vidali, *Astrophysical Journal* **522**, 305 (1999).
- 22 L. Hornekaer, E. Rauls, W. Xu, Z. Sljivancanin, R. Otero, I. Stensgaard, E. Laegsgaard, B. Hammer, and F. Besenbacher, *Physical Review Letters* **97** (2006).
- 23 L. Amiaud, F. Dulieu, J. H. Fillion, A. Momeni, and J. L. Lemaire, *Journal of Chemical Physics* **127** (2007).
- 24 R. T. Garrod, J. M. C. Rawlings, and D. A. Williams, *Astrophysics and Space Science* **286**, 487 (2003).
- 25 J. H. Black and A. Dalgarno, *Astrophysical Journal* **203**, 132 (1976).
- 26 S. Tine, D. A. Williams, D. C. Clary, A. J. Farebrother, A. J. Fisher, A. Meijer, J. M. C. Rawlings, and C. J. Davis, *Astrophysics And Space Science* **288**, 377 (2003).

Chapter 3. Results of the Formation of HD on a Graphite Surface

- ²⁷ M. G. Burton, D. Londish, and P. Brand, *Monthly Notices Of The Royal Astronomical Society* **333**, 721 (2002).
- ²⁸ M. G. Burton, M. Bulmer, A. Moorhouse, T. R. Geballe, and P. Brand, *Monthly Notices Of The Royal Astronomical Society* **257**, P1 (1992).
- ²⁹ R. Wagenblast, *Monthly Notices Of The Royal Astronomical Society* **259**, 155 (1992).
- ³⁰ S. R. Federman, J. A. Cardelli, E. F. Vandishoeck, D. L. Lambert, and J. H. Black, *Astrophysical Journal* **445**, 325 (1995).
- ³¹ H. Mouri and Y. Taniguchi, *Astrophysical Journal* **449**, 134 (1995).
- ³² R. Elston and P. Maloney, *Astrophysical Journal* **357**, 91 (1990).
- ³³ D. Rosenthal, F. Bertoldi, and S. Drapatz, *Astronomy and Astrophysics* **356**, 705 (2000).

Chapter 4

Commissioning of Cold Atom Jets and Consequent Experimental Shortcomings

Overview

In this chapter, the changes made to the experiment to cool the H and D atom beams to a more astrophysically relevant temperature will be described. At this lower temperature the formation of HD on a HOPG surface was observed; however, once the data was analysed by the method described above, it became apparent that there were problems with the new experiments. These problems will be discussed and the various, ongoing, steps taken to solve the problems will be described. It is important to note that the results discussed Chapter 3 were not affected by any of the issues described here.

4.1 Cooling of the Atom Beams

As discussed in Chapter 2 the H and D atoms are produced in two separate microwave dissociation cells and then the atoms are allowed to pass through PTFE tubes until they reach the HOPG surface. The atoms are at room temperature and it had been thought that when the atoms impinge on the surface they might thermalise with the 15 K graphite and so will also have a temperature of 15 K. However, this assumption has not been proven, so it was deemed necessary to alter the temperature of the atom beams and see if there was any change in the resulting ro-vibrational population. The lower gas temperatures are more astronomically relevant, as in the diffuse clouds in the ISM the gas is at a temperature of approximately 100 K.

Initially it was decided that a simple cooling method would be employed to allow preliminary data to be taken, then if any changes were observed, a more robust set-up would be installed. A common way of cooling H atoms is by passing them over a cooled aluminium surface. Generally, aluminium surfaces catalyse the recombination of hydrogen atoms; however, work by Toennies, Welz and Wolf¹ showed that when H atoms are produced in a radio frequency discharge, the atoms can be cooled to ~90 K by passing the gas through channels in an aluminium block that is cooled with liquid nitrogen. Toennies *et al* tested various materials including Pyrex, boron nitride and

Chapter 4. Commissioning of Cold Atom Jets and Consequent Experimental Shortcomings

copper but found that the best results came from the aluminium.¹ The success of the aluminium in cooling, and the minimal H atom recombination, was attributed to the formation of a thin aluminium oxide layer efficiently cooled by the metal substrate.² In the Cosmic Dust experiment it was not possible to use liquid nitrogen to cool down an aluminium block, so a set-up was devised that allowed a piece of aluminium to be attached to the radiation shield of the coldhead. The radiation shield is designed to reduce thermal losses from the coldhead and target. It is attached to the first stage of the coldhead and hence is at a low temperature (~ 40 K). Adding an Al block to the edge of the radiation shield and ensuring good thermal contact between the block and radiation shield would result in the block being cooled to a similar temperature. Mounting the block on the radiation shield had other advantages as the proximity of the block to the target would mean that the H and D atoms could be easily directed to directly impinge on the HOPG, as they had done previously. A schematic of the Al block is shown below in Figure 4.1.1.

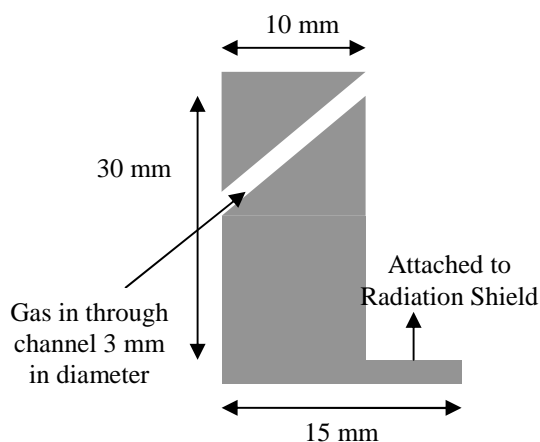


Figure 4.1.1 A cut through of the Al block attached to the radiation shield to cool the H and D atoms. The block has two channels cut into it, similar to the one shown above, one for the H atoms and another for the D atoms.

Figure 4.1.1 is a section of the aluminium block that is attached to the radiation shield. There are two channels cut into the block 7 mm apart. The PTFE atom transport tubes are allowed to enter into the mouth of the channel, just far enough that they cannot be easily

Chapter 4. Commissioning of Cold Atom Jets and Consequent Experimental Shortcomings

dislodged, then the gas flows through the remainder of the channel and is cooled. A flat was skimmed onto the radiation shield so that there would be good thermal contact between the Al block and the shield; gold was placed between the aluminium and the radiation shield to allow good thermal conductivity (Figure 4.1.2).

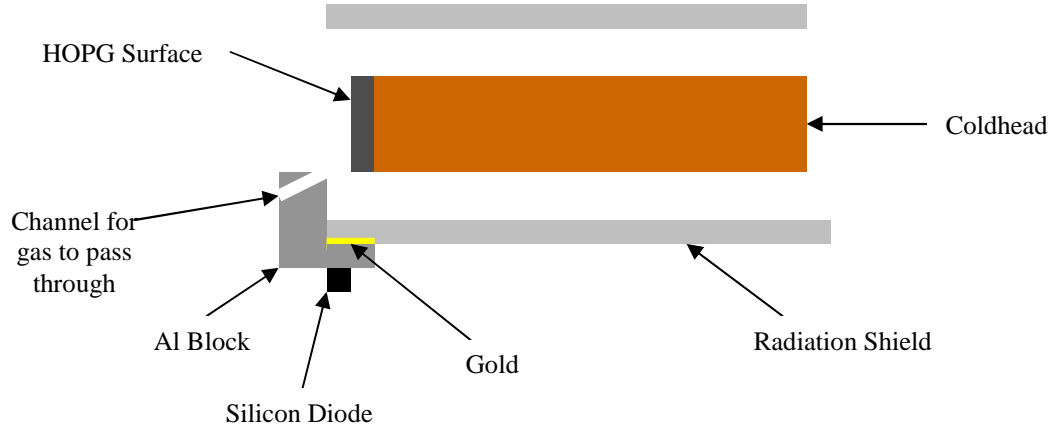


Figure 4.1.2 Schematic to show how the aluminium cooling block is attached to the radiation shield.

The distance between the top of the aluminium block and the centre of the HOPG target is approximately 13.5 mm, so the gas leaves the Al block very close to the target which will mean that only a small proportion of the atoms will be lost to the surrounding chamber. A silicon diode is attached to the aluminium to measure the temperature. When the graphite surface reaches a temperature of 15 K the Al block is at a temperature of between 45–50 K. This temperature could be reduced by taking further steps to improve the thermal contact between the Al block and the radiation shield; however, for preliminary experiments 45-50 K was a sufficient change from room temperature to observe any differences in the ro-vibrational distribution. The work of Walraven and Silvera³ showed that the atoms should be thermalised with the walls of Al channels within a couple of collisions. Their work also showed that the average number of collisions with the walls (N_c) is given by:

$$N_c = \frac{3}{8} \left(\frac{l}{r} \right)^2 \quad 4.1.1$$

where l is the length and r is the radius of the channel. For the case of the channel cut the aluminium block used in these experiments $l = 18$ mm and $r = 3$ mm and hence, $N_c = 13.5$.

4.2 Results

The formation of HD from the cold atoms in the vibrational states $v'' = 1 - 7$ was probed, using the same experimental technique described in Chapter 2. The data was analysed in the same way as the data for the warm atoms and the Franck Condon factors were used to put the distributions onto a relative scale. The data for $v'' = 3 - 7$ was collected first as the laser was set to the frequency doubling regime. Initial observations indicated that $v'' = 3$ was now more populated than $v'' = 4$ and the higher vibrational states had even lower populations than had been observed with the warm atoms, with only $v'' = 7, J'' = 1$ and 2 being populated. The laser was then changed to the frequency tripling regime and the data for $v'' = 1$ and 2 collected. These vibrational states had even higher populations than $v'' = 3$, with a population maximum at $v'' = 1$ (Figure 4.2.1).

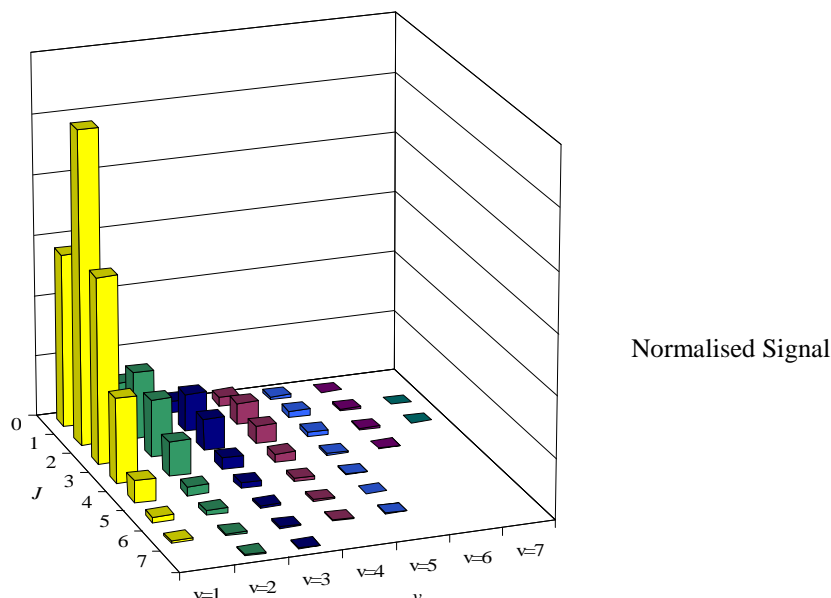


Figure 4.2.1 Derived relative ro-vibrational populations of HD formed on a HOPG surface at 15 K in the vibrational states $v'' = 1 - 7$. The H and D atoms were cooled to 45 K before reaching the surface. The ro-vibrational states are placed on a relative scale, as describe in Chapter 3.

Chapter 4. Commissioning of Cold Atom Jets and Consequent Experimental Shortcomings

As a result of probing the higher vibrational states first, it was not clear until Figure 4.2.1 was constructed that the ro-vibrational distribution of HD formed on graphite from cold H and D atoms, was in fact a thermal distribution of the vibrational states and upon fitting the data to a Boltzmann distribution an r^2 value of 0.95 was obtained. Given that the data for the room temperature atoms was definitely not a thermal distribution the cold atom results suggested there was something else influencing the data. The first test carried out to see if there were any problems with the experiment was to turn off one of the atom sources and to run a scan to see if there was any HD being formed on the surface. It had previously always been the case that with only one source on, either the H or D source, there was no HD produced (Figure 4.2.2). Such checks that the nascent HD was a result of the interaction of the H beam with the D beam were carried out regularly during the experiments reported in Chapter 3.

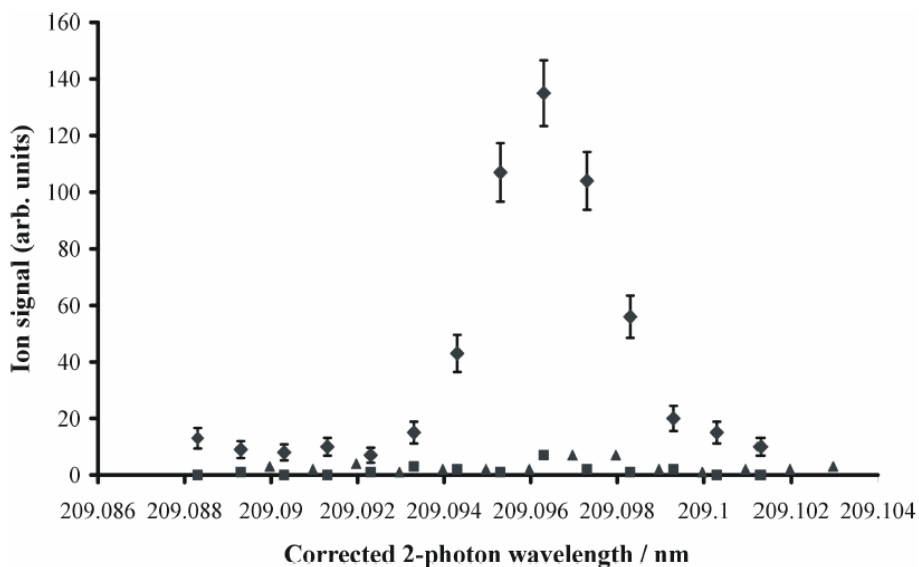


Figure 4.2.2 REMPI signal for the HD transition $E,F \ ^1\Sigma_g^+ (v' = 0, J' = 1) - X \ ^1\Sigma_g^+ (v'' = 1, J'' = 1)$. HD was formed on a HOPG surface at 298 K and the H and D atoms at room temperature. The \blacklozenge symbol indicates when both atom sources were on, the \blacksquare the H source was on but the D source was off and the \blacktriangle the D source was on and the H source was off.

When this test was performed after the cold atom data was collected, the results were not as expected. With the deuterium source off, no HD was detected; however, with the D source on, there was a considerable HD REMPI signal, as is shown in Figure 4.2.3.

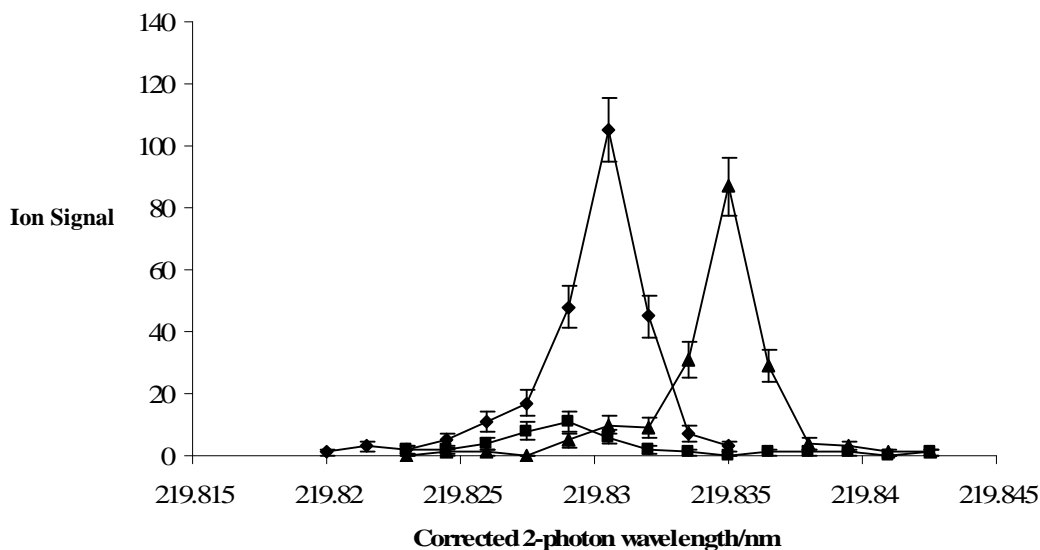


Figure 4.2.3 REMPI signal for the HD transition $E,F \ ^1\Sigma_g^+ (\nu' = 0, J' = 1) - X \ ^1\Sigma_g^+ (\nu'' = 3, J'' = 1)$. HD was formed on a HOPG surface at 298 K. The \blacklozenge symbol indicates when both atom sources were on, the \blacksquare the H source was on but the D source was off and the \blacktriangle the D source was on and the H source was off.

The two peaks shown in Figure 4.2.3 are from the same ν'' , J'' transition, but are at slightly different wavelength. This is due to a slight drift in the laser calibration. Figure 4.2.3 clearly shows that when the H atom source was turned off there was still a considerable HD REMPI signal, almost as large as the signal observed when both sources were on; however, the HD signal was negligible when the H source was on and the D off. This result indicated that there could be a contamination problem with the D source. However, H_2 is the predominant background gas in the target chamber, as it is harder to pump away as efficiently as any heavier atoms or molecules. There was also the possibility that the HD was forming on surfaces in the target chamber. It was vitally important that the two possible causes of this rogue HD signal were disentangled before taking any steps to fix the problem.

4.3 Problem Solving

The decision was made to tackle the possibility that the deuterium microwave dissociation cell had become contaminated. At first glance the old Pyrex cell had been

Chapter 4. Commissioning of Cold Atom Jets and Consequent Experimental Shortcomings

heavily etched by the plasma and this could have lead to the cell becoming porous. Here, the cell was replaced, but it was not possible to passivate the Pyrex in phosphoric acid before it was placed into the vacuum chamber. However, at the time, this was not thought to be a particular problem as over time the H atoms, on the terminal OH groups on the glass that would normally be removed by the phosphoric acid, would be replaced with D atoms in the plasma. Therefore, any HD signal should reduce over the period of a few weeks before disappearing completely. However, surprisingly, this did not happen and the HD REMPI signal, with just the D source on, remained just as strong.

Attention then shifted to the possibility that the HD was being formed in the target chamber. Obviously HD could be formed on the HOPG surface, so the target and coldhead were removed from the chamber to eliminate one possible source for HD formation. The PTFE atom transport tubes were moved so it was possible to directly ionise the atoms and this had no effect on the HD signal. With the coldhead and graphite taken out of the equation there were very few surfaces left to consider: the repeller plate of the time-of-flight or the walls of the chamber. The target chamber was thoroughly cleaned to remove any species that could be contributing to the HD signal; this did not seem to have an influence on the problem. However, when the chamber was opened again after this cleaning, a strong smell of oil was noticed. The backing lines between the rotary pump and the turbo pump were checked for any signs of oil and cleaned; the turbo pump was then removed to check for any oil present. There was found to be a small reservoir of oil at the bottom of the turbo; this could have collected there after an overnight power outage which had occurred recently. There was a similar problem with the turbo pump on the source chamber, so both pumps were removed and returned to the manufacturers for cleaning. It is believed that oil became a problem while attempts were being made to fix the HD contamination problem; during this period the chamber was regularly being brought up to atmospheric pressure. The venting procedure was set-up so that nitrogen was blown into the turbo pumps from the bottom, below the blades, where the oil was located. The regular venting meant that the oil could have become vaporised and carried up into the chamber. Steps have now been taken to ensure that this cannot happen again and a valve has now been fitted to the target chamber so one can vent

Chapter 4. Commissioning of Cold Atom Jets and Consequent Experimental Shortcomings

directly into the chamber rather than through the turbo pump. Once the cleaned turbo pumps were returned, the target chamber was cleaned. However, none of this lengthy procedure had any impact on the HD signal.

Despite the cleaned target chamber there still remained the possibility that the HD was being formed on the surfaces of the vacuum chamber. To be able to definitively tell whether the problem originated in the D source or in the target chamber, an aluminium block with a channel through the middle was placed into the gas line from the D source to the target chamber (Figure 4.31). The aluminium was kept room temperature, so any atoms passing through the channel would recombine on the Al surface; however, any molecules such as HD would pass through into the target chamber. So if a HD REMPI signal was still observed then the problem was in the D source, whereas if there was no HD signal then the problem was in the target chamber, as all the D atoms would have recombined to D_2 and would not be able to react on surfaces in the target chamber. An HD signal was observed, so this was a clear indication that the problem was located in or around the D source.

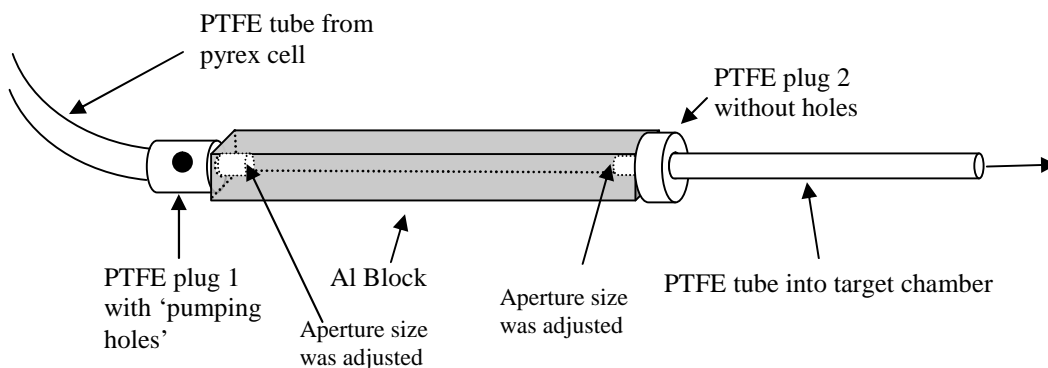


Figure 4.3.1 Diagram to show the set-up of the PTFE tubes in and out of the aluminium block placed in the D gas line.

Now, the area where the problem had been identified to be the cell, it was necessary to systematically work through all the possible causes of the contamination. Given that the Pyrex cell had already been changed, it was assumed that was unlikely to be the issue. The deuterium gas cylinder was almost empty and, although unlikely to be the root of the

Chapter 4. Commissioning of Cold Atom Jets and Consequent Experimental Shortcomings

problem, the cylinder was replaced in an attempt to eliminate another possible cause. The next step was to systematically leak test all of the joints in the gas line running up to the deuterium dissociation cell. Any joins in the gas line were made with Swagelok fittings and it is possible that over time these could have loosened; air leaking in would provide a good source of H atoms. A few minor leaks were discovered and fixed, although this did not have any significant impact on the HD signal coming from the D source. During this period it was also observed that the background signal appearing on the mass spectrum was higher than usual (Figure 4.3.2). Previously, high background signal problems had been associated with a high level of scattered laser light in the target chamber. Although since the introduction of the Brewster's angle window, scattered light had become less of an issue. Scattered light problems could normally be solved by moving the mirrors that reflected the UV light into the chamber, so the beam followed a better path through the target chamber. However, on this occasion moving the path of the light had no impact on the background level.

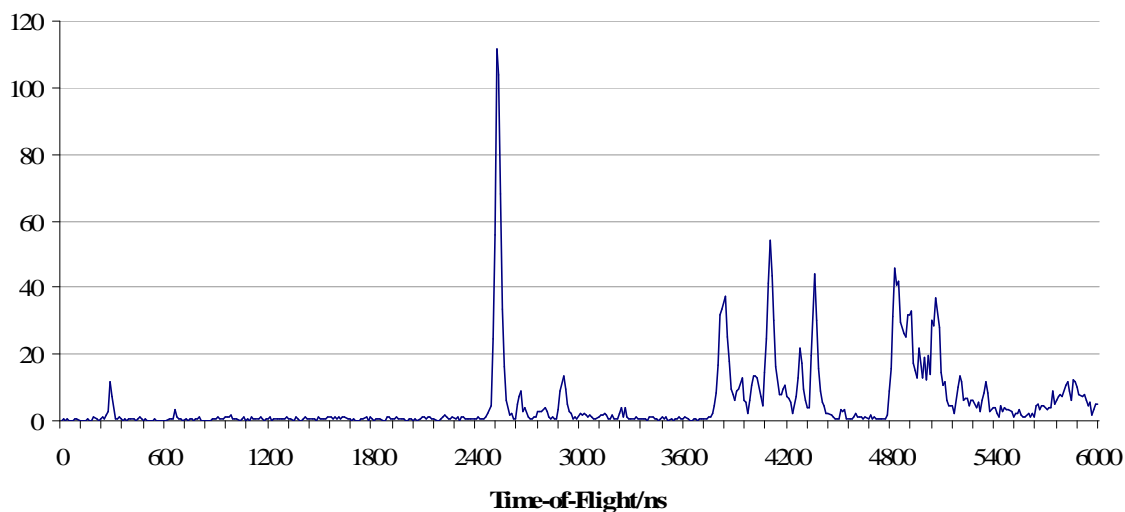


Figure 4.3.2 Mass spectrum showing the high background levels observed.

Given that the high background remained, even after careful reduction of the scattered light levels, suggested that the high mass molecules were being transported into the target chamber through the gas lines, the implication was that either the new deuterium cylinder was contaminated or there was still a leak in the lines leading up to the D source. One

Chapter 4. Commissioning of Cold Atom Jets and Consequent Experimental Shortcomings

way to combat this problem was to freeze out any contaminants that might be present in the D_2 gas line. A loop of copper tube was introduced into the gas line and this was placed in a dewar of liquid nitrogen; the gas lines were pumped out fully to remove any air that might have got in while fitting the copper; the D_2 was allowed into the line and then a mass spectrum was taken. Figure 4.3.3 shows one mass spectrum taken with the copper tubing cold with the D_2 gas flowing but without the microwaves on, and another mass spectrum under the same conditions but with the microwaves turned on.

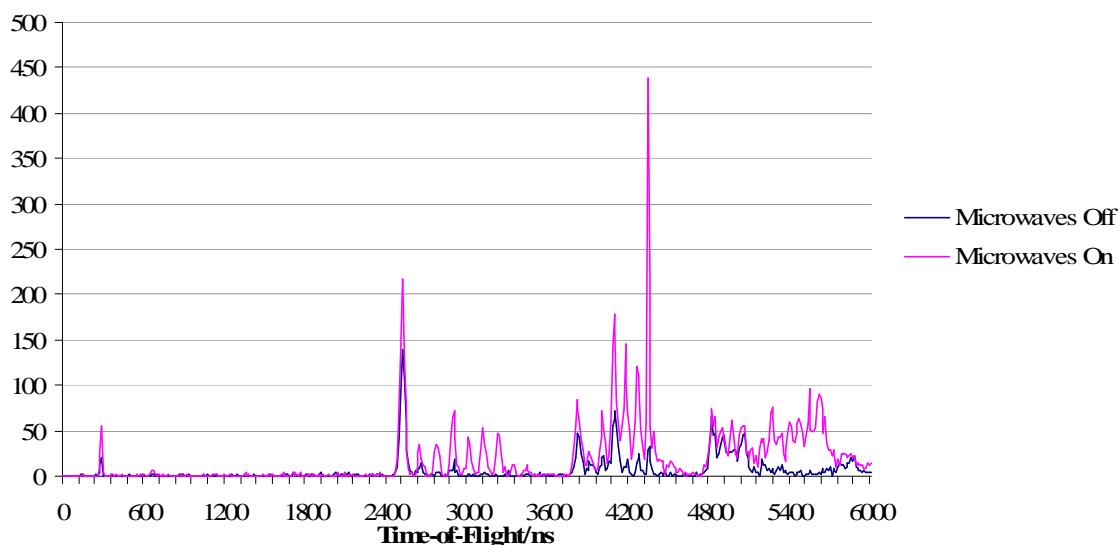


Figure 4.3.3 Background mass spectra taken with the D_2 gas line cooled in liquid nitrogen, one spectrum taken with the microwave source on and the other with the source off but the gas still flowing.

The mass spectra taken with the copper cooled down indicated that simply cooling down the gas lines was not enough to remove any contaminants and that turning the microwaves on had a significant impact on the background. The background, being worse with the microwaves on; suggested that there were species of high mass or inert species such as N_2 , getting into the gas line that were not removed by the cooling; when these species were broken apart by the microwaves they may have become more reactive and formed some of the molecules observed in the mass spectrum. The most likely origin of such molecules would be air, which suggested that there was still a leak in the gas line. In an attempt to narrow down the location of the leak the decision was made to persevere with the cold trap. In addition to the cooling a zeolite was added to the trap to sieve out any contaminants that were not removed by cooling alone.

Chapter 4. Commissioning of Cold Atom Jets and Consequent Experimental Shortcomings

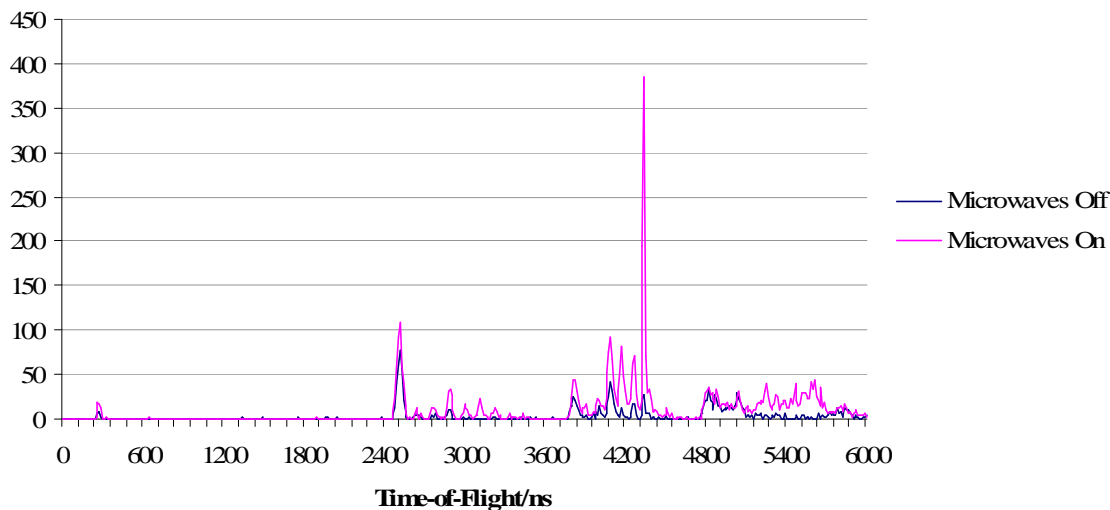


Figure 4.3.4 Background mass spectra taken with the D_2 gas line cooled and the gas allowed to pass through a zeolite before entering the dissociation cell. One spectrum was taken with the microwave source on and the other taken with the microwaves off but the D_2 still flowing.

If the zeolite and cold trap was effective and the background still remained high, that suggested that the leak was most likely to be after the trap; whereas if the background was reduced, then the problem was before the trap. Figure 4.3.4 shows the mass spectra that were obtained from this test. Again the background is significantly higher with the microwaves on; however, overall there are significantly fewer counts. Without the zeolite in place there were 3097 counts in the mass spectrum in 100 s, with the microwaves off and 8485 counts in 100 s with the microwaves on; but with the zeolite there were 1577 counts and 3966 counts in the mass spectrum respectively. This implied that the leak was before the trap. One leak was found across the on/off valve to the cylinder; however, fixing this leak did not have a significant impact on the background. The gas line after the trap and before the dissociation cell was tested for leaks. Again a few small leaks were found and the relevant Swagelok fittings were tightened. Unfortunately, after all of these adjustments there remained a significant HD REMPI signal. The Swagelok fittings had been tightened to a point where it was difficult to tighten them any more and yet the Pirani gauge on the D source and the ion gauge in the source chamber indicated that the pressure was fluctuating whenever a leak test was carried out. It eventually became

Chapter 4. Commissioning of Cold Atom Jets and Consequent Experimental Shortcomings

apparent that there was a problem with the needle valve that allows a small flow of deuterium into the Pyrex cell. Initially, it was thought that the needle valve was leaking. However, after further tests it was observed that the fluctuating pressure in the cell only occurred when there was a flow of gas. It was concluded that the methanol used to test for leaks would, when sprayed onto the needle valve, cooled down the valve causing it to contract, resulting in a drop in pressure in the cell. As the methanol evaporated the valve would warm back up again and expand, meaning that the pressure in the cell would rise again; this had been interpreted as a leak. Some of the Swagelok fittings, where the most significant leaks had been found, were located above the needle valve, so it was possible that the methanol had dripped onto the needle valve, causing a pressure change and allowing one to believe that there was a leak on the Swagelok fitting, when there was not.

The HD signal from the D source remained, with no obvious clues as to from where it originated. The decision was made to swap the gas cylinders round, so the hydrogen would now be running through the problematic D source and deuterium through the H source. As with the previous tests the D source was turned on and the H remained off; unlike the previous scans no HD REMPI signal was observed. However, when the H source was lit with the D source off there was a HD signal. The HD signal coming from the H source did reduce over time but did not disappear completely. This result suggested that when the Pyrex dissociation cells are not passivated in phosphoric acid before use, the dangling OH bonds on the silicate do not become quickly deuterated, or hydrogenated, when the gas cylinders were swapped round, hence causing a contamination problem. The H source was replaced by a new cell which had been in phosphoric acid and the rogue HD signal finally disappeared.

4.4 Conclusion

The contamination of the deuterium source was a two-fold problem. Firstly, how the contamination came about and, secondly, why it continued for so long? It is now thought that the initial problem, of HD coming solely from the D source, was as a result of several tiny leaks in the gas line behind the D source; these leaks were fixed during the process described above. Why the contamination did not disappear after these leaks were

Chapter 4. Commissioning of Cold Atom Jets and Consequent Experimental Shortcomings

fixed, was due to the new Pyrex cell that was placed in the source chamber, before it was passivated in phosphoric acid. When the gas cylinders were swapped round it became obvious that a cell which had been in the acid could be used for either gas, without any risk of contamination. However, the cell that had not spent any time in the acid was a rich source of H atoms and, although some of the OH dangling bonds did become deuterated, this process did not occur as rapidly as was originally assumed. It is now apparent that it is vitally important to passivate the Pyrex cells before use.

4.5 References

- ¹ J. P. Toennies, W. Welz, and G. Wolf, *Journal of Chemical Physics* 71 (2), 614 (1979).
- ² H. a. W. Wise, B.J., *Advances in Atomic and Molecular Physics*. (Academic New York Press, 1967).
- ³ J. T. M. Walraven and I. F. Silvera, *Review of Scientific Instruments* 53 (8), 1167 (1982).

Chapter 5

Studies of the Dissociation and Energetics of Singly and Doubly Ionised OCS

Overview

In this chapter the electron ionisation of OCS will be investigated using pulsed time-of-flight mass spectrometry in conjunction with a 2-D coincidence technique. The experimental set-up allows fragment ions formed by dissociative single, double and triple ionisation to be detected and quantified. The relative partial ionisation cross sections (PICS) and precursor specific relative (PICS) are derived as well as information on OCS²⁺.

5.1 Introduction

As discussed in Chapter 1 carbonyl sulphide (OCS) is an important molecule that contributes to the global atmospheric sulphur cycle. OCS exists in the atmospheres of other planets including Venus and Jupiter and has been observed in dense molecular clouds in the interstellar medium. The dissociation of OCS ions has been extensively studied following photoionisation. Masouka *et al* studied the dissociation of OCS using synchrotron radiation¹ and Eland *et al* investigated the dynamics of OCS dissociation using atomic discharge lamps.² In comparison to photoionisation, the amount of work on the electron impact ionisation of OCS is very limited. The group of Wang and Vidal³ employed covariance mapping techniques to investigate the dissociation of OCS after single, double and triple ionisation, using electron impact at 200 eV. Wang and Vidal measured the absolute cross-sections for the ion pair and ion triple dissociation channels and derived the cross-sections for the dissociation pathways that only have one ionic product. The results presented in this thesis are compared to results of Wang and Vidal later in this chapter.

5.2 Experimental

The experiments carried out to evaluate the ionisation cross-sections of OCS were performed on a Wiley-McClaren style time-of-flight mass spectrometer,⁴ the set-up of which is described in detail in Section 2.5. The TOFMS is again housed in a vacuum chamber which is pumped by a diffusion pump, and a turbomolecular pump located near to the detector to maintain a low gas pressure close to the Micro Channel Plates (MCPs) during data collection. The gas inlet system is held at low pressure so that the sample gas can rapidly enter the TOFMS before any sample deposition can occur; the flow of gas is carefully controlled by a needle valve. The pressure, which is measured using an ion gauge, is typically 1×10^{-6} Torr during the data collection. The ionisation of the sample gas occurs following the interaction of the gas with a pulsed beam of electrons in the source region of the TOFMS. Both the gas and the electrons are transported to the source region *via* hypodermic needles, which are mounted perpendicular to each other and both are perpendicular to the axis of the time-of-flight. The intersection between the pulsed electron beam and the target gas is the point of ionisation and this is designed to occur at the centre of the source region of the TOFMS, Figure 5.1.1.

The experiment is controlled by a 50 kHz pulse generator that operates the pulsing of the electron gun, repeller plate of the TOF and produces a start signal to begin each timing cycle of the data collection electronics. The electron gun is made up of a thoriated iridium filament, a stainless steel base plate, electron beam optics and needle which allows access to the source region of the TOF.⁵ When there is no trigger pulse a negative potential is applied to the base plate to prevent electrons from flowing from the filament to the mouth of the needle. The arrival of a trigger pulse results in a pulsed voltage being applied to the base plate, allowing a flow of a electrons from the filament to the source region. The pulses from the electron gun are approximately 30 ns long, at a repetition rate of 50 kHz. Electrons in the energy range 30 – 200 eV can be quenched and the energy resolution of the beam is estimated to be 0.5 eV at full width half maximum (FWHM).

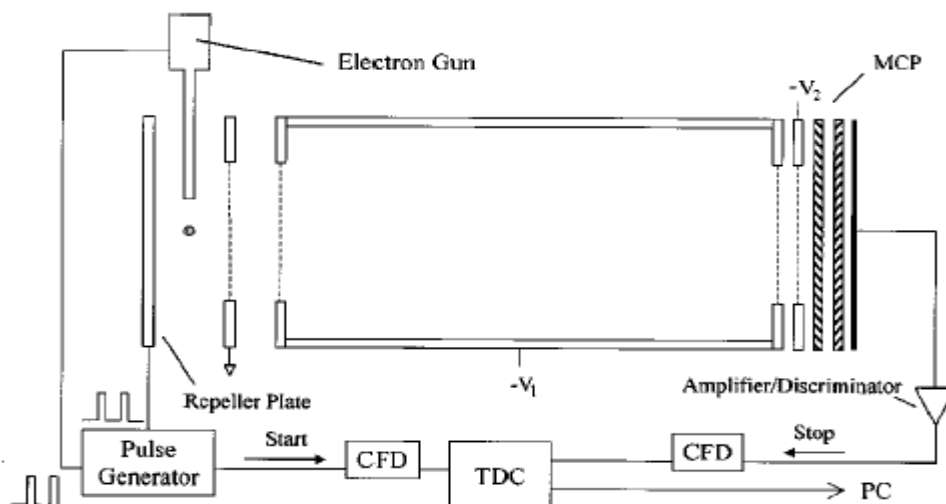


Figure 5.2.1 Schematic diagram of the experimental set-up.

Once the target gas has been ionised, the repeller plate is pulsed from 0 to +400 V to extract all of the positive ions from the source region into the acceleration region; the electric field in the acceleration region is formed by a grid, held at a negative potential, placed at the entrance to the drift tube. The accelerated ions pass through the field-free drift tube before hitting the MCP detector. 350 ns after the extraction voltage is applied to the repeller plate a 'start' signal is sent from the pulse generator to the time-to-digital converter (TDC) *via* a constant fraction discriminator (CFD). The CFD here is solely used to convert a TTL pulse to an ECL pulse. The MCP detector employed in this experiment is the same as the set-up described in detail in Chapter 2. The TDC used here is capable of receiving up to 32 'stops' from the detector within a 5000 ns time window, during which the arrival times of ions as single detections, ion pairs and ion triples are stored separately as single events. The data is collected in 512 kb memory module *via* a fast encoding and readout analogue-to-digital conversion system interface and is then transferred to a PC. This methodology allows normal time-of-flight mass spectra and ion coincidence spectra to be recorded in parallel.

5.2.1 Ion Discrimination Effects

To be able to extract quantitative data from the mass spectra obtained, one must ensure that the TOFMS is able to detect all ions with equal efficiency, regardless of their mass or initial kinetic energy. Work by Bruce and Bonham⁶ found that when measuring the relative intensities of Ar^+ and Ar^{2+} after the electron impact ionisation of Ar that subtle changes in the experimental parameters could cause mass discrimination effects. The experimental parameters that have the most significant impact are: the background gas pressure, the ion impact energy on the detector and the threshold settings on the CFD. Specifically the ratio of $\text{Ar}^{2+}/\text{Ar}^+$ was found to increase slowly as the background gas pressure increased above 5×10^{-6} Torr. Similar experiments to those performed by Bruce and Bonham were carried out on the experiment described here, to find the optimum settings for discrimination free detection. It is under these conditions that all experiments have been performed, Table 1.

| Parameter | Setting |
|--------------------------------|---------------------------|
| Gas Pressure | $< 1 \times 10^{-6}$ Torr |
| Repeller Plate Pulse Frequency | 50 kHz |
| Repeller Plate 'Off' | 0 V |
| Repeller Plate 'On' | +400 V |
| Extractor Grid | 0 V |
| Drift Tube | -1600 V |
| MCP Front | -2050 V |
| MCP Back | +250 V |
| Length of Source Region | 10 mm |
| Length of Acceleration Region | 18 mm |
| Length of Drift Tube | 195 mm |
| Diameter of Detector | 40 mm |

Table 1 Optimum experimental parameters.

5.2.2 Energetic Ion Collection

When measuring PICS it is essential that the apparatus is able to efficiently collect translationally energetic ions.⁷ This is of particular importance when investigating fragmentation processes involving multiple ionisation, as such events often generate ions with large kinetic energy releases.^{8,9} The apparatus described in this chapter has been designed to collect all ions that are formed with a kinetic energy less than 10.6 eV. It has been assumed that all ionisation occurs in the centre of the source region, so given that the detector has a diameter of 40 mm, the ions can travel 20 mm perpendicular TOF axis during their flight time and still be detected. The maximum detectable velocity perpendicular to the flight axis, v_y , is given by:

$$\frac{r_{\text{det}}}{t_{\text{tof}}} = v_y \quad 5.2.1$$

where r_{det} is the radius of the detector and t_{tof} is the flight time of an ion of mass m . This velocity v_y can be related to the translational kinetic energy that an ion may possess, E_y , perpendicular to the flight axis and still be detected:

$$v_y = \left(\frac{2E_y}{m} \right)^{\frac{1}{2}} \quad 5.2.2$$

hence:

$$E_{y\text{max}} = \left(\frac{r_{\text{det}}}{t_{\text{tof}}} \right)^2 \frac{m}{2} \quad 5.2.3$$

Equation 5.2.3 is independent of the mass of the ion given that: $t_{\text{tof}} \propto \sqrt{m}$. When using the flight time for the Ar^+ ion (2805 ns) the value of $E_y < 10.6$ eV is obtained. Work by Curtis and Eland⁹ showed that the total kinetic energy release (KER) from the dissociation of small molecular dications, to be typically significantly less than 9 eV,

hence the experimental conditions described in this chapter are ideal to collect all ions that are formed by multiple ionisation.

5.3 Data Analysis

This section describes the analysis procedures used to process the data obtained by the pulsed time-of-flight mass spectrometer and the 2-D coincidence technique discussed above.

5.3.1 Singles Spectra

A list of ion arrival times for each pulse of the repeller plate is collected by the TDC. Events, where only one ion is collected, are termed ‘singles’ and their arrival times are collated to produce a singles time-of-flight spectrum (Figure 5.3.1).

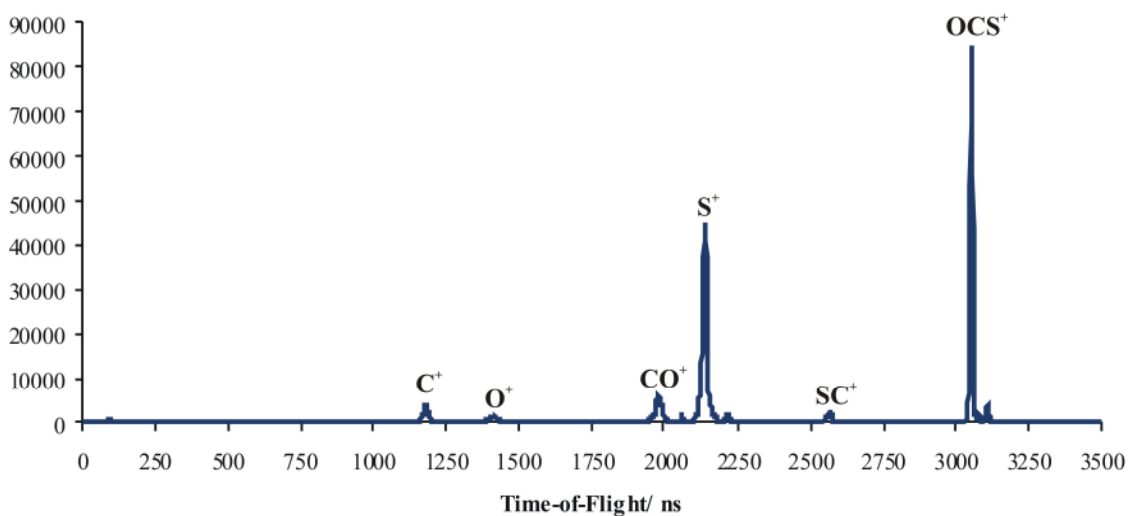


Figure 5.3.1 Singles time-flight-mass spectrum for the fragmentation of OCS by electron impact ionisation.

As discussed in Chapter 2, TOF is related to the mass of an ion by the following relationship:

$$t = k\sqrt{\frac{m}{z}} + c \quad 5.3.1$$

where z is the charge on the ion and k and c are constants, which depend on the electric fields in the mass spectrometer and in the delay in the detection electronics. From the mass spectrum the relative ion intensities, $I_1[X^+]$ for monocations, $I_2[X^{2+}]$ for dications and $I_3[X^{3+}]$ for trications, can be determined by summing the counts under each peak.

In all the singles mass spectra recorded, there is a small yet measurable contribution from background gases such as air and H_2O . Ions formed by the ionisation of these species may add to the number of counts observed for various ions of interest, hence these counts need to be subtracted from the spectra. In the singles spectrum of OCS, the ionisation of background O_2 and H_2O could contribute to the counts in the O^+ fragment ion peak. The relative intensities of O^+ are measured with respect to O_2^+ , $\sigma[O^+/O_2^+]$ and O^+ with respect to H_2O , $\sigma[O^+/H_2O^+]$. These measurements are taken during separate experiments on air and water, as a function of ionising electron energy. The subtraction of the ions from the residual gas can then be made by normalisation to O_2^+ and H_2O^+ peaks in each OCS singles spectrum:

$$I_1[O^+] = I[16] - I[32] \times \sigma \left[\frac{O^+}{O_2^+} \right] - I[18] \times \sigma \left[\frac{O^+}{H_2O^+} \right] \quad 5.3.2$$

In this equation $I[16]$, $I[18]$ and $I[32]$ represent the measured peak intensities at $m/Z = 16$, 18 and 32 respectively. The final intensity of O^+ ions formed by the dissociative ionisation of OCS in the singles spectrum is given by $I_1[O^+]$.

5.3.2 Pairs Spectra

The detection of two or three ions in a cycle are termed ‘pairs’ or ‘triples’ events respectively. It is possible for the data collection electronic to record events with four or more ion arrival times; however, it unlikely to get such events occurring from single ionisation, hence it is neglected, unless significant triple ionisation is observed. The intensity of each peak in the pairs spectrum is simply found by summing the number of counts in the peak, lying within a specified region: for example $P[X^+ + Y^+]$, as shown in

Figure 5.3.2. Pairs events can have different origins either coming from double ionisation, $P_2[X^+]$ or triple ionisation, $P_3[X^+]$ or $P_3[X^{2+}]$. The pairs or coincidence spectra (Figure 5.3.2) consist of a two-dimensional histogram of the flight times for both the ions (t_1 vs. t_2). The total contribution of the fragment to the pairs spectrum, $P_2[X^+]$, is found by summing all the counts in the all the peaks involving an X^+ ion.

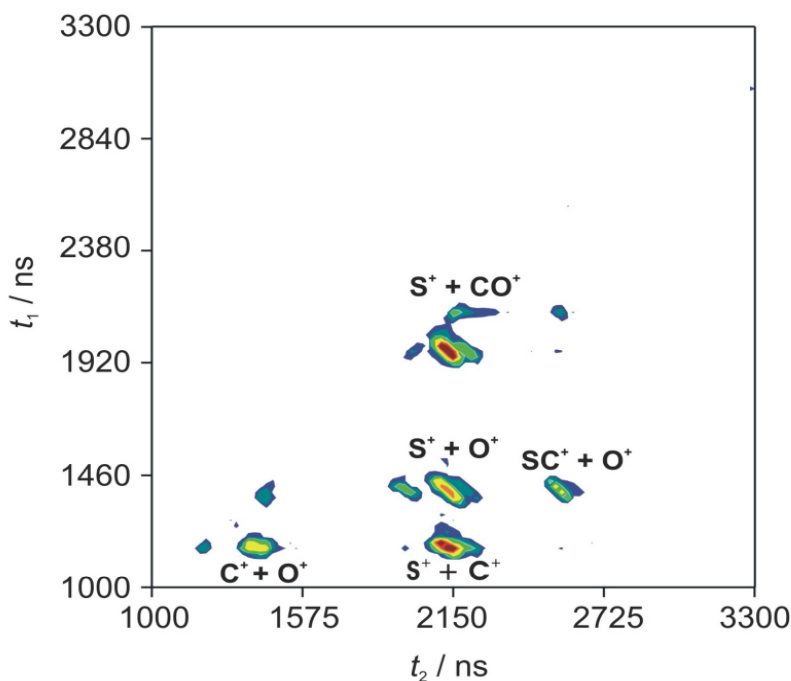


Figure 5.3.2 Pairs spectrum for the electron impact ionisation of OCS.

The peaks in the pairs spectra may contain a small contribution from ‘false’ ion pairs; this is as a result of two ions that are detected in coincidence but are formed from two separate ionisation events. The false coincidences are subtracted from the raw ion pair peak intensities using an auto-correlation function.^{10,11} False peaks in the pairs spectrum have a characteristic round or oval shape due the lack of momentum correlation between the two ions, formed in separate ionisation events. These peaks generally consist of two ion masses that cannot be formed by the same dissociative ionisation event, e.g. SC^+ and S^+ for the pairs spectrum of OCS. The intensity of each false pair peak is divided by the product of the relevant ion intensities in the corresponding singles mass spectrum to give a normalisation factor, α :

$$\alpha = \frac{P[\text{SC}^+ + \text{S}^+]}{I[\text{SC}^+]I[\text{S}^+]} \quad 5.3.3$$

The single ion intensities in Equation 5.3.3, $I[X^+]$, are the raw peak intensities measured in the relevant singles spectrum, prior to any corrections. Each normalisation factor is then used to find an average normalisation factor, α' . Therefore, the number of false counts that contribute to a 'real' ion peak can be calculated using α' and the corresponding single ion intensities:

$$\text{False } X^+ + Y^+ = \alpha' I[X^+]I[Y^+] \quad 5.3.4$$

The false counts are then subtracted from the raw pair peak intensity to correct for false coincidences. These false coincidences make up approximately 1.5% of the peak intensity.

As discussed previously the voltage conditions used during the experiments allow all fragment ions with a kinetic energy of ≤ 10.6 eV to be collected. If ions have a translational energy component, perpendicular to the TOF axis, greater than 10.6 eV then they will escape detection. These energetic ions can arrive from ion pairs, where at least one of the two correlated ions may go undetected, which results in a proportion of the ion pairs being missed. The ion pairs that are missed are those that have a kinetic energy release between the ion fragments that is aligned, broadly perpendicular, to the flight axis. It is possible to identify pairs of ions where one has been missed by plotting the pairs data as a time difference spectrum; this is where the ion pair counts are plotted as a function of the time difference between the respective ion flight times ($t_1 - t_2$). Ion pairs that have considerable translational energy and hence could be missed, contribute to the central region of the time difference distribution; losses of these ion pairs result in a clearly identified hollowing of the one dimensional peak shape, as shown in Figure 5.3.3.

To correct for such losses an appropriate geometric construction is used to estimate the number of counts missed, which is then added to the pairs peak intensity.

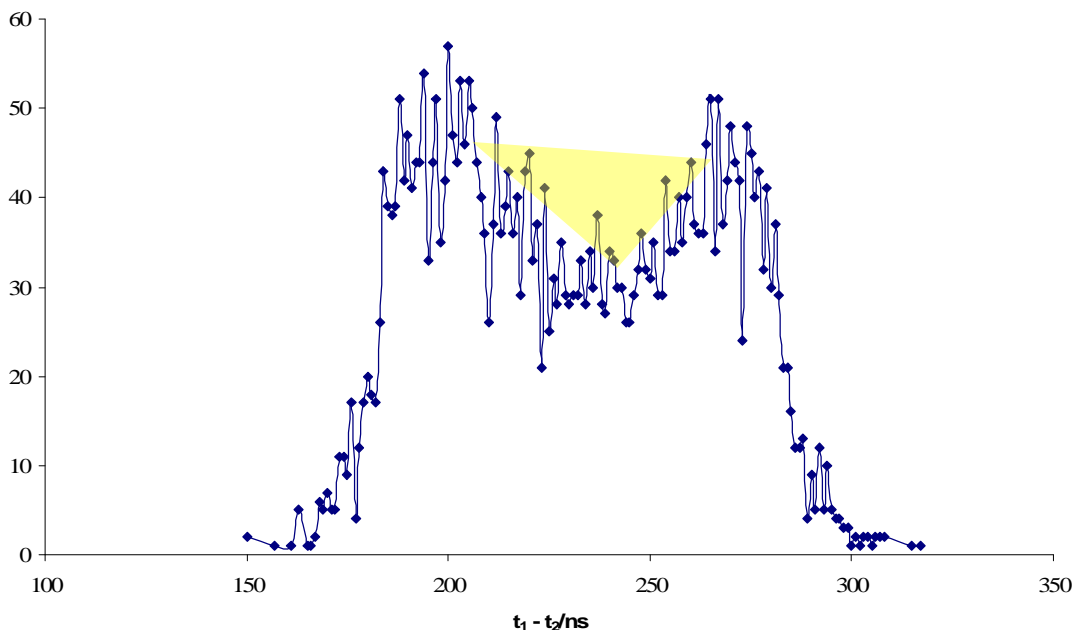


Figure 5.3.3 Time difference distribution for $O^+ + C^+$ recorded in the pairs spectrum for OCS. The shaded area indicates the counts missed due to energetic ion pairs; these losses are corrected for, using a suitable geometric construction.

In electron impact ionisation experimental set-up the discrimination circuit has a dead-time of 32 ns. As a result, for any ion pairs that arrive at the detector in the first 32 ns only the first ion will be detected and the second will be lost, giving rise to a ‘dead region’ in the pairs spectrum. These losses can be estimated by extrapolating the visible part of the time difference plot back to $t_1=t_2$ using simple geometry. This extrapolation makes use of the fact that, for most cases, the time difference distribution is flat-topped¹² in the dead time region. The estimated losses are added to the measured pairs peak intensity, to correct for dead time losses.

5.3.3 Triples Spectra

The processing of the triples spectra is similar to that of the pairs spectra; however, initially, one time-of-flight range for a specific ion is selected and all the ion triples containing this ion are extracted. Once extracted, the flight times of the remaining two

ions are displayed as a two-dimensional histogram. The intensity of each triple ion peak is found by summing the number of counts in the peak, e.g. $T[X^+Y^+Z^+]$. The number of counts for a specific ion is simply the sum of the number of counts for that particular ion.

The triples spectra can also be affected by false coincidences. A false triple ion can occur in one of two ways:

- (i) When three monocations are formed by three separate ionisation events and are detected in coincidence following a single ionisation pulse.
- (ii) When three monocations are formed by two separate ionisation events, one forming a pair of monocations, the other forming a single monocation and all are detected in coincidence.

Previous work has shown that under the experimental conditions described in this thesis, type (ii) false coincidences dominate.¹³ The contribution of false triples is subtracted from each peak in the triples spectrum. Similarly to the false coincidence in the pairs spectra a normalisation factor β , is calculated by dividing the intensity of a known false triples peak by the sum of the products of the relevant ion intensities from the pairs and singles spectra; for example in the triples spectrum for OCS a false triple would be $T[S^+SC^+O^+]$, for which β would be:

$$\beta = \frac{T[S^+ + SC^+ + O^+]}{P[S^+ + SC^+]I[O^+] + P[S^+ + O^+]I[SC^+] + P[SC^+ + O^+]I[S^+]} \quad 5.3.5$$

The number of false coincidences for each true triples peak can then be calculated using β and the corresponding ion pairs and singles intensities; for example the false coincidences for the triples peak of $T[O^+S^+C^+]$ would be:

$$T[O^+S^+C^+] = \beta[P[O^+S^+]I[C^+] + P[O^+C^+]I[S^+] + P[S^+C^+]I[O^+]] \quad 5.3.6$$

5.3.4 Relative Partial Ionisation Cross Sections

The ion intensities that are collected in the singles, pairs and triples spectra are processed to derive the relative PICS and also precursor-specific PICS. The relative PICS for the formation of fragment monocations X^+ are represented as $\sigma_r[X^+]$, similarly dications are represented as $\sigma_r[X^{2+}]$ and these are expressed relative to the cross section for forming the parent ion, OCS^+ . Precursor specific relative PICS are given by $\sigma_n[X^+]$ and $\sigma_n[X^{2+}]$ respectively and represent the cross section for forming a fragment by single ($n = 1$), double ($n = 2$) or triple ($n = 3$) ionisation, with respect to the cross section for forming the parent monocation. The peak intensities recorded in the ion coincidence spectra are also processed to derive relative PICS for ion pair formation by dissociation of the parent dication, given as $\sigma_r[X^+ + Y^+]$. The equations to derive the relative PICS are shown below and derived in full in Appendix C.

$$\sigma_r[X^+] = \frac{I[X^+] + P_2[X^+] + P_3[X^+] + T[X^+]}{I[parent^+]} \quad 5.3.7$$

$$\sigma_r[X^{2+}] = \frac{I_2[X^{2+}] + P_3[X^{2+}]}{I[parent^+]} \quad 5.3.8$$

$$\sigma_r[X^{3+}] = \frac{I_3[X^{3+}]}{I[parent^+]} \quad 5.3.9$$

Before being able to calculate the precursor specific PICS, one must first determine the ion detection efficiency, f_i . The ion detection efficiency allows for the possibility that, due to the less than unit detection efficiency of the apparatus, multiple ionisation events in which a product ion pair or ion triple are formed, could contribute to the singles spectra. The determination of f_i requires separate calibration experiments to be performed. CF_4 was chosen for these calibration experiments as the PICS are well characterised for this molecule. Bruce and Bonham^{10,11} have measured the absolute PICS for the formation of single fragment ions σ_s and product ion pairs σ_p following the

electron ionisation of CF₄. The values obtained from these experiments can be related to the total number of ions recorded in the singles mass spectrum $I[X^{m+}]$ and the total number of ions recorded in the pairs spectrum $P[X^{m+}]$:

$$\sum P = 2f_i^2 k \sum \sigma_p \quad 5.3.10$$

$$\sum I = f_i k \sum \sigma_s \quad 5.3.11$$

These equations can then be combined to derive an expression for f_i :

$$f_i = \left(\frac{\sum P}{\sum I} \right) \left(\frac{\sum \sigma_s}{2 \sum \sigma_p} \right) \quad 5.3.12$$

Any contributions to the spectral intensities from ion triples are assumed to be small and hence, are neglected in the analysis. The value of f_i used during the analysis of the OCS data is 0.25 ± 0.01 , which is in good agreement with the absolute values of f_i reported in the literature.^{9,12}

The precursor specific relative PICS, σ_n , can be derived for the formation of all fragment ions detected, using the measured spectral intensities and f_i , as shown below; again, the complete derivations can be found in Appendix C.

$$\sigma_1[X^+] = \frac{I[X^+] - ((1-f_i)/f_i)(P_2[X^+] + P_3[X^+]) + ((1-f_i)^2/f_i^2)T[X^+]}{I[\text{parent}^+]} \quad 5.3.13$$

$$\sigma_2[X^+] = \frac{P_2[X^+] - 2((1-f_i)/f_i)T[X^+]}{f_i I[\text{parent}^+]} \quad 5.3.14$$

$$\sigma_3[X^+] = \frac{(P_3[X^+]/f_i) + (T[X^+]/f_i)}{I[\text{parent}^+]} \quad 5.3.15$$

$$\sigma_2[X^{2+}] = \frac{I_2[X^{2+}] - ((1 - f_i)/f_i)P_3[X^{2+}]}{I_1[parent^+]} \quad 5.3.16$$

$$\sigma_3[X^{2+}] = \frac{P_3[X^{2+}]}{f_i I_1[parent^+]} \quad 5.3.17$$

$$\sigma_3[X^{3+}] = \frac{I_3[X^{3+}]}{I_1[parent^+]} = \sigma_r[X^{3+}] \quad 5.3.18$$

The experimental set-up is only able to detect positive ions; contributions from cation-anion pairs will be included in the experimentally derived cross sections as they cannot be distinguished from a positive ion pair. However, these contributions are expected to be low as the cross sections for forming such ion pair are typically several orders of magnitude lower than the respective total ionisation cross section.

5.4 Results

5.4.1 Relative Partial Ionisation Cross Sections for OCS

Mass and coincidence spectra of OCS were recorded using ionising electron energies in the range 30 – 200 eV. The ion intensities measured in the mass spectra are processed using data reduction method described previously, to yield the relative PICs σ_r for the formation of SO^+ , SC^+ , CO^+ , S^+ , C^+ , O^+ , OCS^{2+} , SC^{2+} , O^{2+} , C^{2+} and S^{2+} product ions. The relative PICS are displayed in Figure 5.4.1 and in Table 2; these values represent the averages of four independent experimental determinations. The precursor-specific relative PICS σ_n were also calculated using the data reduction procedure described above. These results are shown in Figure 5.4.2 and Table 2; the values of σ_n , where $n = 1, 2$ or 3 , are compared to the values obtained by Wang and Vidal.³

Errors for σ_r and σ_n were calculated by taking the standard deviation over the four data sets; representative error bars are shown in both Figure 5.4.1 and 5.4.2. To ensure that the error bars could be seen on the plots, some of the errors were scaled up: for σ_r the errors

for SC^+ , S^+ and SC^{2+} were multiplied by two, OC^+ , O^+ , C^+ , OCS^{2+} and C^{2+} were multiplied by five and the error for SO^+ did not have to be scaled. The errors for some of the precursor-specific PICS were also adjusted to appear on the plots. The σ_1 errors did not have to be altered; for σ_2 the errors for C^+ , SC^{2+} and O^{2+} were not altered and all other errors were multiplied by ten; finally the errors for σ_3 for S^+ , O^+ and C^+ were multiplied by twenty, two and ten respectively and the errors for the doubly charged ions were not scaled. These steps were taken simply so the errors could be seen on the plots shown below as the original errors were generally too small. When comparing this work with that of Wang and Vidal the original errors, not the scaled errors, were considered. The overall contributions from single, double and triple ionisation, as a percentage of the total ion yield at each ionising electron energy is summarised in Figure 5.3.3.

5.4.1.1 Relative PICS (σ_r) Values

The relative PICS for the electron ionisation of OCS are shown in Figure 5.4.1. These plots indicate that, with the exception of the parent ion, S^+ is the most abundant ion to be formed at all ionising energies in the range 30 – 200 eV. The σ_r values calculated are not in good agreement with the numbers of Wang and Vidal,³ as can be seen in Table 2. The relative PICS for ions such as S^+ , SC^+ and SO^+ are, within the errors, the same as those values of Wang and Vidal, however; the σ_r values calculated in this thesis for OC^+ , C^+ and O^+ are approximately half the values found by Wang and Vidal. The reasons for this disagreement are discussed further in Section 5.3.2.3.

| | Wang and Vidal | | | | This Work | | | |
|-------------------------|----------------|------------|------------|------------|------------|------------|------------|------------|
| | σ_r | σ_1 | σ_2 | σ_3 | σ_r | σ_1 | σ_2 | σ_3 |
| SO⁺ | 0.0017 | 0.0016 | 0.0001 | 0.0000 | 0.0012 | 0.0011 | 0.0001 | |
| SC⁺ | 0.0763 | 0.0704 | 0.0059 | 0.0000 | 0.0748 | 0.0645 | 0.0102 | |
| S⁺ | 1.3750 | 1.2632 | 0.0995 | 0.0009 | 1.1145 | 0.8636 | 0.2447 | 0.0094 |
| OC⁺ | 0.4191 | 0.3638 | 0.0517 | 0.0037 | 0.2361 | 0.0995 | 0.1366 | 0.0045 |
| O⁺ | 0.2605 | 0.1868 | 0.0509 | 0.0042 | 0.0835 | 0.0167 | 0.0574 | 0.0093 |
| C⁺ | 0.3118 | 0.2428 | 0.0575 | 0.0002 | 0.1350 | 0.0417 | 0.0842 | 0.0092 |
| OCS⁺⁺ | 0.0664 | | 0.0664 | 0.0000 | 0.0240 | | | |
| SC⁺⁺ | 0.0014 | | 0.0011 | 0.0003 | 0.0006 | | 0.0005 | 0.0001 |
| C⁺⁺ | 0.0026 | | 0.0016 | 0.0010 | 0.0003 | | | |
| O⁺⁺ | 0.0014 | | 0.0009 | 0.0005 | | | 0.0004 | 0.0003 |
| S⁺⁺ | 0 | | 0 | 0.0034 | 0.0012 | | -0.0034 | 0.0045 |
| CO⁺⁺ | | | 0.0003 | 0.0002 | | | | |

Table 2. Details of the σ_r , σ_1 , σ_2 and σ_3 values calculated by Wang and Vidal using covariance mapping. These values are compared to the numbers calculated in this thesis.

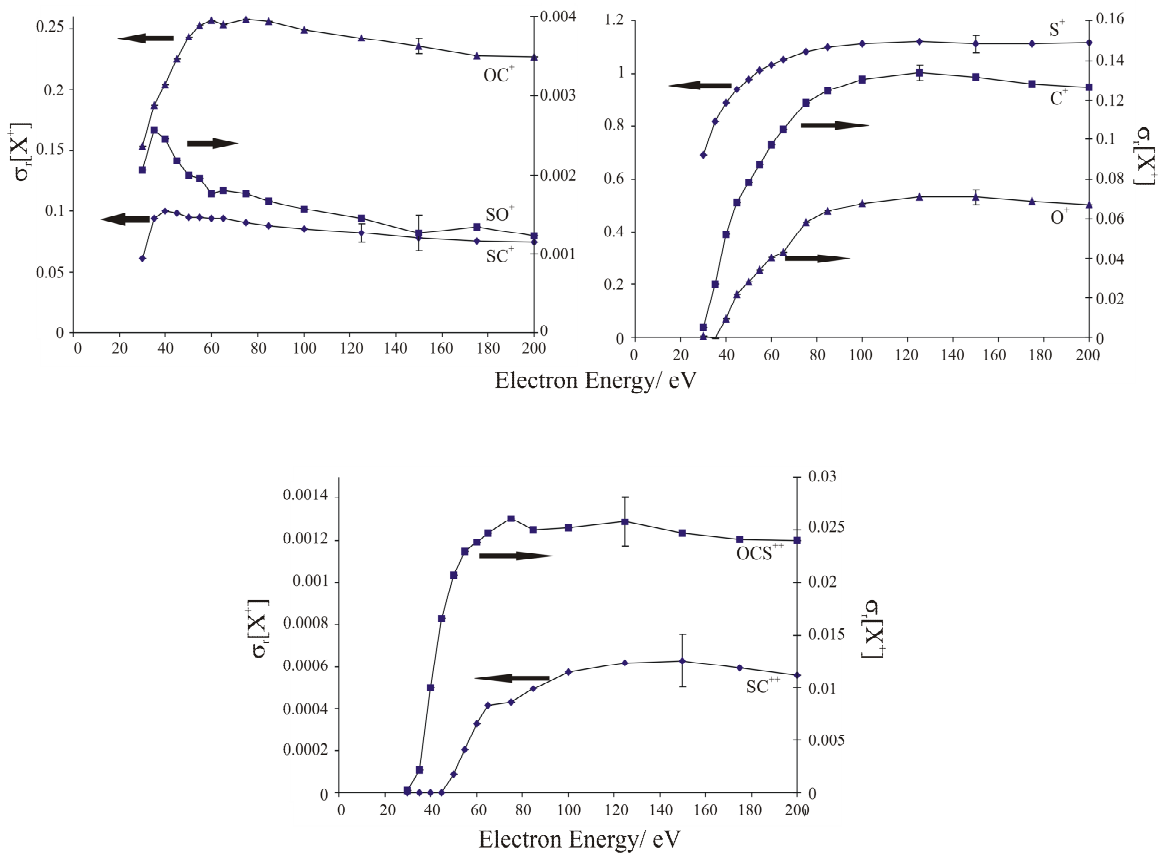


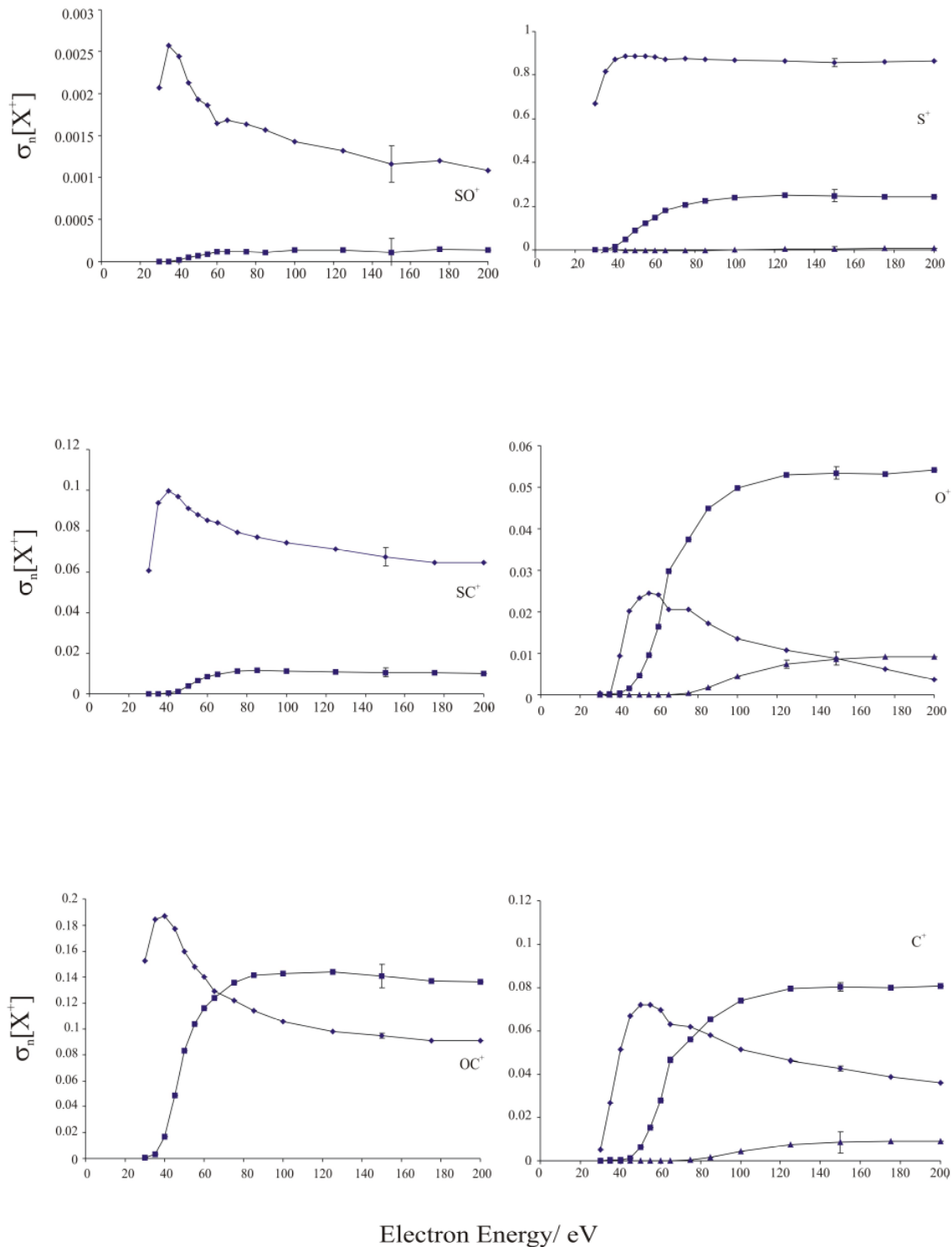
Figure 5.4.1 Relative PICS $\sigma_r[X^+]$ for forming ionic fragments following electron ionisation of OCS.

In Figure 5.4.1 the line shown for OC^+ and O^+ will include contributions from S^{2+} ; as S^{2+} occurs at mass 16 in the mass spectrum it is hard to disentangle the two peaks.

5.4.1.2 Precursor-Specific Relative PICS

In Figure 5.4.2 a comparison is made between the relative precursor-specific PICS σ_n values for the formation of the various ion fragments. Figure 5.4.2 indicates that for sulphur containing ions the ion yield is dominated by single ionisation with double ionisation first occurring at 40 eV and reaching a plateau at 75 eV. Whereas for O^+ , C^+ and OC^+ the contribution from double ionisation increases rapidly from 35 eV and at above 75 eV becomes the more dominant ionisation mechanism, levelling off at around 120 eV. The triple ionisation channel for the atomic ions becomes significant between 75 and 85 eV; this is more apparent for O^+ and C^+ in Figure 5.4.2 as the scale for the S^+ plot is larger than for the other graphs.

Chapter 5. Studies of the Dissociation and Energetics of Singly and Doubly Ionised OCS



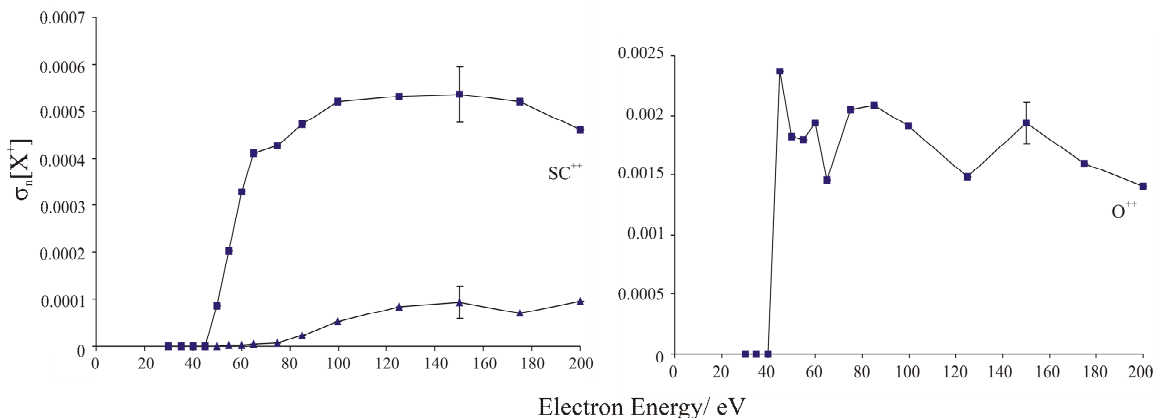


Figure 5.4.2 Relative precursor-specific PICS $\sigma_n[X^+]$ for forming ionic fragments *via* dissociative single (\diamond), double (\blacksquare) or triple (\blacktriangle) ionisation of OCS.

The data for O^{++} has been included in Figure 5.4.2; however, the O^{++} signal was weak and there was a considerable error associated with it. This accounts for the fluctuations in the signal at different energies.

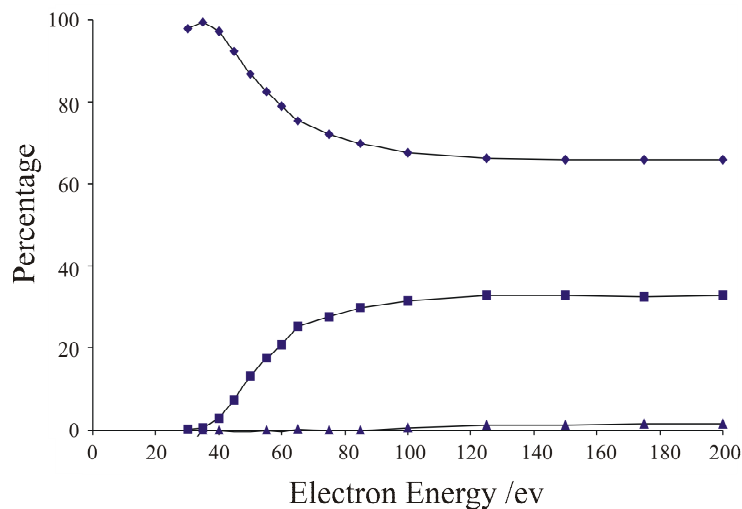


Figure 5.4.3 Contributions to the total ion yield from single (\diamond), double (\blacksquare) and triple (\blacktriangle) ionisation, following the electron impact ionisation of OCS.

Figure 5.4.3 shows the general trends in the relative contributions to the respective ion yields of OCS from single and double ionisation. Single ionisation gives the highest yield

of ions at 35 eV and then gradually decreases as the double ionisation pathway opens at 40 eV and begins to rise. For σ_n both single and double ionisations begin to reach a plateau at 100 eV, where the first significant contributions from triple ionisation are observed.

5.4.2 Discussion

As mentioned above in Section 5.4.1.2, the majority of the results presented in this thesis are not in close agreement with the electron impact ionisation data obtained by Wang and Vidal.³ Previous experimental data¹³ for CO₂ compared very well to similar experiments carried out by the Vidal group. Hence it is somewhat unexpected that the data sets for OCS do not agree. The Vidal group use the technique of two- and three- dimensional covariance mapping to obtain absolute ionisation cross sections, which have been processed to give the relative ionisation cross sections for the purpose of this comparison. The experimental method employed by Wang and Vidal involves a molecular beam that is provided by a continuous gas flow; this beam perpendicularly bisects a beam of electrons produced by a pulsed electron gun.³ A focusing time-of-flight mass spectrometer is used to collect the ions and detected, using multichannel plates. Once the data is collected, considerable analysis is required to achieve the total coincidence between three ions; this can then be plotted in space to get a three-dimensional covariance map, or covariance volume. This method was the same for both the CO₂ and OCS data sets.

The previous work on CO₂¹³ showed inconsistencies in the impact ionisation studies of Orient and Srivastava¹⁴ due to the loss of ionic fragments with high translational energy. However, when comparing the data to that of Tian and Vidal^{15,16} and Straub *et al*¹⁷ the agreement with the UCL data of King *et al*¹³ was deemed to be excellent, with the values of $\sigma_r[\text{O}^{2+}]$ obtained from this group to be approximately 30% lower than those of Tian and Vidal, but with both data sets agreeing within their mutual error limits. When considering OCS there is the problem that the amount of work carried out on OCS is limited. Although the groups of Srivastava and Straub have carried out a variety of electron impact ionisation studies but have not studied OCS; the most recent and directly

comparable work is that of Wang and Vidal.³ As Table 2 shows, the difference between the values obtained in this thesis and those found by Wang and Vidal are considerable, notably for OC^+ , O^+ and C^+ . These differences between the data presented here and that obtained by Wang and Vidal could be explained by the loss of energetic ions in the spectra collected for this thesis. However, it must be noted that in the pairs spectrum it was only the O^+/C^+ pair that had to be corrected for energetic ion losses. However, a considerable loss of high energy ions has not been observed for other molecules and seems unlikely to be the issue with this data. To test this, an extra set of OCS data at 200 eV was collected with reduced TOFMS fields, so to increase any losses of energetic ions. If reduced signals were observed then this would imply that the original data were also affected and steps could be taken to rectify this problem. However, this experiment showed that, within error, the number of ions collected, when compared with the original data sets, with the lower TOFMS fields were the same as the data collected with the normal field settings; this therefore indicates that there are no significant losses of energetic ions. Further analysis of the Wang and Vidal³ data revealed that values for σ_n provided in their publication for the atomic ions did not sum to give the value of σ_r stated in their table. This indicates that there may be other issues with their data that might, at first glance, not be apparent.

5.4.3 The Energetics of OCS Dissociation

The kinetic energy of the ion pairs formed by dissociation of OCS has been determined using Monte Carlo simulations of the peaks observed in the pairs spectrum. All of the kinetic energy releases (KER) were determined at electron energies greater than 55 eV, as the coincidence spectra at below 55 eV contained insufficient coincidence data to yield statistically significant results. In the simulations all KER components were modelled using a Gaussian distribution with a width at FWHM, that could be varied to best fit the data, the details of which are shown in Table 3 below.

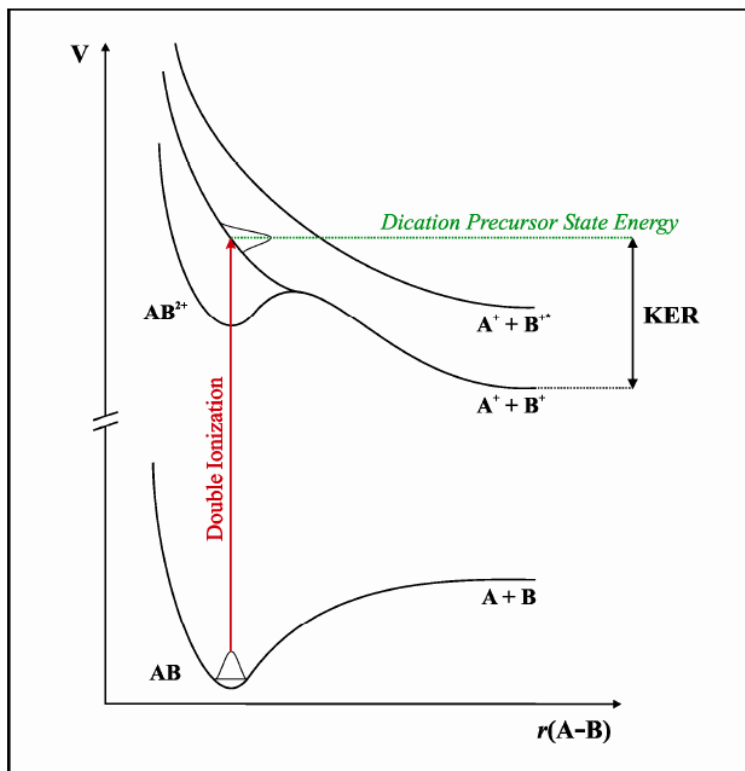


Figure 5.4.4 Schematic potential energy curves for a molecule AB, showing the relationship between the asymptotic energy of the dissociation limit, the KER and the energy of the dication precursor state that gives rise to the ion pair formation.

For the ion pairs of $S^+ + CO^+$ and $SC^+ + O^+$ the spectra indicate that there are two kinetic energy releases; and this is due to the dissociation of two different states of the OCS dication: OCS^{2+} and OCS^{2+*} . The energy release from OCS^{2+*} will be greater than that of OCS^{2+} hence the two KERs. The different KERs can be seen as a step in the time of flight difference spectrum. The spread in time of flight difference, for a single KER arises, of course, because the different orientations in which the OCS^{2+} can dissociate. If the heavy product monocation receives an impulse toward the detector from the dissociation, the light product will receive an impulse away from the detector. This dissociation orientation will mean the heavy ion arrives “early” and the light ion arrives “late” (as it has to be “turned round”). In this situation we measure the smallest time of flight difference between the ions. Conversely if the heavy ion is initially formed with a velocity away from the detector it then arrives late and the light ion, with an initial impulse towards the detector, arrives early and a maximal time of flight difference is

measured. If all ions are detected the time of flight difference spectrum of a single KER exhibits a square peak with a width, which can be explained by the above logic, and related to the KER. If there are two KERs in a given dissociation the time of flight difference spectrum appears as two peaks superimposed (Figure 5.4.5):

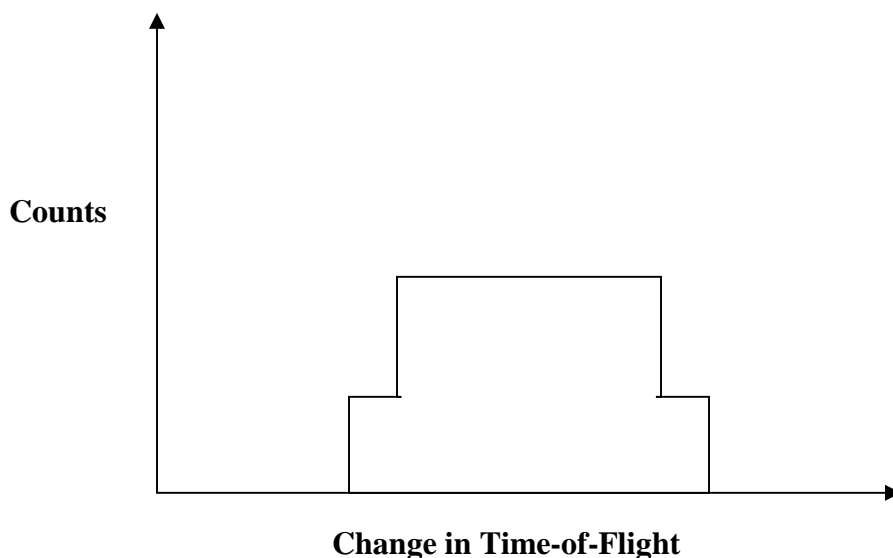


Figure 5.4.5 Schematic diagram to show the steps that can be seen in the time difference spectrum if there are two KERs for a given dissociation.

| Ion Pairs | KER/eV | Second KER/eV | Width /eV | Second KER width/eV |
|-----------------|---------------|---------------|-----------|---------------------|
| $S^+ + CO^+$ | 4 ± 0.2 | 5 ± 0.3 | 1.2 | 1.2 |
| $S^+ + C^+ + O$ | 6 ± 0.3 | - | 1.7 | - |
| $SC^+ + O^+$ | 4.8 ± 0.2 | 6 ± 0.2 | 1 | 1.5 |
| $S^+ + O^+ + C$ | 5.5 ± 0.5 | - | 1.8 | - |
| $O^+ + C^+ + S$ | 7.8 ± 0.2 | - | 2.5 | - |

Table 3. Details of the kinetic energy releases and peaks widths for the fragment ion pairs formed from the electron ionisation of OCS, calculated by use of a Monte Carlo simulation.

The kinetic energy releases shown in Table 3 are used to calculate the precursor energy levels populated in OCS^{2+} using the following relationship:

$$E(\text{OCS}^{2+}) = \text{KER} + E(\text{X}^+ + \text{Y}^+ + \text{N}) \quad 5.4.1$$

Where, X^+ , Y^+ and N represent the relevant ion pairs and the neutral. The values obtained from this calculation are shown in Table 4. The results obtained in this thesis are compared with photon impact ionisation data obtained by the Eland group¹⁸ and with electron impact ionisation studies by Cooks *et al.*¹⁹

| Ion Pair | Precursor State | Precursor State | Literature Values/ eV |
|----------------------------|-----------------|--------------------------|---------------------------|
| | Energy/eV | Energy for Second KER/eV | |
| $\text{S}^+ + \text{CO}^+$ | 31.5 ± 0.7 | 32.5 ± 0.5 | 31.5^{b} |
| $\text{S}^+ + \text{C}^+$ | 41.9 ± 1 | - | $40.2 \pm 1^{\text{a}}$ |
| $\text{SC}^+ + \text{O}^+$ | 36.7 ± 0.5 | 37.9 ± 1 | $33.5 \pm 0.5^{\text{a}}$ |
| $\text{S}^+ + \text{O}^+$ | 43.8 ± 0.7 | - | $40.2 \pm 1^{\text{a}}$ |
| $\text{O}^+ + \text{C}^+$ | 46.9 ± 1 | - | $47 \pm 3^{\text{a}}$ |

Table 4. Details of the excited energy states calculated from the KERs. This data is compared to the values obtained using photon ionisation by the Eland group¹⁸ (^a) and Cooks *et al*¹⁹ data from electron impact ionisation (^b).

As discussed previously, the amount of work carried out on the electron impact ionisation of OCS is far from extensive, hence the need to compare the data presented in the this thesis to photon ionisation studies. The values obtained from the literature for the excited states energies have been compared with our data for the different fragmentation ion pairs. The agreement of the literature values to the new data is generally good, notably so for the $\text{S}^+ + \text{CO}^+$ and $\text{C}^+ + \text{O}^+$ ion pairs, and the data for the other ion pairs agrees within the error limits. Comparing the data shown in Table 4 to that of Eland and co-workers¹⁸ (also shown in Table 4) suggests that the ground state, or one of the lowest lying states, of OCS^{2+} , which lies at approximately 31.5 eV dissociates to form $\text{S}^+ + \text{CO}^+$ ions.

5.5 Summary

The relative PICS for the formation of fragment ions following the dissociative electron ionisation of OCS in the energy range 30 – 200 eV have been measured. The data obtained is compared with the work of Wang and Vidal³ at 200 eV and it is observed that agreement between the two sets of data is not strong, particularly for the O⁺, C⁺ and OC⁺ ions. Precursor specific relative PICS have also been derived for the formation of the various ion fragments observed; these quantify the contributions to the yield from single, double and triple ionisation. The kinetic energy releases for the various ion pairs have been calculated and these values have been used to calculate the OCS²⁺ excited state energies; these values are compared to those found in the literature and, within the error limits, are in good agreement.

5.6 References

- 1 T. Masuoka, I. Koyano, and N. Saito, *Journal of Chemical Physics* **97**, 2392 (1992).
- 2 J. H. D. Eland, *Chemical Physics* **294**, 171 (2003).
- 3 P. Q. Wang and C. R. Vidal, *Journal of Chemical Physics* **118**, 5383 (2003).
- 4 W. C. Wiley and I. H. McLaren, *Review of Scientific Instruments* **26**, 1150 (1955).
- 5 P. Calandra, C. S. S. O'Connor, and S. D. Price, *Journal of Chemical Physics* **112**, 10821 (2000).
- 6 M. R. Bruce and R. A. Bonham, *Zeitschrift Fur Physik D-Atoms Molecules and Clusters* **24**, 149 (1992).
- 7 R. F. Stebbings and B. G. Lindsay, *Journal of Chemical Physics* **114**, 4741 (2001).
- 8 J. H. D. Eland, *Molecular Physics* **61**, 725 (1987).
- 9 D. M. Curtis and J. H. D. Eland, *International Journal of Mass Spectrometry and Ion Processes* **63**, 241 (1985).
- 10 L. J. Frasinski, K. Codling, and P. A. Hatherly, *Science* **246**, 1029 (1989).
- 11 L. J. Frasinski, M. Stankiewicz, P. A. Hatherly, and K. Codling, *Measurement Science & Technology* **3**, 1188 (1992).
- 12 J. H. D. Eland, F. S. Wort, and R. N. Royds, *Journal of Electron Spectroscopy and Related Phenomena* **41**, 297 (1986).
- 13 S. J. King and S. D. Price, *International Journal of Mass Spectrometry* **272**, 154 (2008).
- 14 O. J. Orient and S. K. Srivastava, *Journal of Physics B-Atomic Molecular and Optical Physics* **20**, 3923 (1987).
- 15 C. C. Tian and C. R. Vidal, *Physical Review A* **58**, 3783 (1998).
- 16 C. C. Tian and C. R. Vidal, *Journal of Chemical Physics* **108**, 927 (1998).
- 17 H. C. Straub, B. G. Lindsay, K. A. Smith, and R. F. Stebbings, *Journal of Chemical Physics* **105**, 4015 (1996).
- 18 P. Millie, I. Nenner, P. Archirel, P. Lablanquie, P. Fournier, and J. H. D. Eland, *Journal of Chemical Physics* **84**, 1259 (1986).
- 19 R. G. Cooks, Terwilli.Dt, and J. H. Beynon, *Journal of Chemical Physics* **61**, 1208 (1974).

Chapter 6

Further Work

The previous chapters in this thesis have described the UCL Cosmic Dust Experiment, including changes to the experimental set-up and new results that provide a complete rovibrational distribution of molecular hydrogen formed on a cold graphite surface. Also included in this thesis are experimental results for the electron impact ionisation of OCS; however, for this chapter on further experiments, the focus will remain on the Cosmic Dust Experiment.

6.1 Water in the ISM

In the interstellar medium OH and water is highly abundant; water is thought to be the most abundant condensed material in the Universe, as it forms water ice on dust grain surfaces. Amorphous solid water ice is readily observed spectroscopically in the ISM *via* infrared absorption lines.^{1,2} The icy mantles that cover the dust grains are thought to have formed after direct freeze-out of gas phase species and after surface reactions of atoms and radicals. Water ice is by far the most abundant species present in these icy mantles; however, its exact origin is still uncertain. Similarly to molecular hydrogen, the gas phase reaction required to produce water is not efficient enough to account for the abundances of water observed in dark clouds, especially in its solid form.³ Therefore, water is now believed to form directly on the dust grain surfaces, rather than as a condensate after formation in the gas phase.

A number of water formation mechanisms have been proposed; one that has been investigated experimentally by the Lemaire group⁴ is the $O_3 + H$ reaction pathway where O_2 simply plays a catalytic role. Lemaire *et al* dosed O_3 and D onto an amorphous water ice surface and were able to detect nascent HDO molecules. Oba *et al* have also studied the formation of water under astrophysically relevant conditions.⁵ They found that when O_2 and H were co-deposited onto a cold (10 - 40 K) aluminium substrate, both H_2O and H_2O_2 were continuously formed, even at 40 K and the H_2O had an amorphous structure. The amount of work carried out on the formation of H_2O on dust grain surfaces is still very limited and given the problems discussed in Chapter 4 the decision has been made to

use the Cosmic Dust Experiment to investigate the formation of water and/or OH on a graphite surface.

6.1.1 Preliminary Experiments

Early experiments have been carried out to investigate the formation of water and OH on the HOPG surface. Initially, it was necessary to discover if it was possible to detect OH with the current laser and experimental set-up, so formic acid was used to produce OH. It was possible to photoionise the formic acid and do REMPI of the OH fragment with the same laser beam. The OH was detected successfully and the spectrum compared with the literature.

The microwave dissociation sources, described in Chapter 2, are now being used to produce O atoms and either H atoms or D atoms depending on the experiment. H atoms are required when probing the formation of OH as if D were used, then the peak in the mass spectrum from nascent OD would overlap with the background water peak; whereas D atoms are required when studying water formation so D₂O is formed and again does not overlap with the background water peak in the mass spectrum. Initial formation experiments suggest that any OH or D₂O that is formed on the surface does not desorb; however, crude TPD style experiments, *i.e.* gradually heating the surface after the sources have been on for a while, suggest that D₂O does desorb from the graphite at ~160 K.

6.1.2 Safety

When the Cosmic Dust Experiment was used to probe the formation of molecular hydrogen the microwave dissociation sources were on the majority of the time; this was because the source took approximately a week to reach their maximum efficiency. This would also be the case for an oxygen source. However, this causes a problem: if the O and H sources are left on all of the time, including overnight, and there was a power cut or the pumps failed, there would be a build up of O and H atoms in the vacuum chamber and a small spark, *i.e.* from the ion gauge, could cause an explosion. The correct steps need to be taken to ensure that this does not happen. Firstly, to prevent a build up of O and H in the pump exhaust lines a continuous flow of nitrogen is allowed through the

Chapter 6. Further Work

exhaust lines to blow the gases through. Secondly, solenoid valves will be placed between the turbo pumps and the rotary pumps so that in the event of a power failure the O and H will not be able to get into the backing lines. The final safety measure is a third solenoid valve that will open if the power fails and let 2 bar pressure of nitrogen into the chambers, venting the chambers and preventing a significant build up of oxygen and hydrogen.

6.2 Other Interstellar Grain Analogue Surfaces

As discussed in Chapter 1, the composition of interstellar dust grains is not accurately known; hence it would be of use to astronomers to investigate the formation of molecular hydrogen or OH and water on other suitable surfaces. Silicates are known to be present in the ISM, so experiments on silicate surfaces, such as olivine, would enable direct comparison with the data obtained for HOPG.^{6,7} Olivine is a mixture of Mg_2SiO_4 and Fe_2SiO_4 and the use of this material would allow the results to be compared with other experiments where olivine has been used to study molecular hydrogen formation. It would also be advantageous to use an amorphous carbon surface as it is unlikely that dust grains are as ordered as the HOPG used for the experiments described in this thesis. Similarly, ice surfaces could be used to investigate the formation of hydrogen and water or OH, as it is well known that icy mantles cover the dust grains in dark clouds, and again it would allow comparison with other experiments.⁸⁻¹¹

6.3 Summary

This Chapter has discussed some of the future plans for the Cosmic Dust Experiment, describing some of the steps already being taken to allow the formation of water and OH on the graphite to be investigated. The amount known about the formation of these molecules in the ISM is limited, so it is hoped that these experiments will provide some more answers and help to untangle the complex web that is the chemistry of the interstellar medium.

6.4 References

- ¹ E. L. Gibb, D. C. B. Whittet, W. A. Schutte, A. C. A. Boogert, J. E. Chiar, P. Ehrenfreund, P. A. Gerakines, J. V. Keane, A. Tielens, E. F. van Dishoeck, and O. Kerkhof, *Astrophysical Journal* **536**, 347 (2000).
- ² A. C. A. Boogert, K. M. Pontoppidan, F. Lahuis, J. K. Jorgensen, J. C. Augereau, G. A. Blake, T. Y. Brooke, J. Brown, C. P. Dullemond, N. J. Evans, V. Geers, M. R. Hogerheijde, J. Kessler-Silacci, C. Knez, P. Morris, A. Noriega-Crespo, F. L. Schoier, E. F. van Dishoeck, L. E. Allen, P. M. Harvey, D. W. Koerner, L. G. Mundy, P. C. Myers, D. L. Padgett, A. I. Sargent, and K. R. Stapelfeldt, *Astrophysical Journal Supplement Series* **154**, 359 (2004).
- ³ B. Parise, C. Ceccarelli, and S. Maret, *Astronomy & Astrophysics* **441**, 171 (2005).
- ⁴ H. Mokrane, H. Chaabouni, M. Accolla, E. Congiu, F. Dulieu, M. Chehrouri, and J. L. Lemaire, *Astrophysical Journal Letters* **705**, L195 (2009).
- ⁵ Y. Oba, N. Miyauchi, H. Hidaka, T. Chigai, N. Watanabe, and A. Kouchi, *Astrophysical Journal* **701**, 464 (2009).
- ⁶ V. Pirronello, O. Biham, C. Liu, L. O. Shen, and G. Vidali, *Astrophysical Journal* **483**, L131 (1997).
- ⁷ V. Pirronello, C. Liu, L. Y. Shen, and G. Vidali, *Astrophysical Journal* **475**, L69 (1997).
- ⁸ J. E. Roser, G. Manico, V. Pirronello, and G. Vidali, *Astrophysical Journal* **581**, 276 (2002).
- ⁹ J. E. Roser, S. Swords, G. Vidali, G. Manico, and V. Pirronello, *Astrophysical Journal* **596**, L55 (2003).
- ¹⁰ L. Hornekaer, A. Baurichter, V. V. Petrunin, D. Field, and A. C. Luntz, *Science* **302**, 1943 (2003).
- ¹¹ L. Hornekaer, A. Baurichter, V. V. Petrunin, A. C. Luntz, B. D. Kay, and A. Al-Halabi, *Journal of Chemical Physics* **122** (2005).

Appendix A. Calculation of Ion Flight Times in a Two Field Time-of-Flight Mass Spectrometer

The mass, m , of an ion can be determined using time-of-flight mass spectrometry by recording the time it takes for the ion to travel a known distance, after having accelerated through an electric potential. The flight time, t , is then given by the equation¹:

$$t = k\sqrt{m} + C \quad \text{A.1}$$

where k and C are constants.

Figure A.1 shows a schematic diagram of the time-of-flight mass spectrometer (TOFMS) used in the experiments described in this thesis, with the dimensions appropriately labelled for the ion flight time calculations.

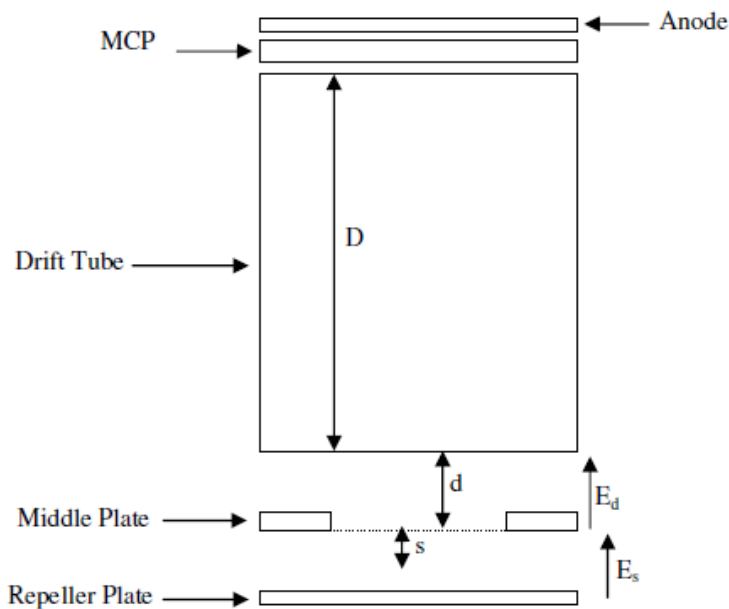


Figure A.1 Schematic diagram of TOFMS showing the dimensions and electric fields needed to calculate an ion's flight time.

Appendix A. Calculations of Ion Flight Times in a Two Field Time-of-Flight Mass Spectrometer

The energy, U , that an ion of charge, q , gains as it moves through an electric field, E , which acts over a distance, s , is given by the equation:

$$U = qsE \quad \text{A.2}$$

The final energy gained by an ion of initial energy, U_0 , travelling through the TOFMS shown in Figure A.1 is given by:

$$U = U_0 + qsE_s + qdE_d \quad \text{A.3}$$

The time of flight of an ion (in seconds) travelling in the spectrometer is the sum of the time it takes to travel the distances s , d , and D :

$$t = t_s + t_d + t_D \quad \text{A.4}$$

A standard result from Newtonian mechanics is used to find the time, t_s , it takes for the ion to travel from the point of ionisation to the middle plate of the spectrometer:

$$t_s = \frac{v_s - v_0}{a} \quad \text{A.5}$$

where v_0 is the initial velocity of the ion, v_s is the ion's velocity after being accelerated through a distance s , and a is the acceleration the ion undergoes due to the electric field, E_s .

v_s is found from:

$$v_s^2 = v_0^2 + 2as \quad \text{A.6}$$

Appendix A. Calculations of Ion Flight Times in a Two Field Time-of-Flight Mass Spectrometer

Substituting equation A.6 into equation A.5 gives:

$$t_s = \frac{(v_0^2 + 2as)^{\frac{1}{2}} \pm v_0}{a} \quad \text{A.7}$$

The \pm in front of v_0 is due to the fact that some of the ions will be created with an initial velocity in the direction of the detector whereas some ions will have initial velocities away from the detector.

The kinetic energy of an ion is given by:

$$U_0 = \frac{1}{2}mv^2 \quad \text{A.8}$$

$$v_0 = \left(\frac{2U_0}{m}\right)^{\frac{1}{2}} \quad \text{A.9}$$

Substituting equation A.9 into equation A.7 gives:

$$t_s = \left[\left(\frac{2U_0}{m} + 2as\right)^{\frac{1}{2}} \pm \left(\frac{2U_0}{m}\right)^{\frac{1}{2}} \right] \frac{1}{a} \quad \text{A.10}$$

The acceleration of an ion can be given in terms of its mass, charge and the electric field causing the acceleration, using Newton's second law:

$$F = ma = qe \rightarrow a = \frac{qE}{m} \quad \text{A.11}$$

Substituting equation A.11 into equation A.10 gives:

Appendix A. Calculations of Ion Flight Times in a Two Field Time-of-Flight Mass Spectrometer

$$t_s = \left(\left(\frac{2U_0}{m} + \frac{2sqE_s}{m} \right)^{\frac{1}{2}} \pm \left(\frac{2U_0}{m} \right)^{\frac{1}{2}} \right) \frac{m}{qE_s} \quad \text{A.12}$$

Equation A.12 can be simplified to:

$$t_s = \frac{(2m)^{\frac{q}{w}}}{qE_s} \left((U_0 + sqE_s)^{\frac{1}{2}} \pm (U_0)^{\frac{1}{2}} \right) \quad \text{A.13}$$

Similar arguments can be used to determine the time, t_d , it takes an ion to travel a distance d :

$$t_d = \frac{v_d - v_s}{a} \quad \text{A.14}$$

where v_d is the velocity after being accelerated through a distance d and a is the acceleration of the ion as it passes through the electric field E_d . v_d is found via:

$$v_d^2 = v_s^2 + 2ad = v_s^2 + \frac{2dqE_d}{m} \quad \text{A.15}$$

Substituting equations A.6 and A.15 into A.14 gives:

$$t_d = \left(\left(v_s^2 + \frac{2dqE_d}{m} \right)^{\frac{1}{2}} - \left(v_0^2 + \frac{2sqE_s}{m} \right)^{\frac{1}{2}} \right) \frac{m}{qE_d} \quad \text{A.16}$$

Substituting again for equations A.6 and A.8 gives:

$$t_d = \left((U_0 + sqE_s + dqE_d)^{\frac{1}{2}} - (U_0 + sqE_s)^{\frac{1}{2}} \right) \frac{(2m)^{\frac{1}{2}}}{qE_d} \quad \text{A.17}$$

Appendix A. Calculations of Ion Flight Times in a Two Field Time-of-Flight Mass Spectrometer

Which then simplifies to:

$$t_d = \frac{(2m)^{\frac{1}{2}}}{qE_d} \left(U^{\frac{1}{2}} - (U_0 + qsE_s)^{\frac{1}{2}} \right) \quad \text{A.18}$$

The ions travel through the drift tube at a constant speed, v_d , as there is no accelerating potential in the drift tube. Hence, the time, t_d , it takes the ions to travel the length of the drift tube, D , is given by:

$$t_D = \frac{D}{v_d} = \frac{D}{\left(v_s^2 + \frac{2dqE_d}{m} \right)^{\frac{1}{2}}} \quad \text{A.19}$$

Substituting equations A.6 and A.8 into equation A.19 gives:

$$t_D = \frac{D}{\left(\left(\frac{2}{m} \right) (U_0 + sqE_s + dqE_d) \right)^{\frac{1}{2}}} \quad \text{A.20}$$

which then simplifies to:

$$t_D = \frac{(2m)^{\frac{1}{2}} D}{2U^{\frac{1}{2}}} \quad \text{A.21}$$

Appendix A. Calculations of Ion Flight Times in a Two Field Time-of-Flight Mass Spectrometer

The total time of flight of an ion through the spectrometer (in seconds) is therefore given by:

$$t = (2m)^{\frac{1}{2}} \left\{ \frac{\left((U_0 + sqE_s)^{\frac{1}{2}} \pm (U_0)^{\frac{1}{2}} \right)}{qE_s} + \frac{\left(U^{\frac{q}{w}} - (U_0 + sqE_s)^{\frac{1}{2}} \right)}{qE_d} + \frac{D}{2U^{\frac{1}{2}}} \right\} \quad \text{A.22}$$

From equation A.22 it can be seen that the time of flight of an ion is proportional to $m^{1/2}$. Since the electric fields and dimensions of the spectrometer are constant, as is the charge on the ion equation A.22 can be abbreviated to give rise to equation A.1.

$$t = k\sqrt{m} + C \quad \text{A.1}$$

The constant k is related to the electric fields and dimensions of the spectrometer and C is due to the delays from the spectrometer's timing electronics. The constants can be found simply by solving two simultaneous equations for two ions of different mass.

Reference

- ¹ W. C. Wiley and I. H. McLaren, Review of Scientific Instruments **26** (12), 1150 (1955).

Appendix B. Error analysis on the Rotational Populations

As discussed in Chapter 3, the rotational populations of the nascent molecules are found by determining the area under the rotational peak, corrected for background, and dividing this area by the laser power normalisation factor, n . To find the errors on the measured rotational populations it is necessary to propagate the error on the background counts under the recorded ion peak, the error on the peak area and the error on the laser power dependence. Figure B.1 shows a REMPI peak illustrating the various parameters described below.

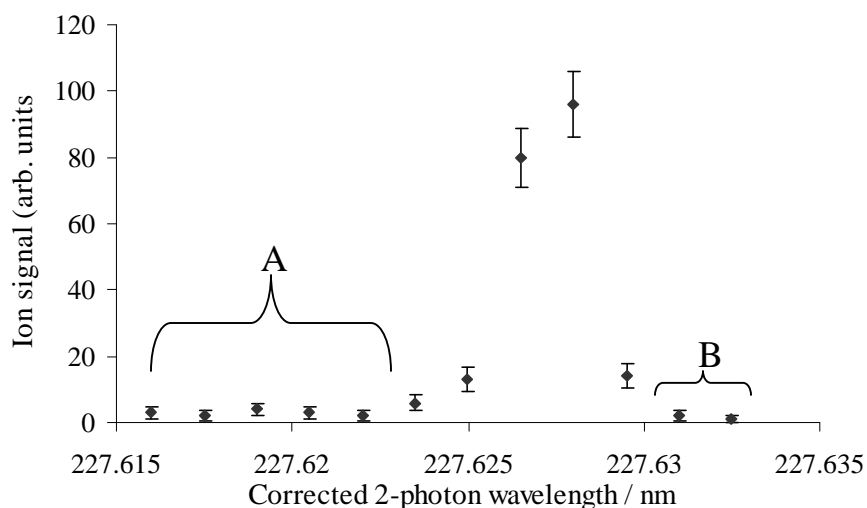


Figure B.2 REMPI plot showing the A and B parameters described in the text.

The average background counts before the peak, A , or after the peak, B , is the mean number of counts before or after the peak. The error associated with each of the background counts, x_i , is Δx_i . Therefore, the error on the average background before the peak, ΔA , is:

$$(\Delta A)^2 = \frac{1}{N} [(\Delta x_1)^2 + (\Delta x_2)^2 + \dots + (\Delta x_N)^2] \quad \text{B.1}$$

Appendix B. Error analysis on the Rotational Populations

where N is the number of laser steps before the peak. Rearranging for ΔA gives:

$$\Delta A = \left\{ \frac{1}{N} [(\Delta x_1)^2 + (\Delta x_2)^2 + \dots + (\Delta x_N)^2] \right\}^{\frac{1}{2}} \quad \text{B.2}$$

Since $\Delta x_i = \sqrt{x_i}$ it follows that:

$$\Delta A = \sqrt{\frac{1}{N} \sum_{i=1}^N x_i} \quad \text{B.3}$$

which is equal to $\sqrt{(\text{mean background counts})}$. The error on the average background counts after the peak, ΔB , is found in the same way.

The error on the measured peak area, E , requires propagation of the error on the average background counts under the peak, C , and the total average counts under the peak, D .

$$C = \left[\frac{A + B}{2} \right] N \quad \text{B.4}$$

where N is now the number of laser steps under the peak. ΔC is found from the errors on A and B using equation B.3 to give:

$$(\Delta C)^2 = \left[(\Delta A)^2 + (\Delta B)^2 \right] \frac{N}{2} \quad \text{B.5}$$

therefore

$$\Delta C = \left\{ \left[(\Delta A)^2 + (\Delta B)^2 \right] \frac{N}{2} \right\}^{\frac{1}{2}} \quad \text{B.6}$$

Appendix B. Error analysis on the Rotational Populations

The error in the total counts under the peak is ΔD :

$$(\Delta D)^2 = (\Delta x_1)^2 + (\Delta x_2)^2 + \dots + (\Delta x_N)^2 \quad \text{B.7}$$

and as before, $\Delta x_i = \sqrt{x_i}$, so:

$$\Delta D = \sqrt{\sum_{i=1}^N x_i} \quad \text{B.8}$$

The measure area under the peak $E = D - C$, hence combining ΔC and ΔD gives ΔE :

$$\Delta E = \left[(\Delta C)^2 + (\Delta D)^2 \right]^{\frac{1}{2}} \quad \text{B.9}$$

The error on the peak then needs to be propagated through the error associated with normalising the laser power. The final rotational population, F , is found by dividing the peak area, E , by the laser power, G , raised to the power of its energy dependence:

$$F = \frac{E}{G^n} \quad \text{B.10}$$

If we let $G^n = H$ then:

$$\left(\frac{\Delta F}{F} \right)^2 = \left(\frac{\Delta E}{E} \right)^2 + \left(\frac{\Delta H}{H} \right)^2 \quad \text{B.11}$$

Given that we know ΔE from equation B.9, we only need to find ΔH .

$$H = G^n \text{ so } \ln H = n \ln G$$

Appendix B. Error analysis on the Rotational Populations

Making the following substitutions:

$$\ln H = J \quad \text{and} \quad \ln G = K \quad \text{then} \quad J = nK \quad \text{which gives:}$$

$$\left(\frac{\Delta J}{J}\right)^2 = \left(\frac{\Delta n}{n}\right)^2 + \left(\frac{\Delta K}{K}\right)^2 \quad \text{B.12}$$

As $K = \ln G$ and $\Delta K = \frac{\Delta G}{G}$, substituting back into equation B.12 gives:

$$\left(\frac{\Delta J}{J}\right)^2 = \left(\frac{\Delta n}{n}\right)^2 + \left(\frac{\Delta G}{G \ln G}\right)^2 \quad \text{B.13}$$

which gives:

$$\Delta J = J \left[\left(\frac{\Delta n}{n}\right)^2 + \left(\frac{\Delta G}{G \ln G}\right)^2 \right]^{\frac{1}{2}} \quad \text{B.14}$$

However, $J = \ln H$ so $H = \exp J$ giving $\Delta J = \frac{\Delta H}{H}$ therefore:

$$\frac{\Delta H}{H} = \ln H \left[\left(\frac{\Delta n}{n}\right)^2 + \left(\frac{\Delta G}{G \ln G}\right)^2 \right]^{\frac{1}{2}} \quad \text{B.15}$$

Substituting equation B.15 back into equation B.11 gives:

$$\left(\frac{\Delta F}{F}\right)^2 = \left(\frac{\Delta E}{E}\right)^2 + \left(n \ln G \left[\left(\frac{\Delta n}{n}\right)^2 + \left(\frac{\Delta G}{G \ln G}\right)^2 \right]^{\frac{1}{2}} \right)^2 \quad \text{B.16}$$

Appendix B. Error analysis on the Rotational Populations

Rearranging equation B.16 for ΔF gives the final error for the rotational population:

$$\Delta F = F \left\{ \left(\frac{\Delta E}{E} \right)^2 + \left(n \ln G \left[\left(\frac{\Delta n}{n} \right)^2 + \left(\frac{\Delta G}{G \ln G} \right)^2 \right]^{\frac{1}{2}} \right)^2 \right\}^{\frac{1}{2}} \quad \text{B.17}$$

which simplifies to:

$$\Delta F = F \left\{ \left(\frac{\Delta E}{E} \right)^2 + (n \ln G)^2 \left[\left(\frac{\Delta n}{n} \right)^2 + \left(\frac{\Delta G}{G \ln G} \right)^2 \right] \right\}^{\frac{1}{2}} \quad \text{B.18}$$

where F is the rotational population divided by the (laser power) ^{n} , E and ΔE are the peak area and associated error, n and Δn are the power to which the laser energy is raised for normalisation and its error and finally G and ΔG are the laser power and its error.

Appendix C. Derivation of Relative PICS and Relative Precursor Specific PICS equations

The equations used to calculate the relative PICS and relative precursor-specific PICS are firstly derived from the Beer-Lambert Law:

$$I = I_0 e^{-nl\sigma} \quad \text{C.1}$$

where I is the intensity of the outgoing electron beam, I_0 is the intensity of the incident electron beam, n is the number density of the sample, l is the length of the sample through which the beam passes and σ is the ionisation cross-section of the sample. If we let $N[X^+]$ represent the number of ionisation events forming X^+ then we get:

$$N[X^+] = I_0 - I \quad \text{C.2}$$

By letting $\sigma[X^+]$ represent the partial ionisation cross-section (PICS) for the formation of ion X^+ and rearranging using equation C.3 for when x is small we get equation C.4:

$$e^{-x} = 1 - x \quad \text{C.3}$$

$$e^{-nl\sigma[X^+]} = 1 - nl\sigma[X^+] \quad \text{C.4}$$

when $nl\sigma[X^+]$ is small. Substituting and rearranging equations C.1, C.2 and C.4 as follows to give equation C.6, the expression for the PICS for ion X^+ .

$$I = I_0 (1 - nl\sigma[X^+]) \quad \text{C.5a}$$

$$I = I_0 (1 - nl\sigma[X^+]) \quad \text{C.5b}$$

Appendix C. Derivation of Relative PICS and Relative Precursor Specific PICS equations

$$I = I_0(1 - nl\sigma[X^+]) \quad \text{C.5c}$$

$$I = I_0(1 - nl\sigma[X^+]) \quad \text{C.5d}$$

$$\sigma[X^+] = \frac{N[X^+]}{I_0nl} \quad \text{C.6}$$

From equation C.6 it is possible to derive the relative PICS for the formation of fragment monocations, $\sigma_r[X^+]$, dications, $\sigma_r[X^{2+}]$ and trications, $\sigma_r[X^{3+}]$, where the cross-section for the formation of the fragment ion X^{m+} is expressed relative to the cross-section for the formation of the parent monocation. The precursor specific relative PICS, $\sigma_r[X^{m+}]$, describe the cross-section for the formation of the ion X^{m+} via single ($n = 1$), double ($n = 2$) and triple ($n = 3$) ionisation relative to the cross-section for the formation of the parent monocation. To derive these equations we first need to derive some terms:

$N_1[\text{parent}^+]$ Number of parent ions formed by ionisation events involving the loss of 1 electron (single ionisation).

$N_1[X^+]$ Number of X^+ ions formed by ionisation events involving the loss of 1 electron (single ionisation), which generate one ion fragment.

$N_2[X^+]$ Number of X^+ ions formed by ionisation events involving the loss of 2 electrons (double ionisation), which generate a pair of fragment ions.

$N_2[X^{2+}]$ Number of X^{2+} ions formed by ionisation events involving the loss of 2 electrons (double ionisation), which generate one ion fragment.

$N_3^{\text{triples}}[X^+]$ Number of X^+ ions formed by ionisation events involving the loss of 3 electrons (triple ionisation), which generate three ion fragments.

Appendix C. Derivation of Relative PICS and Relative Precursor Specific PICS equations

$N_3^{\text{pairs}}[X^+]$ Number of X^+ ions formed by ionisation events involving the loss of 3 electrons (triple ionisation), which generate a pair of ion fragments.

$N_3[X^{2+}]$ Number of X^{2+} ions formed by ionisation events involving the loss of 3 electrons (triple ionisation), which generate a pair of fragment ions.

$N_3[X^{3+}]$ Number of X^{3+} ions formed by ionisation events involving the loss of 3 electrons (triple ionisation), which generate one ion fragment.

f_i Experimental ion detection efficiency.

The experimental ion detection efficiency term arises due to ion losses because of the 90% transmission of the grids that define the electric fields in the apparatus and the less than unity efficiency of the electronics and detector. As well as the above definitions, the measurable parameters that are extracted from the singles, pairs and triples spectra need to be defined:

$I[\text{parent}^+]$ Number of parent^+ ions count in the single spectrum.

$I_1[X^+]$ Number of X^+ ions counted in the singles spectrum.

$I_2[X^{2+}]$ Number of X^{2+} ions counted in the singles spectrum.

$I_3[X^{3+}]$ Number of X^{3+} ions counted in the singles spectrum.

$P_2[X^+]$ Number of X^+ ions counted in the pairs spectrum.

$P_3[X^+]$ Number of X^+ ions counted in the pairs spectrum from triple ionisation (i.e. in coincidence with a doubly charged fragment).

$P_3[X^{2+}]$ Number of X^{2+} ions counted in the pairs spectrum from triple ionisation.

Appendix C. Derivation of Relative PICS and Relative Precursor Specific PICS equations

$T_3[X^+]$ Number of X^+ ions counted in triples spectrum.

With these definitions in place it is now possible to express these measurable parameters in terms of f_i and the number of X^{m+} ions formed *via* ionising events involving the loss of n electrons ($N_n[X^{m+}]$):

$$I[\text{parent}^+] = f_i N_i[\text{parent}^+] \quad \text{C.7a}$$

$$I[X^+] = f_i N_i[X^+] + f_i(1-f_i)N_2[X^+] + f_i(1-f_i)N_3^{\text{pairs}}[X^+] + f_i(1-f_i)N_3^{\text{triples}}[X^+] \quad \text{C.7b}$$

$$I_2[X^{2+}] = f_i N_2[X^{2+}] + f_i(1-f_i)N_3[X^{2+}] \quad \text{C.7c}$$

$$I_3[X^{3+}] = f_i N_3[X^{3+}] \quad \text{C.7d}$$

$$P_2[X^+] = f_i^2 N_2[X^+] + 2f_i^2(1-f_i)N_3^{\text{triples}}[X^+] \quad \text{C.7e}$$

$$P_3[X^+] = f_i^2 N_3^{\text{pairs}}[X^+] \quad \text{C.7f}$$

$$P_3[X^{2+}] = f_i^2 N_3[X^{2+}] \quad \text{C.7g}$$

$$T[X^+] = f_i^3 N_3^{\text{triples}}[X^+] \quad \text{C.7h}$$

It is now possible to rearrange and substitute these equations to give rise to the defined parameters given earlier ($N_m[X^{m+}]$):

$$N_1[\text{parent}^+] = \frac{I[\text{parent}^+]}{f_i} \quad \text{C.8a}$$

Appendix C. Derivation of Relative PICS and Relative Precursor Specific PICS equations

$$N_1[X^+] = \frac{I[X^+]_-(1-f_i)/f_i P_2[X^+]_+ (1-f_i)^2/f_i^2 T[X^+]_-(1-f_i)/f_i P_3[X^+]}{f_i} \quad \text{C.8b}$$

$$N_2[X^+] = \frac{P_2[X^+]_-(1-f_i)/f_i T[X^+]}{f_i^2} \quad \text{C.8c}$$

$$N_2[X^{2+}] = \frac{I_2[X^{2+}]_-(1-f_i)/f_i P_3[X^{2+}]}{f_i} \quad \text{C.8d}$$

$$N_3^{\text{triples}}[X^+] = \frac{T[X^+]}{f_i^3} \quad \text{C.8e}$$

$$N_3^{\text{pairs}}[X^+] = \frac{P_3[X^+]}{f_i^2} \quad \text{C.8f}$$

$$N_3[X^{2+}] = \frac{P_3[X^{2+}]}{f_i^2} \quad \text{C.8g}$$

$$N_3[X^{3+}] = \frac{I_3[X^{3+}]}{f_i} \quad \text{C.8h}$$

As previously mentioned the relative PICS are the cross sections for the formation of the fragment ion X^{m+} relative to the cross section for the formation of the parent monocation, equations C.9a – c.

$$\sigma_r[X^+] = \frac{\sigma[X^+]}{\sigma[\text{parent}^+]} = \sigma_1[X^+] + \sigma_2[X^+] + \sigma_3[X^+] \quad \text{C.9a}$$

$$\sigma_r[X^{2+}] = \frac{\sigma[X^{2+}]}{\sigma[\text{parent}^+]} = \sigma_2[X^+] + \sigma_3[X^+] \quad \text{C.9b}$$

Appendix C. Derivation of Relative PICS and Relative Precursor Specific PICS equations

$$\sigma_r[X^{3+}] = \frac{\sigma[X^{3+}]}{\sigma[\text{parent}^+]} = \sigma_3[X^+] \quad \text{C.9c}$$

Under normal experimental conditions where low electron flux and low ionisation rate are used $N_n[X^{m+}]$ is proportional to $\sigma_n[X^{m+}]$:

$$\sigma_n[X^{m+}] = kN_n[X^{m+}] \quad \text{C.10}$$

where k is constant for each experiment and is dependant on experimental variables such as target gas pressure, electron flux, ionisation volume and the duration of the experiment. Therefore rearranging and substituting equations C.8 – C.10 gives the relative PICS expressed in terms of the measured spectral intensities:

$$\sigma_r[X^+] = \frac{N_1[X^+] + N_2[X^+] + N_3^{\text{pairs}}[X^+] + N_3^{\text{triples}}[X^+]}{N_1[\text{parent}^+]} \quad \text{C.11a}$$

$$= \frac{I[X^+] + P_2[X^+] + P_3[X^+] + T[X^+]}{I[\text{parent}^+]}$$

$$\sigma_r[X^{2+}] = \frac{N_2[X^{2+}] + N_3^{\text{pairs}}[X^{2+}]}{N_1[\text{parent}^+]} = \frac{I_2[X^{2+}] + P_3[X^{2+}]}{I[\text{parent}^+]} \quad \text{C.11b}$$

$$\sigma_r[X^{3+}] = \frac{N_3[X^{3+}]}{N_1[\text{parent}^+]} = \frac{I_3[X^{3+}]}{I[\text{parent}^+]} \quad \text{C.11c}$$

The equations for the relative PICS derived above do not depend on the value of f_i , however, by determining this value the precursor specific relative PICS can be derived by rearranging and substituting equations C.8 – C.10. As mentioned above these cross-sections quantify the ion yield of a particular fragment ion from single, double and triple ionisation, relative to that of the parent monocation.

Appendix C. Derivation of Relative PICS and Relative Precursor Specific PICS equations

$$\sigma_1[X^+] = \frac{N_1[X^+]}{N_1[\text{parent}^+]} \quad \text{C.12a}$$

$$= \frac{I[X^+] - ((1-f_i)/f_i)(P_2[X^+] + P_3[X^+]) + ((1-f_i)^2/f_i^2)T[X^+]}{I[\text{parent}^+]}$$

$$\sigma_2[X^+] = \frac{N_2[X^+]}{N_1[\text{parent}^+]} = \frac{P_2[X^+] - 2((1-f_i)/f_i)T[X^+]}{f_i I[\text{parent}^+]} \quad \text{C.12b}$$

$$\sigma_3[X^+] = \frac{N_3^{\text{pairs}}[X^+] + N_3^{\text{triples}}[X^+]}{N_1[\text{parent}^+]} = \frac{(P_3[X^+]/f_i) + (T[X^+]/f_i)}{I[\text{parent}^+]} \quad \text{C.12c}$$

$$\sigma_2[X^{2+}] = \frac{N_2[X^{2+}]}{N_1[\text{parent}^+]} = \frac{I_2[X^{2+}] - ((1-f_i)/f_i)P_3[X^{2+}]}{I_1[\text{parent}^+]} \quad \text{C.12d}$$

$$\sigma_3[X^{2+}] = \frac{N_3[X^{2+}]}{N_1[\text{parent}^+]} = \frac{P_3[X^{2+}]}{f_i I_1[\text{parent}^+]} \quad \text{C.12e}$$

$$\sigma_3[X^{3+}] = \frac{N_3[X^{3+}]}{N_1[\text{parent}^+]} = \frac{I_3[X^{3+}]}{I_1[\text{parent}^+]} = \sigma_r[X^{3+}] \quad \text{C.12f}$$